UNIVERSIDAD DE CHILE
FACULTAD DE CIENCIAS FÍSICAS Y MATEMÁTICAS
DEPARTAMENTO DE INGENIERÍA ELÉCTRICA

CONTROL OF THE MODULAR MULTILEVEL MATRIX CONVERTER BASED ON CONTINUOUS CONTROL SET MODEL PREDICTIVE CONTROL

TESIS PARA OPTAR AL GRADO DE
DOCTOR EN INGENIERÍA ELÉCTRICA
EN COTUTELA CON LA UNIVERSIDAD DE NOTTINGHAM

MATÍAS ALONSO URRUTIA ORTIZ

PROFESORES GUÍAS:
ROBERTO CÁRDENAS DOBSON
ALAN WATSON

PROFESOR CO-GUÍA
JONATHAN CLARE

MIEMBROS DE LA COMISIÓN:
PATRICIO MENDOZA ARAYA
MARCELO PEREZ LEIVA
LUCA TARISCIOTTI

SANTIAGO DE CHILE
2022

RESUMEN DE TESIS PARA OPTAR
AL GRADO DE DOCTOR EN INGENIERÍA ELÉCTRICA
POR: **MATÍAS ALONSO URRUTIA ORTIZ**
FECHA: 2022
PROF. GUÍAS: ROBERTO CÁRDENAS y ALAN WATSON
PROF. CO-GUÍA: JONATHAN CLARE

CONTROL DEL CONVERTIDOR MODULAR MATRICIAL MULTINIVEL POR MEDIO DE UN ESQUEMA DE CONTROL PREDICTIVO CON CONJUNTO DE CONTROL CONTINUO

El convertidor matricial modular multinivel (M3C) es un convertidor de potencia AC/AC conformado por 9 ramas, el cual ha sido propuesto para soluciones de alta potencia como accionamientos o sistemas de conversión eólicos. Debido a su inherente complejidad, el control del M3C típicamente se subdivide en varias metas, además de dos modos de operación: Modo de Frecuencias Distintas (DFM), y Modo de Frecuencias Iguales (EFM). En operación EFM, el control es más complejo y requiere consideraciones adicionales. Este trabajo presenta un esquema de regulación de energía y corrientes circulantes para el M3C utilizando Control Predictivo con Variables Continuas (CCS-MPC) en dos etapas. La primera etapa MPC usa un problema de programación cuadrático con restricciones de igualdad, el cual su solución es obtenida de manera analítica. Esta formulación sirve tanto para DFM como para EFM. La segunda etapa MPC controla las corrientes circulantes, donde se definió un problema de programación cuadrática con restricciones de desigualdad. Para resolver este problema, se implementó un algoritmo de conjunto activo (active-set). La validación de este trabajo se completó por medio de resultados de simulación y experimental en un prototipo M3C de 27 celdas. Según los resultados obtenidos, el esquema propuesto permite un buen desempeño del M3C.

ABSTRACT OF THE THESIS FOR THE GRADE
DOCTOR EN INGENIERÍA ELÉCTRICA
AUTHOR: **MATÍAS ALONSO URRUTIA ORTIZ**
DATE: 2022
SUPERVISORS: ROBERTO CÁRDENAS AND ALAN WATSON
CO-SUPERVISOR: JONATHAN CLARE

CONTROL OF THE MODULAR MULTILEVEL MATRIX CONVERTER BASED ON CONTINUOUS CONTROL SET MODEL PREDICTIVE CONTROL

The Modular Multilevel Matrix Converter (M3C) is an AC to AC power converter composed of 9 arms that has been proposed for high power applications such as motor drive and wind energy conversion systems. Due to its complex nature, control of the M3C is usually divided into several sub-goals, and the capacitor voltage regulation varies according to the operating mode, where two classifications are commonly used: Different Frequency Mode (DFM), and Equal Frequency Mode (EFM). EFM is more challenging, because of the larger capacitor voltage oscillations that can be produced. In this work, a Continuous-Control-Set Model Predictive Control (CCS-MPC) for energy management and circulating current control of the M3C is proposed. A first MPC stage solves an equality constrained quadratic programming problem, for which an optimal solution is analytically obtained. The result is a simple control law, which ensures good transient and steady performance in EFM/DFM. The second MPC stage, regulates the circulating currents with an inequality constrained quadratic programming problem. To solve the inherent optimisation problem associated with the second CCS-MPC, an active-set algorithm is implemented. Experimental and simulation results from a 27-cell M3C prototype validate the proposed strategy and show a good overall performance.

This work is sincerely dedicated to my beloved wife, mother, father, and siblings.

Acknowledgements

This work was supported by CONICYT- PCHA/Doctorado Nacional/2018-21181386 and in part by Fondecyt under Grant 1221392 and in part by the Basal Project under Grant FB0008.

Table of Content

List of Tables

List of Figures

Nomenclature

AC	Alternating Current
CMV	Common-mode voltage
CSC	Current Source Converter
CCS-MPC	Continuous Control Set Model Predictive Control
CCV	Cluster Capacitor Voltage
DFM	Different Frequencies Mode
EFM	Equal Frequencies Mode
EC-QP	Equality constrained Quadratic Programming
FCS-MPC	Finite Control Set Model Predictive Control
HVDC	High-Voltage Direct Current
i_{bi}	i-th Arm current
$\boldsymbol{I}_x$	Identity matrix of order x.
IEA	International Energy Agency
$\mathrm{i}_{\varepsilon \mathrm{i}}$	i-th Circulating current
M2C	Modular Multilevel Converter
M3C	Modular Multilevel Matrix Converter
MDS	Motor-Drive Systems
MIMO	Multiple Input Multiple Output
MMCs	Modular Multilevel Converters
MVSC	Multilevel Voltage Source Converter
OSS	Optimal Switching State
OSV	Optimal Switching Voltage
PLL	Phase-Locked Loop
PD-PWM	Phase Disposition Pulse-width Modulation
PWM	Pulse-width Modulation
QP	Quadratic Programming
$\boldsymbol{Q}_{\mathrm{e}}$	Cost weight matrix related to the T-SSCV
$\boldsymbol{R}_{\mathrm{e}}$	Cost weight matrix related to the circulating currents
SISO	Single Input Single Output
SSCV	Sum of the Squares of the Cluster Capacitor Voltages

T-CCV	Transformed Cluster Capacitor Voltage
T-SSCV	Transformed SSCV
TBT	Transient Balancing Test
VSC	Voltage Source Converter
v_{bi}	i-th Output Cluster Voltage
WECS	Wind Energy Conversion System
ψ_{bi}	SSCV of the i-th cluster

Chapter 1

Introduction

Since the mid 1980s when Motor-Drive Systems (MDS) appeared, they have been used for extensive applications in a wide variety of industries, like the oil and gas sectors, production plants, and process industries [1, 2]. Although most of the Medium Voltage-MDS available in the market are reliable and their technology is well stablished, there remains a great potential for improving their efficiency [1]. Acccording to the International Energy Agency (IEA), MDS are the largest source of electricity demand with over 40 % of the worldwide energy consumption. Most of these are MV solutions, for which about 60 % could improve their efficiency with modern control schemes [3].

In Addition to traditional MV-MDS solutions, such as current source converter (CSC) [4, 5] and two level Voltage Source Converter (VSC) [1, 6], the Multilevel Voltage Source converters (MVSC) have risen in prominence, with important successful implementations in the industry [7, 8, 9]. The main aspect that motivated the invention of MVSCs was to overcome the limitations of the semiconductors, mainly due to voltage-blocking capability [6].

Within the MVSCs extensive family, Modular Multilevel Converters (MMCs) have acquired special interest due to their completely modular design, their scalability without increasing the component ratings, the possibility of a transformerless configuration, their fault-tolerant operation capability and applicability for wind energy conversion systems (WECS) [10, 11, 12, 13]. At present, the Modular Multilevel Converter (M2C) is the only topology from the MMC family that has been used in the industry with successful results. Specifically, the M2C has been proposed and mostly implemented in High Voltage Direct Current (HVDC) applications with the first project in 2010, called the Trans Bay Cable, which is an HVDC link between the cities of Pittsburg and San Francisco with two M2C, and a capacity of 400MW and ±200kV. More recently, *Sinamics Perfect Harmony* by Siemens has positioned the M2C as a suitable option for electrical drives with ratings up to 24MW at 11kV [14]. This first step has opened the door to more companies to produce solutions based on MMC technology, such as ABB, CEPRI and GE [15, 16, 17]. In addition to the M2C,

the Modular Multilevel Matrix Converter (M3C) is another MMC topology that has been identified for use in AC-AC medium to high-power applications [10, 18, 19]. According to [20], it is expected that the M3C could compete with high-power cyclo-converter-based drives. Specifically, the M3C is composed of nine clusters containing a stack of series-connected full-bridge power-cells. As is inherent to all MMCs, maintaining correct operation of the M3C is challenging as the capacitor voltage of each power-cell is floating and the power-cells charge and discharge depending on the operating conditions. Additionally, large low-frequency oscillations occur naturally in the capacitor voltages at some operating points [21]. The magnitude of these fluctuations can reach unacceptable values unless compensation methods are implemented.

Typically, the M3C operation is categorised into two main modes to consider the floating capacitor voltage oscillations. The first mode, referred to as "Different Frequencies Mode" (DFM), is enabled when the input-port frequency is higher or lower (by a given threshold) than the output-port frequency. The second mode is referred to as "Equal Frequencies Mode" (EFM), and is enabled when the output-port frequency is close or equal to the input-port frequency. Capacitor voltage oscillations are relatively small in DFM; however, low frequency capacitor voltage fluctuations increase in magnitude as the M3C enters EFM operation [22].

To achieve energy balance in the M3C, i.e. to regulate the floating capacitor voltages of the nine clusters, four circulating currents are utilised as degrees of freedom [23, 11, 21]. Usually these currents have two or more frequency components [21, 24], and typically Proportional (P) controllers have been proposed for regulating them [11, 25, 26, 21]. Although P-controllers have shown adequate performance in some applications, they cannot provide good tracking for sinusoidal references unless the gain is increased, which introduces a trade-off between improvement in tracking error and an undesirable amplification of the electrical noise in the measurements. Moreover, as typically happens in most of the practical control systems, a large increase in the control gain may move the closed loop poles to poorly damped positions which certainly affect the dynamic response of the system. To avoid the inherent tracking problem of P- and PI-controllers in the presence of sinusoidal references, in [27] the utilisation of multi-resonant controllers is proposed. However, multi-resonant controllers have to be tuned online when the input and/or output frequencies are varying, which implies that some sort of self-tuning algorithm is required (see [27, 28]).

In addition to the requirement for satisfactory reference-tracking with high-bandwidth for the circulating current control, a saturation scheme should be included to ensure effective protection of the converter. The total current in each arm of the M3C has several components, i.e a contribution from the input and output currents, and a contribution from each of the four circulating currents.

At present, the arm current control schemes reported in the literature saturate each voltage and current component separately, e.g. saturating the input current vector, output current vector, positive and negative sequence components of the circulating currents, using heuristic criteria [21, 24]. This is certainly a sub-optimal solution because limiting each component

independently does not ensure that the arm current or voltage is adequately limited or, conversely, fully exploited.

Conversely, Model Predictive Control (MPC) has been widely proposed and implemented within power electronic and drive systems, where the high-bandwidth response with straightforward incorporation of system non-linearities and operating constraints are its most attractive features [11, 29]. At present, the majority of the proposed MPC strategies for MMCs are aimed at regulating the M2C with Finite-Control Set MPC (FCS-MPC) schemes [30, 31, 32, 33, 34, 11, 29, 35]. A limited number of works have discussed Continuous-Control-Set MPC (CCS-MPC) for control of the MMC [36, 37, 38]

The research presented in this thesis aims to control the M3C with a CCS-MPC scheme. From an implementation perspective, the proposed scheme uses two cascaded MIMO based CCS-MPC, which are discussed in detail for M3C applications. Specifically, the first MPC stage aims to properly regulate the capacitor voltages during DFM and EFM with a straightforward control-law obtained from an analytical solution; afterwards, the following MPC stage regulates the circulating currents, where an arm-saturation scheme for arm voltages and currents is included, which exhibits attractive results during transient operation of the M3C.

To the best of the author's knowledge, this MPC approach has not been reported previously in the literature. Moreover, this scheme can be further used for regulating other MMC topologies with a similar procedure. The proposed control scheme is validated through simulation and experimental work, with successful and promising results.

1.1. Hypotheses

The following topics are the working and stated hypotheses for the proposed research project:

- (H1) A continuous set model predictive control scheme can be implemented for mitigating and balancing the energy of the clusters in an M3C.
- (H2) A circulating current control scheme, based on a continuous model predictive control strategy, can improve the overall arm current and voltage saturation scheme.
- (H3) Compared to conventional schemes, a better dynamic performance and further capabilities can be achieved during critical operating points of the M3C by using the proposed MPC scheme.
- (H4) A saturation scheme for the arm currents and voltages can be used during transient operation without affecting input/output ports.

1.2. Project Goals

The main goals of the proposed research project are to research, design, implement and validate a novel control scheme for a M3C based on Continuous Control Set Model Predictive Control (CCS-MPC). This strategy allows a full frequency operation range that includes critical operation points. The validation consists of simulation and experimental work.

1.2.1. Specific Goals

- To propose a new Continuous Control Set Model Predictive Control strategy for capacitor voltage control of the M3C.
- To propose a Continuous Control Set Model Predictive Control strategy for circulating current control of the M3C with an integrated arm-saturation scheme.
- To simulate the overall MPC strategy.
- To set up an experimental prototype of an M3C, which it is composed of 27 power modules.
- To validate experimentally the proposed control scheme in the M3C.

1.2.2. Methodology

The procedure to prove or refute the proposed hypotheses is divided in three steps:

1. There is an analytical development of the idea.

2. The premise is carefully tested and validated by simulation using the software packages *Plecs* and *Simulink*.

3. After the second step, several experimental tests are prepared and are performed in an experimental prototype.

According to this methodology, the presented document exhibits an essential development of analytical work, which is thoroughly studied through several cases in a simulation environment. Afterwards, the proposed strategy is validated with an experimental prototype.

1.3. Thesis Structure

The structure of this work is the following:

- Chapter 1 includes the Introduction, Project Goals and Hypotheses.
- Chapters 2 to 5 present the literature review of the Modular Multilevel Matrix Converter (M3C), starting with an introduction to the MMC and M3C topologies in Chapter 2, the modelling approach in Chapter 3, the conventional control based on linear controllers in Chapter 4, and, finally, M3C control schemes based on optimisation approaches in Chapter 5.
- Chapter 6 describes the proposed control scheme for the M3C in detail.
- Chapters 7 to 9 show the simulation and experimental work with the result obtained. A detailed description of the experimental prototype used is also given.
- Chapters 10 and 11 include the final conclusions related to the work, where the benefits, limitations, contributions and proposed future work are presented.
- The appendix section show the Model Predictive Control general definitions and analytical development.

Chapter 2

Introduction to the Modular Multilevel Matrix Converter (M3C)

This chapter describes the essentials of the Modular Multilevel Converters and, specifically, of the M3C. Firstly, a brief introduction of the Modular Multilevel Converters (MMCs) family is presented, where the basic structure, features, and research trends are introduced. Afterwards, an introduction, applications and challenges of the M3C are presented.

2.1. The Modular Multilevel Converters Family

The Modular Multilevel Converters (MMCs) family is a subdivision of the bigger Multilevel Converters (MCs) group [2, 39, 40, 41, 20]. Although the MC technology can be considered as mature due to its wide acceptance, the emerging challenges are still vast. Specifically, one of these challenges is the creation of new topologies to solve limitations or to enhance capabilities of the traditional configurations: Neutral-Point Clamped (NPC), Floating-Capacitor (FC) and Cascaded H-Bridge (CHB). From these traditional MC groups, the two latter topologies have the attractive feature of being modular [see Figure 2.1], which implies that their scalability is straightforward, without requiring higher rating of the semiconductors. Although FC and CHB inverters have attractive features, as depicted in Figure 2.1, both configurations have limiting requirements. In the case of the FC, one main DC-link bus is required and sized according to the maximum available DC-voltage and nominal rating. Additionally, extra capacitors with different voltage levels are required when the voltage level of the converter is increased, which implies that the rating of the corresponding semiconductors are different. In addition to the regulation of the phase currents, the FC requires an additional scheme for balancing the floating capacitors. To address this issue, several methodologies have been published [42, 43].

In the case of the CHB, this inverter topology requires several rectification stages, where one rectifier is required per-module. Therefore, specific and complex transformers with several

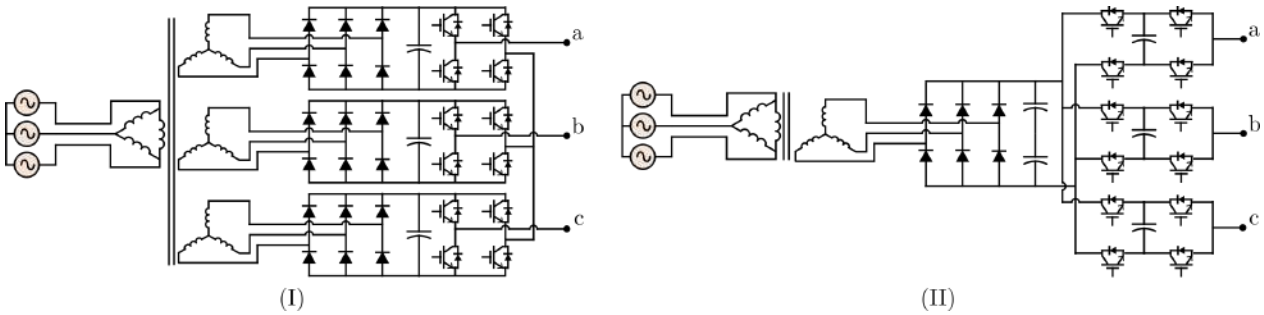

Figure 2.1: (I) 3-level Cascaded H-Bridge inverter (3L-CHB). (b)3-level Flying Capacitor inverter (3L-FC).

phases are used to reduce the harmonic distortion of the input side system. The CHB does not require a balancing control of the capacitor voltages, since they are defined by the corresponding rectification stage. In order to reduce the bulkiness of the transformer , asymmetrical CHB topologies have been reported [44].

2.1.1. Fundamental Structure of the MMCs

As aforementioned, MMCs are a sub-family of the MCs, where their building block is the power cell, which is based on power semiconductors and floating capacitors. Although there are several types of power-cells, the most often used are the Full-bridge and Half-bridge ones [see Figure 2.2.(a)-(b)]. A set of n cells connected in series with an inductor constitutes an arm, as illustrated in Figure 2.2.(c)-(d), whose interconnections define the specific topologies of the MMC family [11]. Another distinctive feature of the MMCs is the availability of linear independent circulating currents within the converter, which do not interfere with input and output port currents. These currents are degrees of freedom and are used to achieve the balancing of the capacitor voltages. In Figure 2.3, a general diagram specifies the input/output port currents and n circulating currents of a MMC.

The members of the MMC family are few. One of the traditional MMC members is the modular multilevel matrix converter (M3C), which is composed of two AC ports interconnected through nine arms as shown in Fig. 2.4(a). Potential solutions based on this kind of converter in high-power electrical drives and wind energy conversion systems have been reported in [13, 45, 25]. Another converter, and currently the most represantive member of the MMC family, is the Modular Multilevel Converter (M2C), which is a DC/AC converter (see Figure 2.4.(b)). The M2C is composed of six arms with half-bridge cells as its building block. Other examples of converters that are members of the MMC family are the Hexverter and the Alternating Arm Converter (AAC), among many others [11]. The Hexverter is an AC/AC converter made up of six arms with H-bridge cells, and its name is related with the number of its arms and ports, see Figure 2.5.(a)[46]. The Alternating Arm Converter (AAC) is a DC/AC converter defined as a hybrid MMC, because it is derived from the M2C structure, but with additional bidirectional semiconductors in each of its six arms, and H-bridge modules instead of half-bridges (see 2.5.(b)). These new features allow a reduction

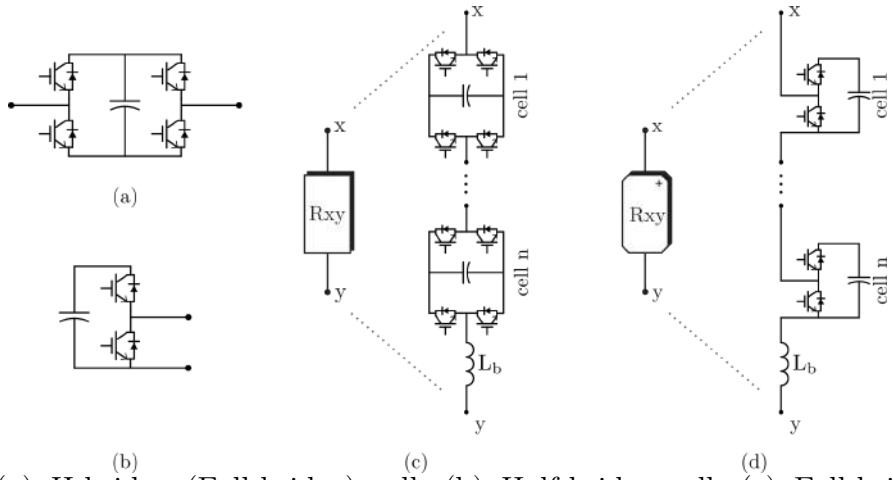

Figure 2.2: (a) H-bridge (Full-bridge) cell. (b) Half-bridge cell. (c) Full-bridge arm. (d) Half-bridge arm.

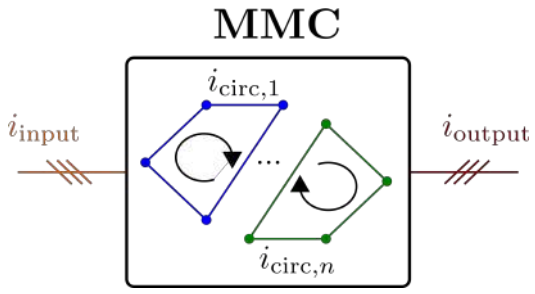

Figure 2.3: Conceptual description of the Input /Output port currents and n circulating currents for a traditional MMC.

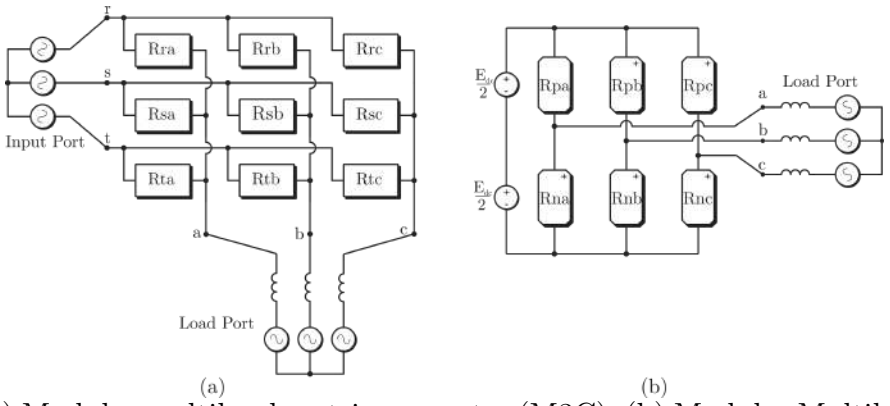

Figure 2.4: (a) Modular multilevel matrix converter (M3C). (b) Modular Multilevel Converter (M2C).

of the required number of sub-modules, less energy storage, and more degrees of freedom to deal with DC failures [47]. Table 2.1 shows the mentioned topologies, their corresponding power cell structure, and the number of available circulating currents.

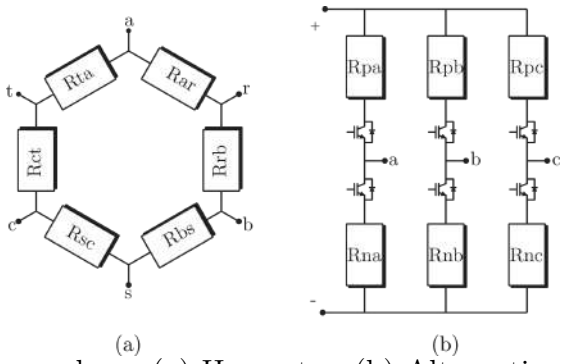

(a) (b)

Figure 2.5: Other MMC members: (a) Hexverter; (b) Alternating Arm Converter (AAC).

Table 2.1: MMCs most common topologies.

Topology	Type	Power-Cell	N° Arms	N° Circulating Currents
M2C	DC/AC	Half-Bridge	6	2
M3C	AC/AC	Full-Bridge	9	4
Hexverter	AC/AC	Full-Bridge	6	1
AAC	DC/AC	Full-Bridge	6	2

2.1.2. Trends and Current Challenges for MMCs

Due to the modular structure enables infinite architecture and control possibilities, the study of MMCs is also extensive and can be roughly classified into two sub-trends: new topology studies and enhanced/new control schemes.

New Architecture Trends

In addition to full-bridge and half-bridge cells, different module architectures have been proposed for MMCs [48]. In [49], a power-cell inspired on an active neutral point clamped leg is proposed for the M2C, achieving losses reduction and enabling an internal fault management capability (see Figure 2.6 (a)). Similarly, a power cell built from cross-connected half-bridges have been proposed in [50], enabling more voltage levels with fewer components in comparison with half-bridge cells. Additionally, a fault-clearance capability power cell is proposed in [51] (Figure 2.6 (c)).

Although the most relevant MMCs are based on a single kind of power cells, its construction can be extended by using hybrid structures. For instance, an hybrid structure for the M2C that consists of full-bridge and half-bridge cells have been proposed [52]. This hybrid architecture allows the same operation of a traditional M2C in HVDC, but with fewer cells. Moreover, in [53], an hybrid structure between an M2C and two 2-level converters is used to achieve a straightforward regulation of reactive power and negative sequence (see Figure 2.7 (a)). In [54], a replacement of a M2C based on a different arrangement of its six arms is proposed for HVDC solution. The proposed structure allows a reduction in the number of half-bridges, but it requires three single-phase transformers (refer to Figure 2.7 (b)).

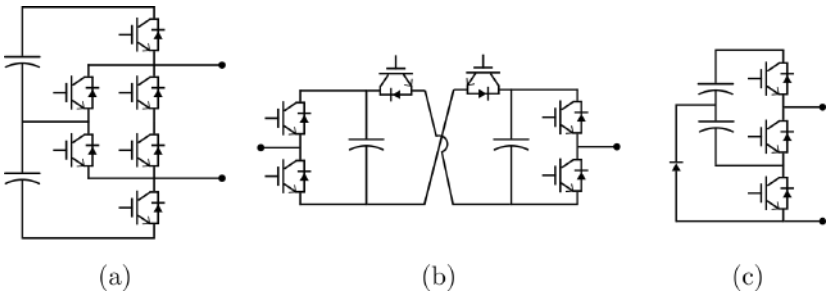

Figure 2.6: (a) Cell inspired on an active neutral point clamped leg; (b) Cross-connected half-bridges cell; (c) Fault-tolerant cell.

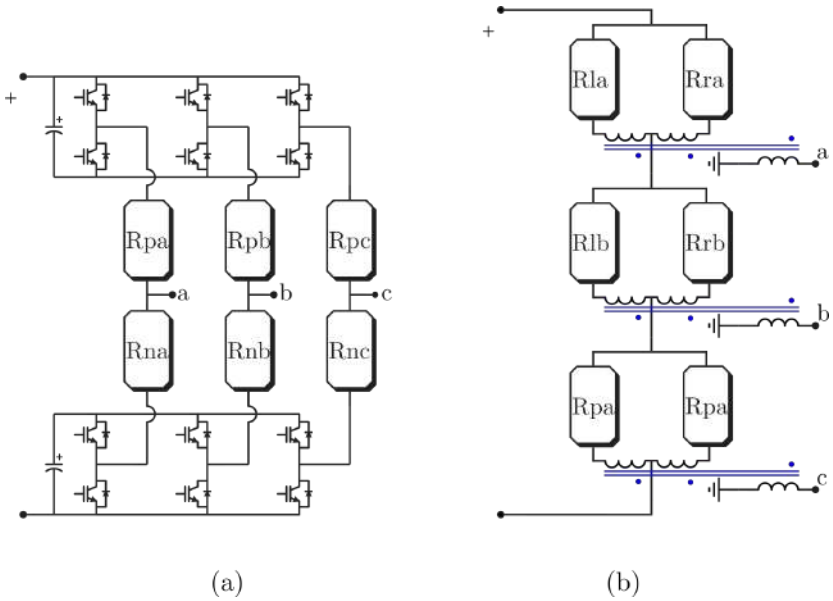

Figure 2.7: (a) M2C hybrid derivation; (b) M2C derivation inspired on a Push-pull concept.

Control Challenges

As same as their inherent architecture, the regulation of MMCs is highly challenging due to its inherent Multiple-Input Multiple-Output (MIMO) non-linear system nature. Nowadays, the traditional and most adopted control approach is the implementation of a three stage scheme: stored energy control, arm current control, and modulation with local balancing control. Moreover, depending on the application of the MMCs, undesirable lower frequency oscillation in the capacitor voltages could emerge, requiring extra considerations and control design targets for its operation. As explained in the incoming chapters, different approaches have been proposed for MMC regulation, where the most used is based on linear controllers. Although the linear-controllers approach can be considered as sufficient, several other approaches are being reported recently to enhance their performance on different applications [55].

2.2. The Modular Multilevel Matrix Converter (M3C)

The M3C, shown in Figure 2.8, is an AC/AC converter composed of nine arms, which can be grouped into three sub-converters for analysis purposes. Usually referred to as the second most studied MMC family member, the M3C is also known as Direct MMC and Triple-Star Bridge Cells (MMCC-TSBC) [56, 24, 57]. Each cell of the n-cell cluster is composed of several H-bridges cells (Figure 2.2 (a)) with DC floating capacitors. Unlike its first proposed architecture [58], in the modern M3C topology, all the nine arms are connected with inductors. This component facilitates the controllability of the M3C by treating each arm as a current source.

The arm inductors can be designed with different configurations per sub-converter [59, 60]: (a) three individual single-core inductors, (b) three coupled single-core inductors, (c) three-legged core three-winding structure and (d) three-legged core six-winding structure. The aim of options (b) to (d) is to decrease the overall weight, volume and cost of the inductors. Option (c) allows a reduction of the overall weight by neglecting the output currents in the design. Conversely, option (d) reduces the total weight near 32 % of the case based on configuration (a).

2.2.1. Proposed Solutions based on M3C

At present, there has not been presented a commercial solution based on the M3C yet. However, the study of potential solutions using this converter is active from the academic perspective. More specifically, the M3C has been mainly proposed for high-power applications such as wind energy conversion systems (WECS) and Low-Frequency fractional AC (LFAC)

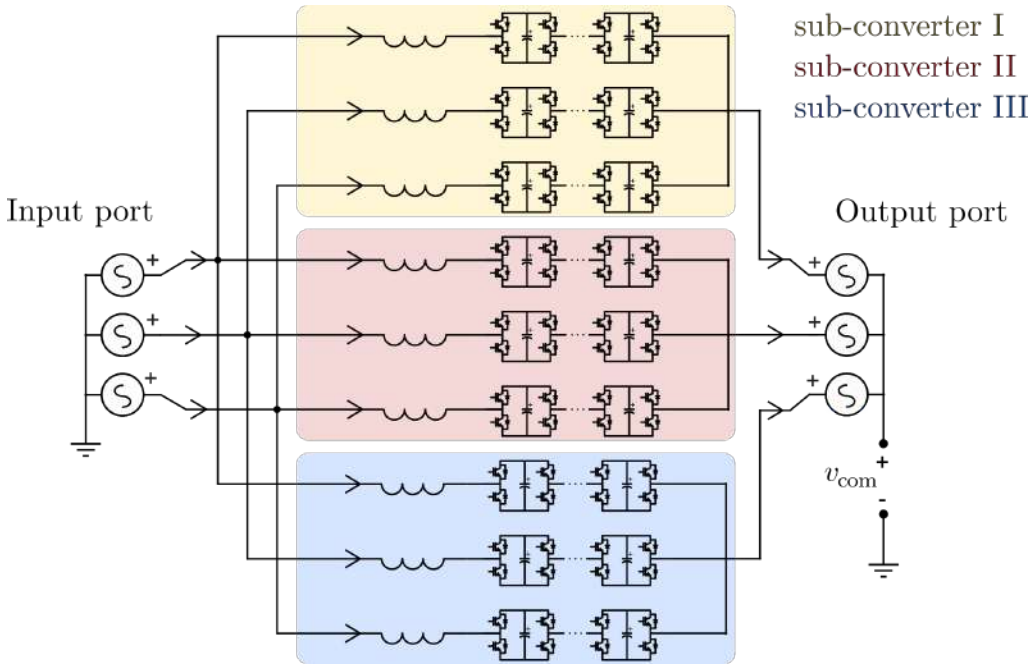

Figure 2.8: M3C architecture, grouped into three sub-converters.

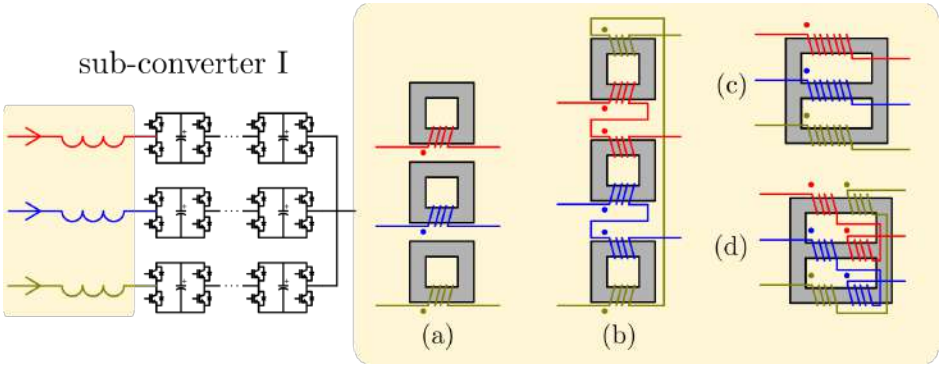

Figure 2.9: Inductor options for M3C sub-converter. (a) three individual single-core inductor per arm, (b) three coupled single-core inductors, (c) three-leg core three-winding structure and (d) three-leg core six-winding structure with intrazigzag connection.

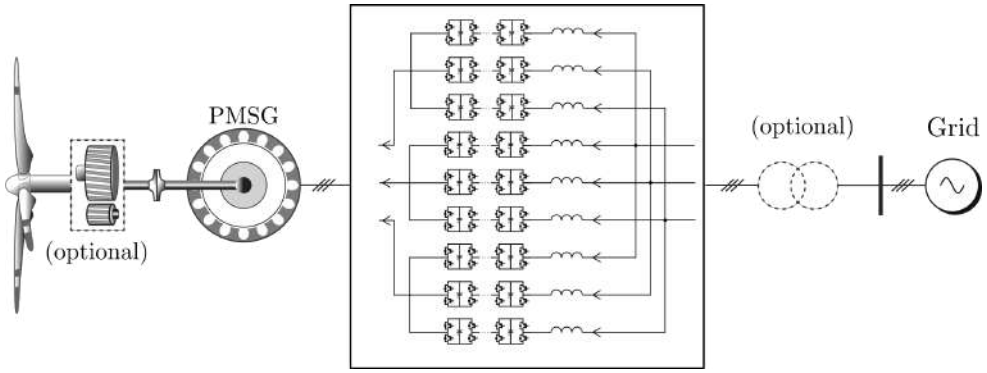

Figure 2.10: WECS type-4 turbine based on a PMSG and M3C.

transmission systems.

WECS based on the M3C

At the beginning, Erickson et al. proposed the M3C for wind energy applications [58, 61]. This idea has been extended in more recent papers for type-4 turbines, as shown in Figure 2.10 [13, 18, 21, 62]. Based on the presented results, the fault-clearance capability based on its redundancy and the exhibited good performance when the machine operates at low speed with nominal torque prove that the M3C is an attractive option for WECS. In contrast to the M2C, at low-frequency operation, the M3C capacitor voltages are relatively simple to control, even without requiring a mitigation scheme in general [13].

Low-Frequency AC Transmission Systems (LFAC)

The LFAC systems, also referred to as fractional frequency transmission systems, has been proposed to compete with HVDC systems. Traditionally, transmission systems between 1-20Hz are considered as LFAC systems [63]. One of the main benefits of LFAC systems are the possibility to enhance the power capability of the transmission cables in comparison to standard 50 Hz or 60 Hz AC transmission systems [64]. Moreover, in comparison with HVDC transmission, a LFAC system is less expensive and the protection devices are similar to the

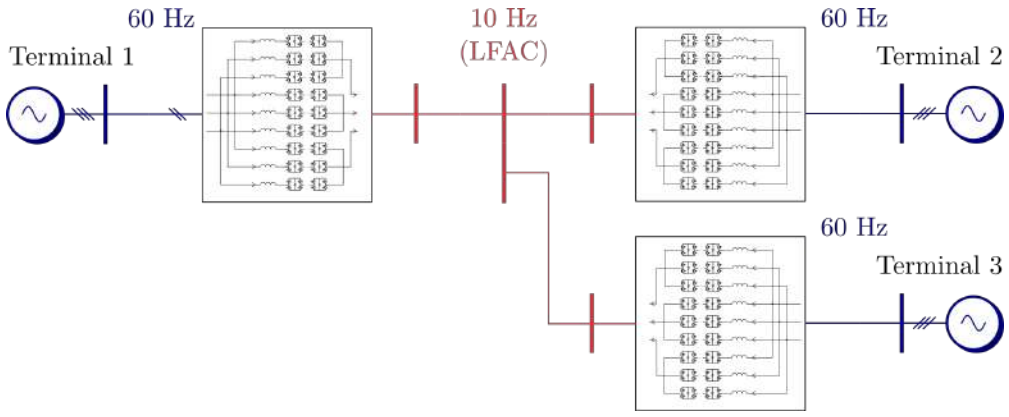

Figure 2.11: Multiterminal 60Hz-to-10Hz LFAC system based on three M3C.

50-60Hz AC systems. In this context, the M3C has been proposed for off-shore WECS and asynchronous power system interconnections [65, 66, 67, 68, 69, 70]. In [65], a 9-cell M3C was proposed for LFAC using space-vector modulation (SVM). Unfortunately, the presented control scheme is not valid for M3C with higher number of cells due to the high computational burden of the algorithm. More recently, in [70], a multi-terminal LFAC system based on three M3Cs is proposed. As depicted in Figure 2.11, three M3C are proposed for a 60Hz to 10Hz conversion. A virtual synchronous generator (VSG) scheme is proposed for energy management among terminals. The frequency difference between the input and output ports above 10-20Hz implies that a mitigation scheme for the capacitor voltage regulation is not necessary from the M3C control perspective. Therefore, this benefit points to considering the M3C as a good candidate for LFAC systems.

Challenges and Trends

Several advantages are gained due to the M3C high control flexibility and redundant architecture. For instance, its most prominent benefits are the ability to include better power quality without requiring extra passive components, transformer-less operation, and continuous operation during faults.

In addition to WECS and LFAC system solutions, the M3C has also been proposed for variable-speed drives and FACTS [71, 72]. In these specific applications, the output port frequency operation is near or the same as the grid frequency, which implies that further control and design requirements must be considered. Particularly for the M3C, solutions that include this frequency range is challenging and an open issue. The control techniques with the corresponding design, which depend on the solution requirements, are actively discussed and reported in the available literature.

Additionally, operation during cell and even arm faults have been generously reported [73, 74, 75, 76, 77]. The redundancy and the natural complexity of the M3C allow several possibilities to include a fault-tolerant capability.

Consequently, it is expected that further research will play a major role in making the

M3C an industrial-feasible power converter. Hopefully, the current academic tendency on the M3C will still continue to encourage power electronics engineers and scientists to carry out further research on this converter.

2.3. Summary of the Chapter

Modular multilevel converters (MMCs) are built by the interconnection of several power cells, which allow redundancy and flexibility in their operation. Although the M2C and M3C are their most attractive topologies, other novel MMC structures have been proposed and studied. Nowadays, the study of MMCs is active, and proposals of new architectures or novel control schemes are consistently increasing.

The M3C is an AC/AC converter conformed of H-bridge power cells arranged in nine arms. Although it has not been implemented as an industrial solution, its study is very active. Particularly, the M3C has been considered for WECS solutions and LFAC systems, but its application has been extended for variable-speed drives and as FACT devices. Additionally, the particular M3C architecture allows fault-tolerant capability even including arm faults. Therefore, the study of the M3C is wide and open with several possibilities.

In the following chapter, the modelling of the M3C is introduced. Afterwards, in the next chapter, an overview of the control schemes available in the literature is presented and discussed.

Chapter 3

Modelling of the M3C

In this chapter, the modelling of the M3C is introduced and discussed. The circulating currents of the converter are analytically obtained and presented as a degrees of freedom from the control perspective. Moreover, a steady state operation analysis is provided, which allows the understanding of the critical operating ranges of the converter.

In contrast to the previously reported matrix-type modelling [22, 21], the proposed model is a state-space representation of the converter, which is based on the work reported in [78]. In comparison with the matrix-type model, this work adopts a vector form, maintaining the same current and capacitor voltage dynamic definitions. This model approach allows a straightforward interpretation of the subsequent introduction of the linear transform at the arm current and the stored energy dynamics. Additionally, the state-space model approach enables the implementation of MIMO-based control techniques, for instance, Model Predictive Control, Kalman filters and sensor-less approaches.

The model is based on two decoupled dynamic sub-models: (a) Current/Voltage Model

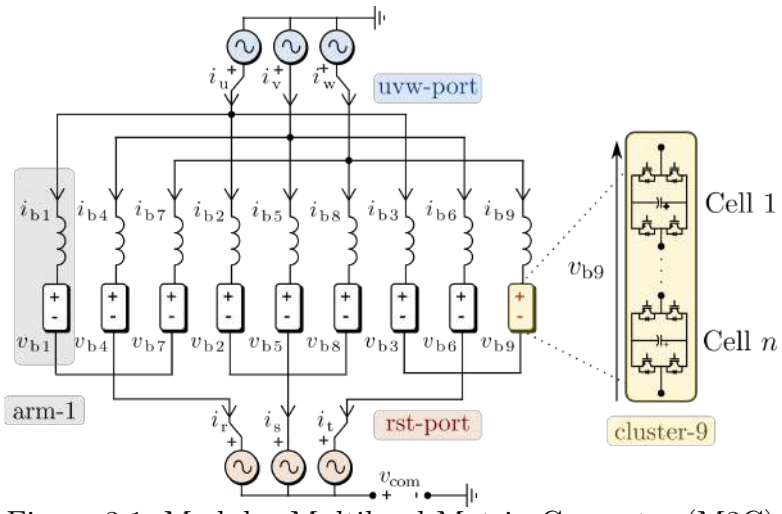

Figure 3.1: Modular Multilevel Matrix Converter (M3C).

and (b) Power/CCV Model.

3.1. Current/Voltage Model of the M3C

According to Figure 3.1, the dynamics of the arm currents are defined by the Kirchhoff's voltage law with the following matrix representation

$$\underbrace{\frac{\mathrm{d}}{\mathrm{d}t}\begin{bmatrix} \mathrm{i_{b1}} \\ \mathrm{i_{b2}} \\ \mathrm{i_{b3}} \\ \mathrm{i_{b4}} \\ \mathrm{i_{b5}} \\ \mathrm{i_{b6}} \\ \mathrm{i_{b7}} \\ \mathrm{i_{b8}} \\ \mathrm{i_{b9}} \end{bmatrix}}_{\mathbf{i}_\mathrm{b}} = \frac{1}{\mathrm{L_b}} \underbrace{\begin{bmatrix} 1 & 0 & 0 & -1 & 0 & 0 \\ 1 & 0 & 0 & 0 & -1 & 0 \\ 1 & 0 & 0 & 0 & 0 & -1 \\ 0 & 1 & 0 & -1 & 0 & 0 \\ 0 & 1 & 0 & 0 & -1 & 0 \\ 0 & 1 & 0 & 0 & 0 & -1 \\ 0 & 0 & 1 & -1 & 0 & 0 \\ 0 & 0 & 1 & 0 & -1 & 0 \\ 0 & 0 & 1 & 0 & 0 & -1 \end{bmatrix}}_{\mathbf{\Lambda}_\mathrm{v}} \underbrace{\begin{bmatrix} v_\mathrm{u} \\ v_\mathrm{v} \\ v_\mathrm{w} \\ v_\mathrm{r} \\ v_\mathrm{s} \\ v_\mathrm{t} \end{bmatrix}}_{\boldsymbol{v}_\mathrm{rst}^\mathrm{uvw}} - \frac{1}{\mathrm{L_b}} \underbrace{\begin{bmatrix} v_\mathrm{b1} \\ v_\mathrm{b2} \\ v_\mathrm{b3} \\ v_\mathrm{b4} \\ v_\mathrm{b5} \\ v_\mathrm{b6} \\ v_\mathrm{b7} \\ v_\mathrm{b8} \\ v_\mathrm{b9} \end{bmatrix}}_{\boldsymbol{v}_\mathrm{b}} - \frac{1}{\mathrm{L_b}} \underbrace{\begin{bmatrix} 1 \\ 1 \\ 1 \\ 1 \\ 1 \\ 1 \\ 1 \\ 1 \\ 1 \end{bmatrix}}_{\mathbf{1}} v_\mathrm{com} \tag{3.1}$$

where the input/output ports are defined by phases uvw and rst terminals, respectively, and $\boldsymbol{v}_\mathrm{b}$ is the vector that contains the output voltages of the clusters.

In order to define the input and load currents with the branch currents, the Kirchhoff's current law is applied to each output node, with the following matrix representation

$$\mathbf{i}_\mathrm{rst}^\mathrm{uvw} = \underbrace{\begin{bmatrix} 1 & 1 & 1 & 0 & 0 & 0 & 0 & 0 & 0 \\ 0 & 0 & 0 & 1 & 1 & 1 & 0 & 0 & 0 \\ 0 & 0 & 0 & 0 & 0 & 0 & 1 & 1 & 1 \\ 1 & 0 & 0 & 1 & 0 & 0 & 1 & 0 & 0 \\ 0 & 1 & 0 & 0 & 1 & 0 & 0 & 1 & 0 \\ 0 & 0 & 1 & 0 & 0 & 1 & 0 & 0 & 1 \end{bmatrix}}_{\mathbf{\Lambda}_\mathrm{i}} \mathbf{i}_\mathrm{b} \tag{3.2}$$

where $\mathbf{i}_\mathrm{rst}^\mathrm{uvw} = \begin{bmatrix} \mathrm{i_u} & \mathrm{i_v} & \mathrm{i_w} & \mathrm{i_r} & \mathrm{i_s} & \mathrm{i_t} \end{bmatrix}^\mathrm{T}$.

It can be directly proved that $\mathrm{rank}(\mathbf{\Lambda}_\mathrm{i}) = 5$, and therefore its null-space is four ($\dim\{\mathrm{null}(\mathbf{\Lambda}_\mathrm{i})\} = 4$). The dimension of the null space means that there are four independent current paths which do not interfere with the output's current paths of the converter (specified by $\mathbf{\Lambda}_\mathrm{i}$) [78]. These degrees of freedom play a key-role in the overall control of the M3C, where they are commonly known as *circulating currents*, and are mainly used for regulation of the capacitor-voltages of the converter.

3.1.1. Linear Transform and Reinterpretation of the Variables

With the definition of $\mathbf{\Lambda}_{\mathrm{i}}$, the dynamics of the input/output port and the circulating currents can be conveniently reinterpreted with a proper linear transformation. The definition of the circulating currents can also be considered as a degree of freedom, where different compositions have been proposed and analysed, such as the presented in [22, 23]. For this work, the definition of the transform applied to (3.1) is derived from [22], which is rewritten into the following matrix representation:

$$\underbrace{\begin{bmatrix} \mathrm{i}_{\alpha 1} \\ \mathrm{i}_{\beta 1} \\ \mathrm{i}_{\alpha 2} \\ \mathrm{i}_{\beta 2} \\ \mathrm{i}_{0} \\ \mathrm{i}_{\varepsilon 1} \\ \mathrm{i}_{\varepsilon 2} \\ \mathrm{i}_{\varepsilon 3} \\ \mathrm{i}_{\varepsilon 4} \end{bmatrix}}_{\mathbf{i}_{\alpha\beta 0\varepsilon}} = \underbrace{\frac{1}{6}\begin{bmatrix} 2 & 2 & 2 & -1 & -1 & -1 & -1 & -1 & -1 \\ 0 & 0 & 0 & \sqrt{3} & \sqrt{3} & \sqrt{3} & -\sqrt{3} & -\sqrt{3} & -\sqrt{3} \\ 2 & -1 & -1 & 2 & -1 & -1 & 2 & -1 & -1 \\ 0 & \sqrt{3} & -\sqrt{3} & 0 & \sqrt{3} & -\sqrt{3} & 0 & \sqrt{3} & -\sqrt{3} \\ 2 & 2 & 2 & 2 & 2 & 2 & 2 & 2 & 2 \\ 2 & -1 & -1 & -1 & -1 & 2 & -1 & 2 & -1 \\ 0 & -\sqrt{3} & \sqrt{3} & -\sqrt{3} & \sqrt{3} & 0 & \sqrt{3} & 0 & -\sqrt{3} \\ 2 & -1 & -1 & -1 & 2 & -1 & -1 & -1 & 2 \\ 0 & -\sqrt{3} & \sqrt{3} & \sqrt{3} & 0 & -\sqrt{3} & -\sqrt{3} & \sqrt{3} & 0 \end{bmatrix}}_{\mathbf{T}_{\alpha\beta 0\varepsilon}} \mathbf{i}_{\mathrm{b}} \tag{3.3}$$

The used transform allows a decoupling of the oscillating stored energy frequency components as it will be introduced in the incoming section 3.3. This feature is used conveniently in the definition of the proposed control strategy, allowing a clear definition of the working zones of the M3C. Pre-multiplying the expression (3.1) by the matrix specified in (3.3), the following voltage/current dynamic equation is obtained:

$$\underbrace{\frac{\mathrm{d}}{\mathrm{d}t}\begin{bmatrix} \mathrm{i}_{\alpha 1} \\ \mathrm{i}_{\beta 1} \\ \mathrm{i}_{\alpha 2} \\ \mathrm{i}_{\beta 2} \\ \mathrm{i}_{0} \\ \mathrm{i}_{\varepsilon 1} \\ \mathrm{i}_{\varepsilon 2} \\ \mathrm{i}_{\varepsilon 3} \\ \mathrm{i}_{\varepsilon 4} \end{bmatrix}}_{\mathbf{i}_{\alpha\beta 0\varepsilon}} = \frac{1}{\mathrm{L_b}}\begin{bmatrix} 3 & 0 & 0 & 0 & 0 & 0 \\ 0 & 3 & 0 & 0 & 0 & 0 \\ 0 & 0 & 0 & -3 & 0 & 0 \\ 0 & 0 & 0 & 0 & -3 & 0 \\ 0 & 0 & 3 & 0 & 0 & -3 \\ 0 & 0 & 0 & 0 & 0 & 0 \\ 0 & 0 & 0 & 0 & 0 & 0 \\ 0 & 0 & 0 & 0 & 0 & 0 \\ 0 & 0 & 0 & 0 & 0 & 0 \end{bmatrix} \begin{bmatrix} v^{o}_{\alpha 1} \\ v^{o}_{\beta 1} \\ v^{o}_{01} \\ v^{o}_{\alpha 2} \\ v^{o}_{\beta 2} \\ v^{o}_{02} \end{bmatrix} - \frac{1}{\mathrm{L_b}}\underbrace{\begin{bmatrix} v_{\alpha 1} \\ v_{\beta 1} \\ v_{\alpha 2} \\ v_{\beta 2} \\ v_{0} \\ v_{\varepsilon 1} \\ v_{\varepsilon 2} \\ v_{\varepsilon 3} \\ v_{\varepsilon 4} \end{bmatrix}}_{\boldsymbol{v}_{\alpha\beta 0\varepsilon}} - \frac{1}{\mathrm{L_b}}\begin{bmatrix} 0 \\ 0 \\ 0 \\ 0 \\ 3 \\ 0 \\ 0 \\ 0 \\ 0 \end{bmatrix} v_{\mathrm{com}} \tag{3.4}$$

where, for avoiding complexity in the nomenclature, the ports "uvw" and "rst" are replaced with "1" and "2", respectively. In addition, the voltages related with the output ports (loads) have a superscript "o". The corresponding equivalent circuit of the transformed M3C current dynamic equations is shown in 3.2.

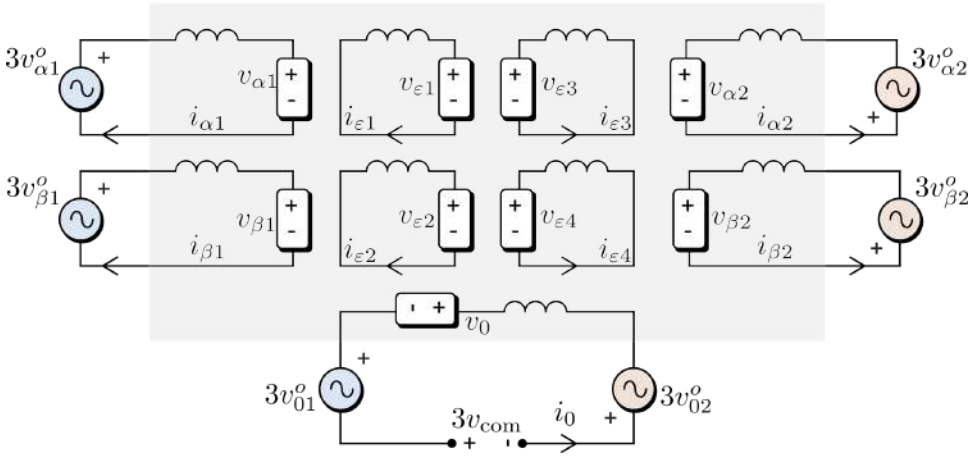

Figure 3.2: M3C decoupled circuit modelling.

3.2. Voltage/Power Model of the M3C

To regulate the nine Cluster Capacitor Voltages (CCVs) of the M3C, a dynamic model that considers the sum of the square of the capacitor voltages for each arm, with their corresponding output power, is introduced.

Assuming that the capacitance of all power-cells are equal, the stored energy of the i-th cluster is determined by,

$$W_{\mathrm{Ci}} = \frac{1}{2}\mathrm{C}\underbrace{\sum_{r=1}^{n}(v_{\mathrm{C}r}^{\mathrm{i}})^2}_{\psi_{\mathrm{Cbi}}} \tag{3.5}$$

where n is the number of power-cells in each cluster, C is the cell capacitance, $v_{\mathrm{C}r}^{\mathrm{i}}$ is the r-th cell capacitor voltage belonging to the i-th cluster and ψ_{Cbi} is conveniently defined as the Sum of the Squares of the Capacitor Voltages (SSCV).

Considering that the output power of each cluster is equal to the derivative of its respective stored energy, the following linear relationship is obtained,

$$\frac{\mathrm{d}}{\mathrm{d}t}\underbrace{\begin{bmatrix}\psi_{\mathrm{Cb1}}\\ \psi_{\mathrm{Cb2}}\\ \psi_{\mathrm{Cb3}}\\ \psi_{\mathrm{Cb4}}\\ \psi_{\mathrm{Cb5}}\\ \psi_{\mathrm{Cb6}}\\ \psi_{\mathrm{Cb7}}\\ \psi_{\mathrm{Cb8}}\\ \psi_{\mathrm{Cb9}}\end{bmatrix}}_{\boldsymbol{\psi}_{\mathrm{C}b}} = \frac{2}{\mathrm{C}}\underbrace{\begin{bmatrix}p_{\mathrm{b1}}\\ p_{\mathrm{b2}}\\ p_{\mathrm{b3}}\\ p_{\mathrm{b4}}\\ p_{\mathrm{b5}}\\ p_{\mathrm{b6}}\\ p_{\mathrm{b7}}\\ p_{\mathrm{b8}}\\ p_{\mathrm{b9}}\end{bmatrix}}_{\boldsymbol{p}_{\mathrm{b}}} \tag{3.6}$$

where $p_{\mathrm{bi}} = v_{\mathrm{bi}}\mathrm{i}_{\mathrm{bi}}\ \forall \mathrm{i} \in \{1, ..., 9\}$, with i_{bi} and v_{bi} as, respectively, the arm current and the i-th output cluster voltage. This approach allows us to treat the stored energy of each arm as an equivalent single power cell, where its voltage is the square-root of its SSCV (i.e $v_{\mathrm{Cbi}}=\sqrt{\sum_{r=1}^{n}(v_{\mathrm{C}r}^{\mathrm{i}})^2}$). Therefore, if there exists a proper balance among the capacitor voltage of each cluster, the analysis of an n-cell cluster can directly simplified to an equivalent single power cell per arm.

It is important to remark that if the control of the CCVs is realised using $\boldsymbol{\psi}_{\mathrm{C}b}$ rather than the capacitor voltages directly, no small-signal models, like those used in [24, 13], are required to define a linear plant.

Applying the $\mathbf{T}_{\alpha\beta 0\varepsilon}$ transform in (3.6),

$$\frac{\mathrm{d}}{\mathrm{d}t}\underbrace{\begin{bmatrix}\psi_{\mathrm{C}_{\alpha 1}}\\ \psi_{\mathrm{C}_{\beta 1}}\\ \psi_{\mathrm{C}_{\alpha 2}}\\ \psi_{\mathrm{C}_{\beta 2}}\\ \psi_{\mathrm{C}_{0}}\\ \psi_{\mathrm{C}_{\varepsilon 1}}\\ \psi_{\mathrm{C}_{\varepsilon 2}}\\ \psi_{\mathrm{C}_{\varepsilon 3}}\\ \psi_{\mathrm{C}_{\varepsilon 4}}\end{bmatrix}}_{\boldsymbol{\psi}_{\mathrm{C}\alpha\beta\varepsilon}} = \frac{2}{\mathrm{C}}\begin{bmatrix}p_{\alpha 1}\\ p_{\beta 1}\\ p_{\alpha 2}\\ p_{\beta 2}\\ p_{0}\\ p_{\varepsilon 1}\\ p_{\varepsilon 2}\\ p_{\varepsilon 3}\\ p_{\varepsilon 4}\end{bmatrix} \tag{3.7}$$

where relationship among the transformed SSCV variables (T-SSCV) is straightforward by observing them in an ideal condition [13]. If all capacitor voltages have the magnitude $v_{\mathrm{C}}^{\mathrm{ref}}$,the following T-SSCV values are obtained:

$$\begin{bmatrix}\psi_{\mathrm{C}_{\alpha 1}}^{\mathrm{ref}}\\ \psi_{\mathrm{C}_{\beta 1}}^{\mathrm{ref}}\\ \psi_{\mathrm{C}_{\alpha 2}}^{\mathrm{ref}}\\ \psi_{\mathrm{C}_{\beta 2}}^{\mathrm{ref}}\\ \psi_{\mathrm{C}_{0}}^{\mathrm{ref}}\\ \psi_{\mathrm{C}_{\varepsilon 1}}^{\mathrm{ref}}\\ \psi_{\mathrm{C}_{\varepsilon 2}}^{\mathrm{ref}}\\ \psi_{\mathrm{C}_{\varepsilon 3}}^{\mathrm{ref}}\\ \psi_{\mathrm{C}_{\varepsilon 4}}^{\mathrm{ref}}\end{bmatrix} = \begin{bmatrix}0\\ 0\\ 0\\ 0\\ 3n(v_{\mathrm{C}}^{\mathrm{ref}})^2\\ 0\\ 0\\ 0\\ 0\end{bmatrix} \tag{3.8}$$

where the energy term ψ_{C_0} is directly related to the total stored energy in the M3C due to it being the sum of the squared capacitor voltages; on the other hand, the remaining eight transformed terms are interpreted as a measurement of the distribution of the stored energy among the nine clusters [23, 13].

Regarding the plant of ψ_{C_0}, it is defined by p_0 [equation (3.7)], which has the following composition,

$$p_0 = \frac{1}{3}p_1 + \frac{1}{3}p_2 \tag{3.9}$$

where $p_1{=}2\Re\left\{\dot{\boldsymbol{v}}_1\dot{\mathbf{i}}_1^c\right\}$ and $p_2{=}2\Re\left\{\dot{\boldsymbol{v}}_2\dot{\mathbf{i}}_2^c\right\}$ are, respectively, the uvw and rst instantaneous port power, and $\dot{\boldsymbol{v}}_1{=}v_{\alpha 1}{+}jv_{\beta 1}$, $\dot{\boldsymbol{v}}_2{=}v_{\alpha 2}{+}jv_{\beta 2}$, $\dot{\mathbf{i}}_1{=}\mathrm{i}_{\alpha 1}{+}j\mathrm{i}_{\beta 1}$ with $\dot{\mathbf{i}}_2{=}\mathrm{i}_{\alpha 2}{+}j\mathrm{i}_{\beta 2}$ are the transformed input/output port cluster output voltages and currents in complex notation.

The dynamic relationships of the remaining eight T-SSCV variables is given in the following matrix formulation:

$$\frac{\mathrm{d}}{\mathrm{d}t}\boldsymbol{\psi}_{\mathrm{C}\alpha\beta\varepsilon} = \boldsymbol{B}_{\mathrm{C}}(t)\mathbf{i}_{\varepsilon} + \mathbf{d}_{\mathrm{C}}(t) \tag{3.10}$$

where $\mathbf{i}_{\varepsilon}=[\mathrm{i}_{\varepsilon 1}\ \mathrm{i}_{\varepsilon 2}\ \mathrm{i}_{\varepsilon 3}\ \mathrm{i}_{\varepsilon 4}]^T$,

$$\boldsymbol{B}_{\mathrm{C}}(t)=\frac{2}{3\mathrm{C}}\begin{bmatrix} v_{\alpha 2} & -v_{\beta 2} & v_{\alpha 2} & -v_{\beta 2} \\ -v_{\beta 2} & -v_{\alpha 2} & v_{\beta 2} & v_{\alpha 2} \\ v_{\alpha 1} & -v_{\beta 1} & v_{\alpha 1} & v_{\beta 1} \\ -v_{\beta 1} & -v_{\alpha 1} & v_{\beta 1} & -v_{\alpha 1} \\ v_0 & 0 & v_{\alpha 1}+v_{\alpha 2} & -v_{\beta 1}+v_{\beta 2} \\ 0 & v_0 & v_{\beta 1}+v_{\beta 2} & v_{\alpha 1}-v_{\alpha 2} \\ v_{\alpha 1}+v_{\alpha 2} & v_{\beta 1}+v_{\beta 2} & v_0 & 0 \\ -v_{\beta 1}+v_{\beta 2} & v_{\alpha 1}-v_{\alpha 2} & 0 & v_0 \end{bmatrix} \tag{3.11}$$

and

$$\mathbf{d}_{\mathrm{C}}(t)=\frac{2}{3\mathrm{C}}\begin{bmatrix} v_o+v_{\alpha 1} & -v_{\beta 1} & 0 & 0 \\ -v_{\beta 1} & v_0-v_{\alpha 1} & 0 & 0 \\ 0 & 0 & v_o+v_{\alpha 2} & -v_{\beta 2} \\ 0 & 0 & -v_{\beta 2} & v_0-v_{\alpha 2} \\ v_{\alpha 2} & -v_{\beta 2} & v_{\alpha 1} & -v_{\beta 1} \\ -v_{\beta 2} & -v_{\alpha 2} & -v_{\beta 1} & -v_{\alpha 1} \\ v_{\alpha 2} & v_{\beta 2} & v_{\alpha 1} & v_{\beta 1} \\ -v_{\beta 2} & v_{\alpha 2} & v_{\beta 1} & -v_{\alpha 1} \end{bmatrix} \underbrace{\begin{bmatrix} \mathrm{i}_{\alpha 1} \\ \mathrm{i}_{\beta 1} \\ \mathrm{i}_{\alpha 2} \\ \mathrm{i}_{\beta 2} \end{bmatrix}}_{\mathbf{i}_{\alpha\beta 12}} \tag{3.12}$$

As will be shown in the control scheme section, (Section 6.1.1), this formulation allows an easier utilisation of a Model Predictive Control strategy for regulating the T-SSCV.

3.2.1. T-SSCV Dynamic Model in Complex Form

The matrix modelling shown in (3.10) can be rewritten into a convenient complex form, where the transformed power complex variables are defined as $\dot{\boldsymbol{p}}_{\alpha\beta 1}=p_{\alpha 1}+jp_{\beta 1}$, $\dot{\boldsymbol{p}}_{\alpha\beta 2}=p_{\alpha 2}+jp_{\beta 2}$, $\dot{\boldsymbol{p}}_{\varepsilon 12}=p_{\varepsilon 1}+jp_{\varepsilon 2}$ and $\dot{\boldsymbol{p}}_{\varepsilon 34}=p_{\varepsilon 3}+jp_{\varepsilon 4}$.

Replacing the arm currents and output cluster voltages with their corresponding transformed variables, the following complex power relations arise [21]:

$$\begin{aligned} \dot{\boldsymbol{p}}_{\varepsilon 12} &= \frac{1}{3}\left(\dot{\mathbf{i}}_2^*\dot{\boldsymbol{v}}_1^*+\dot{\mathbf{i}}_1^*\dot{\boldsymbol{v}}_2^*\right)+\frac{1}{3}(\dot{\boldsymbol{v}}_2\dot{\mathbf{i}}_{\varepsilon 34}^*+\dot{\boldsymbol{v}}_1\dot{\mathbf{i}}_{\varepsilon 34})+\frac{1}{3}v_o\dot{\mathbf{i}}_{\varepsilon 12} \\ \dot{\boldsymbol{p}}_{\varepsilon 34} &= \frac{1}{3}\left(\dot{\mathbf{i}}_2^*\dot{\boldsymbol{v}}_1+\dot{\mathbf{i}}_1\dot{\boldsymbol{v}}_2^*\right)+\frac{1}{3}(\dot{\boldsymbol{v}}_2\dot{\mathbf{i}}_{\varepsilon 12}^*+\dot{\boldsymbol{v}}_1^*\dot{\mathbf{i}}_{\varepsilon 12})+\frac{1}{3}v_o\dot{\mathbf{i}}_{\varepsilon 34} \\ \dot{\boldsymbol{p}}_{\alpha\beta 1} &= \frac{1}{3}\dot{\boldsymbol{v}}_1^*\dot{\mathbf{i}}_1^*+\frac{1}{3}\left(\dot{\boldsymbol{v}}_2^*\dot{\mathbf{i}}_{\varepsilon 12}^*+\dot{\boldsymbol{v}}_2\dot{\mathbf{i}}_{\varepsilon 34}\right)+\frac{1}{3}\dot{\mathbf{i}}_1 v_0 \\ \dot{\boldsymbol{p}}_{\alpha\beta 2} &= \frac{1}{3}\dot{\boldsymbol{v}}_2^*\dot{\mathbf{i}}_2^*+\frac{1}{3}\left(\dot{\boldsymbol{v}}_1^*\dot{\mathbf{i}}_{\varepsilon 12}^*+\dot{\boldsymbol{v}}_1\dot{\mathbf{i}}_{\varepsilon 34}^*\right)+\frac{1}{3}\dot{\mathbf{i}}_2 v_0 \end{aligned} \tag{3.13}$$

and the following dynamic equations are the starting point for the traditional vector control of the CCVs:

$$
\begin{aligned}
\frac{\mathrm{d}\dot{\boldsymbol{\psi}}_{\mathrm{C}_{\alpha\beta 1}}}{\mathrm{d}t} &= \frac{2}{\mathrm{C}}\dot{\boldsymbol{p}}_{\alpha\beta 1} \\
\frac{\mathrm{d}\dot{\boldsymbol{\psi}}_{\mathrm{C}_{\alpha\beta 2}}}{\mathrm{d}t} &= \frac{2}{\mathrm{C}}\dot{\boldsymbol{p}}_{\alpha\beta 2} \\
\frac{\mathrm{d}\dot{\boldsymbol{\psi}}_{\mathrm{C}_{\varepsilon 12}}}{\mathrm{d}t} &= \frac{2}{\mathrm{C}}\dot{\boldsymbol{p}}_{\varepsilon 12} \\
\frac{\mathrm{d}\dot{\boldsymbol{\psi}}_{\mathrm{C}_{\varepsilon 34}}}{\mathrm{d}t} &= \frac{2}{\mathrm{C}}\dot{\boldsymbol{p}}_{\varepsilon 34}
\end{aligned}
\tag{3.14}
$$

with $\dot{\boldsymbol{\psi}}_{\mathrm{C}\alpha\beta 1}=\psi_{\mathrm{C}\alpha 1}+j\psi_{\mathrm{C}\beta 1}$, $\dot{\boldsymbol{\psi}}_{\mathrm{C}\alpha\beta 2}=\psi_{\mathrm{C}\alpha 2}+j\psi_{\mathrm{C}\beta 2}$, $\dot{\boldsymbol{\psi}}_{\mathrm{C}\varepsilon 12}=\psi_{\mathrm{C}\varepsilon 1}+j\psi_{\mathrm{C}\varepsilon 2}$ and $\dot{\boldsymbol{\psi}}_{\mathrm{C}\varepsilon 34}=\psi_{\mathrm{C}\varepsilon 3}+j\psi_{\mathrm{C}\varepsilon 4}$

3.3. Steady-state Capacitor Voltage Oscillations in the M3C

Due to the power cells are composed of floating capacitors, the output port power oscillations are transferred to the DC side voltages, where their amplitudes can be naturally filtered in most cases. The effectiveness of the natural filtering of the oscillations depends on the frequency and amplitude of the power components and the capacitance of the cells. However, depending on the working conditions at both AC ports of the M3C, the power components still can lead to undesirable voltage oscillations, leading to an unstable operation of the converter. Specifically, the working conditions that originate low-frequency power oscillations are considered the source of an unstable operation, due to the natural filtering is not enough to mitigate the voltage fluctuations.

This section defines the critical AC port frequency ranges of the M3C. The presented analysis starts from a general definition, assuming balanced operation at both the input/output ports and the capacitor voltages of all arms are locally balanced. These considerations simplify the overall analysis, where the definition of the T-SSCVs is enough to specify the critical frequency ranges because they are a linear combination of the SSCVs. Moreover, the SSCVs are a direct measurement of the CCVs according to (3.5). This implies that knowing the behaviour of the T-SSCVs, the overall status of the M3C can be specified.

3.3.1. Steady State T-SSCV Oscillations in the M3C

Assuming steady operation with symmetrical and balanced conditions, the following transformed port currents and voltages are defined:

$$\begin{bmatrix} \mathrm{i}_{\alpha 1} \\ \mathrm{i}_{\beta 1} \\ \mathrm{i}_{\alpha 2} \\ \mathrm{i}_{\beta 2} \end{bmatrix} = \begin{bmatrix} \mathrm{I}_1 \cos\left(\omega_1 t + \phi_{\mathrm{i}1}\right) \\ \mathrm{I}_1 \sin\left(\omega_1 t + \phi_{\mathrm{i}1}\right) \\ \mathrm{I}_2 \cos\left(\omega_2 t + \phi_{\mathrm{i}2}\right) \\ \mathrm{I}_2 \sin\left(\omega_2 t + \phi_{\mathrm{i}2}\right) \end{bmatrix} \quad \begin{bmatrix} v_{\alpha 1} \\ v_{\beta 1} \\ v_{\alpha 2} \\ v_{\beta 2} \end{bmatrix} = \begin{bmatrix} \mathrm{V}_1 \cos\left(\omega_1 t + \phi_{v1}\right) \\ \mathrm{V}_1 \sin\left(\omega_1 t + \phi_{v1}\right) \\ \mathrm{V}_2 \cos\left(\omega_2 t + \phi_{v2}\right) \\ \mathrm{V}_2 \sin\left(\omega_2 t + \phi_{v2}\right) \end{bmatrix} \tag{3.15}$$

where the frequencies ω_1 and ω_2 are not limited in magnitude or sign. The complex form of (3.15) is depicted below,

$$\dot{\boldsymbol{v}}_1 = \dot{V}_1 \mathrm{e}^{j\omega_1 t}, \quad \dot{\mathbf{i}}_1 = \dot{I}_1 \mathrm{e}^{j\omega_1 t} \tag{3.16}$$

$$\dot{\boldsymbol{v}}_2 = \dot{V}_2 \mathrm{e}^{j\omega_2 t}, \quad \dot{\mathbf{i}}_2 = \dot{I}_2 \mathrm{e}^{j\omega_2 t} \tag{3.17}$$

with $\dot{V}_1 = \mathrm{V}_1 \mathrm{e}^{j\phi_{v1}}$, $\dot{I}_1 = \mathrm{I}_1 \mathrm{e}^{j\phi_{\mathrm{i}1}}$, $\dot{V}_2 = \mathrm{V}_2 \mathrm{e}^{j\phi_{v2}}$ and $\dot{I}_2 = \mathrm{I}_2 \mathrm{e}^{j\phi_{\mathrm{i}2}}$.

Additionally, it is assumed that,

$$v_0 = \mathrm{V}_0 \cos(\omega_0 t + \phi_0) \tag{3.18}$$

where the frequency ω_0 is usually much higher than the input/output port frequencies ($|\omega_0| >> |\omega_1|$ and $|\omega_0| >> |\omega_2|$) [21]. Note that the variable v_0 is related to the traditional

definition of the M3C Common-mode Voltage (CMV) used in [21] by,

$$v_0{=}3 \cdot \mathrm{CMV} \tag{3.19}$$

According to the expression shown in (3.10), steady state operation of the M3C naturally induces undesirable oscillations in the capacitor voltages. Specifically, the origin of these oscillations is directly linked with the disturbance vector $\mathbf{d}_{\mathrm{C}}(t)$ defined in (3.12), which is exclusively composed of the input/output port voltages/currents and the common-mode voltage. Replacing the values established in (3.15) and (3.18) into the definition of $\mathbf{d}_{\mathrm{C}}(t)$, the following T-SSCV oscillating components are defined:

$$\begin{aligned} \tilde{\boldsymbol{\psi}}_{\alpha\beta\varepsilon}(t) &= \int \mathbf{d}_{\mathrm{C}}(t)\mathrm{d}t \\ &= \tilde{\boldsymbol{\psi}}^{12}_{\alpha\beta\varepsilon}(t) + \tilde{\boldsymbol{\psi}}^{0}_{\alpha\beta\varepsilon}(t) \end{aligned} \tag{3.20}$$

where

$$\tilde{\boldsymbol{\psi}}^{12}_{\alpha\beta\varepsilon}(t){=}\ \tfrac{2}{3\mathrm{C}} \begin{bmatrix} \frac{1}{2\omega_1}\mathrm{P}_1 \sin(2\omega_1 t{+}\phi_1) \\ \frac{1}{2\omega_1}\mathrm{P}_1 \cos(2\omega_1 t{+}\phi_1) \\ \frac{1}{2\omega_2}\mathrm{P}_2 \sin(2\omega_2 t{+}\phi_2) \\ \frac{1}{2\omega_2}\mathrm{P}_2 \cos(2\omega_2 t{+}\phi_2) \\ \frac{1}{\omega_1{+}\omega_2}\mathrm{P}^{+}_{12} \sin\big([\omega_1{+}\omega_2]t{+}\phi^{+}_{12}\big) \\ \frac{1}{\omega_1{+}\omega_2}\mathrm{P}^{+}_{12} \cos\big([\omega_1{+}\omega_2]t{+}\phi^{+}_{12}\big) \\ \frac{1}{\omega_1{-}\omega_2}\mathrm{P}^{-}_{12} \sin\big([\omega_1{\text{-}}\omega_2]t{+}\phi^{-}_{12}\big) \\ \frac{-1}{\omega_1{-}\omega_2}\mathrm{P}^{-}_{12} \cos\big([\omega_1{\text{-}}\omega_2]t{+}\phi^{-}_{12}\big) \end{bmatrix} \tag{3.21}$$

is the energy oscillation vector induced by the input/output port voltages and currents exclusively, with $\mathrm{P}_1{=}\mathrm{V}_1\mathrm{I}_1$, $\mathrm{P}_2{=}\mathrm{V}_2\mathrm{I}_2$, $\phi_1{=}\phi_{\mathrm{i}1}{+}\phi_{v1}$ and $\phi_2{=}\phi_{\mathrm{i}2}{+}\phi_{v2}$. Additionally, the following complex relations define the remaining parameters:

$$\begin{aligned} \mathrm{P}^{+}_{12}\mathrm{e}^{j\phi^{+}_{12}}{=}[\mathrm{V}_1(\mathrm{I}_{\mathrm{d}2}{-}j\mathrm{I}_{\mathrm{q}2}){+}\mathrm{V}_2(\mathrm{I}_{\mathrm{d}1}{-}j\mathrm{I}_{\mathrm{q}1})]\mathrm{e}^{\text{-}j(\phi_{v1}+\phi_{v2})} \\ \mathrm{P}^{-}_{12}\mathrm{e}^{j\phi^{-}_{12}}{=}[\mathrm{V}_1(\mathrm{I}_{\mathrm{d}2}{-}j\mathrm{I}_{\mathrm{q}2}){+}\mathrm{V}_2(\mathrm{I}_{\mathrm{d}1}{+}j\mathrm{I}_{\mathrm{q}1})]\mathrm{e}^{\text{-}j(\text{-}\phi_{v1}+\phi_{v2})} \end{aligned} \tag{3.22}$$

with

$$\begin{bmatrix}\mathrm{I}_{\mathrm{d}1}\\ \mathrm{I}_{q1}\end{bmatrix} = \begin{bmatrix}\mathrm{I}_1\cos(\phi_{\mathrm{i}1}{-}\phi_{v1})\\ \mathrm{I}_1\sin(\phi_{\mathrm{i}1}{-}\phi_{v1})\end{bmatrix} \text{ and } \begin{bmatrix}\mathrm{I}_{\mathrm{d}2}\\ \mathrm{I}_{q2}\end{bmatrix} = \begin{bmatrix}\mathrm{I}_2\cos(\phi_{\mathrm{i}2}{-}\phi_{v2})\\ \mathrm{I}_2\sin(\phi_{\mathrm{i}2}{-}\phi_{v2})\end{bmatrix}$$

as the input/output port currents in synchronous reference frames oriented with the input/output port voltage phase, respectively.

Furthermore, the T-SSCV oscillations related to the interaction between the

Table 3.1: Affected transformed energy terms due to specific frequency operation in input and output ports.

Critical Range	$\omega_1 \approx 0$	$\omega_2 \approx 0$	$\omega_1 \approx -\omega_2$	$\omega_1 \approx \omega_2$
Affected Energy Terms	$\psi_{C_{\alpha 1}}$-$\psi_{C_{\beta 1}}$	$\psi_{C_{\alpha 2}}$-$\psi_{C_{\beta 2}}$	$\psi_{C_{\varepsilon 1}}$-$\psi_{C_{\varepsilon 2}}$	$\psi_{C_{\varepsilon 3}}$-$\psi_{C_{\varepsilon 4}}$

common-mode voltage with the input/output port currents are described by,

$$\tilde{\boldsymbol{\psi}}^{0}_{\alpha\beta\varepsilon}(t)=\frac{2}{3\mathrm{C}}\begin{bmatrix} \frac{\mathrm{P}_{01}}{\omega_0+\omega_1}\sin\left([\omega_0+\omega_1]t+\phi^{+}_{01}\right)+\frac{\mathrm{P}_{01}}{\omega_0-\omega_1}\sin\left([\omega_0-\omega_1]t+\phi^{-}_{01}\right) \\ \frac{-\mathrm{P}_{01}}{\omega_0+\omega_1}\cos\left([\omega_0+\omega_1]t+\phi^{+}_{01}\right)+\frac{\mathrm{P}_{01}}{\omega_0-\omega_1}\cos\left([\omega_0-\omega_1]t+\phi^{-}_{01}\right) \\ \frac{\mathrm{P}_{02}}{\omega_0+\omega_2}\sin\left([\omega_0+\omega_2]t+\phi^{+}_{02}\right)+\frac{\mathrm{P}_{02}}{\omega_0-\omega_2}\sin\left([\omega_0-\omega_2]t+\phi^{-}_{02}\right) \\ \frac{-\mathrm{P}_{02}}{\omega_0+\omega_2}\cos\left([\omega_0+\omega_2]t+\phi^{+}_{02}\right)+\frac{\mathrm{P}_{02}}{\omega_0-\omega_2}\cos\left([\omega_0-\omega_2]t+\phi^{-}_{02}\right) \\ 0 \\ 0 \\ 0 \\ 0 \end{bmatrix}$$

where $\mathrm{P}_{01}=\mathrm{V}_0\mathrm{I}_1$, $\mathrm{P}_{02}=\mathrm{V}_0\mathrm{I}_2$, $\phi^{+}_{01}=\phi_0+\phi_{\mathrm{i}1}$, $\phi^{-}_{01}=\phi_0-\phi_{\mathrm{i}1}$, $\phi^{+}_{02}=\phi_0+\phi_{\mathrm{i}2}$, and $\phi^{-}_{02}=\phi_0-\phi_{\mathrm{i}1}$.

As shown in the results, an undesirable increase of the T-SSCVs oscillating components is caused for specific values of the input/output port frequencies. These values with the affected T-SSCV pair are shown in Table 3.1. Assuming that the condition of $|\omega_0| >> |\omega_1|$ and $|\omega_0| >> |\omega_2|$ are accomplished,the oscillating components of $\tilde{\boldsymbol{\psi}}^{0}_{\alpha\beta\varepsilon}(t)$ are neglected. This assumption relies on the natural behaviour of the capacitor voltage dynamics, where high frequency power components are naturally mitigated and, therefore, their impact is negligible.

Regarding the M3C implementation, some of the critical operation ranges can be neglected because they are infeasible in normal conditions. Assuming that the M3C is connected to a balanced utility grid in the rst port, the operation $\omega_2 \approx 0$ is not feasible and no further analysis in this critical region is presented. Additionally, the operation of the uvw load side near zero frequency, $\omega_1 \approx 0$, can be critical when the demanded power is important in such operating range, like high-torque low-frequency drives as presented in [25]. It is important to remark that this sort of machine operation has not been considered in the presented work and no further analysis will be shown.

With the aforementioned considerations, the studied critical operation ranges are focused on uvw/output port operation at Equal Frequencies Mode (EFM) [21], which, depending on the phase-sequence in the output port, can be either the $\{\psi_{C_{\varepsilon 1}},\ \psi_{C_{\varepsilon 2}}\}$ or the $\{\psi_{C_{\varepsilon 3}},\ \psi_{C_{\varepsilon 4}}\}$ pair, as depicted in Table 3.1.

Steady State T-SSCV Oscillations During EFM

During EFM, a single pair of T-SSCV is affected with low-frequency oscillations, which is defined by the phase sequence of the input and output ports. From one side, if $\omega_1 \approx \omega_2$, the

affected pair will be

$$\tilde{\psi}_{C\varepsilon 3} = \frac{2}{3C}\frac{1}{\omega_1-\omega_2}P_{12}^{-}\sin([\omega_1-\omega_2]t+\phi_{12}^{-}) \quad (3.23)$$

$$\tilde{\psi}_{C\varepsilon 4} = \frac{2}{3C}\frac{-1}{\omega_1-\omega_2}P_{12}^{-}\cos([\omega_1-\omega_2]t+\phi_{12}^{-}) \quad (3.24)$$

on the other hand, if $\omega_1 \approx -\omega_2$, which can be considered as a electrical drive operating at a negative phase sequence, the following terms will suffer from high-amplitude oscillations

$$\tilde{\psi}_{C\varepsilon 1} = \frac{2}{3C}\frac{1}{\omega_1+\omega_2}P_{12}^{+}\sin\big([\omega_1+\omega_2]t+\phi_{12}^{+}\big)$$

$$\tilde{\psi}_{C\varepsilon 2} = \frac{2}{3C}\frac{1}{\omega_1+\omega_2}P_{12}^{+}\cos\big([\omega_1+\omega_2]t+\phi_{12}^{+}\big)$$

where the amplitudes P_{12}^{-} and P_{12}^{+} are defined in (3.22). An attractive EFM scenario is when the input/output voltages have equal amplitudes (V_1=V_2), where the power amplitudes are simplified to,

$$P_{12}^{+} = \frac{1}{2}|Q_1+Q_2|$$

$$P_{12}^{-} = \frac{1}{2}|Q_1-Q_2| \quad (3.25)$$

with Q_1 and Q_2 as the uvw and rts port reactive power, respectively. This definition concurs with the open-loop mitigation strategy presented in [26], which is based on a grid-side reactive power adjustment according to the load-side working power factor.

3.4. Chapter Summary

In this chapter, the M3C state-space modelling is presented. The approach uses two decoupled models for arm current and cluster capacitor voltages (CCV) dynamics. A linear transform is introduced, which separates the arm current dynamics into input port, output port and circulating currents; moreover, this linear transform facilitates the analysis of the CCV dynamics with the transformed arm currents and voltages. Four M3C circulating (inner) currents are obtained from the transformed model and stated as degrees of freedom. Specifically, these currents are used to regulate the CCVs. In addition to the circulating currents, the M3C common-mode voltage is also presented. The steady-state analysis defines the critical operating ranges of the M3C and highlights the issue involved when the M3C output port side frequency is near the input port side.

Chapter 4

Overview of Conventional Control Strategies for M3C

Due to the floating capacitors and the complex arm interconnections, the operation and control of the M3C is more complex than conventional converters. In addition to the proper input/output port current regulation, it is essential to keep the voltage of all capacitors within a feasible tolerance range. In this regard, several control strategies have been proposed in the literature, where the following general targets are sought [21, 22, 11]: to control the stored energy of the MMC, to regulate the arm currents and to locally balance the stored energy of each cell within an arm. It is worth mentioning that these targets are also utilised for the other MMC topologies, where the reasoning to define the control goals is the same.

In most of the reported works, the control of MMCs, including the M3C, are accomplished by using nested control loop approaches, as shown in Figure 4.1. Commonly, the stored energy control is sub-divided into the total stored energy regulation and the Cluster Capacitor Voltage (CCV) balancing/mitigation scheme. The mitigation control scheme is required during specific operation ranges of the system, and plays a key-role for electrical drive solutions based on the MMC [79, 21, 25]. The local balancing sub-goal balances the stored energy in each individual cluster through modifying the modulation scheme. [80]. By introducing linear transforms like that in (3.3), the MMC can be analysed as multiple decoupled circuits, where the input and output port dynamic relations are separated, and

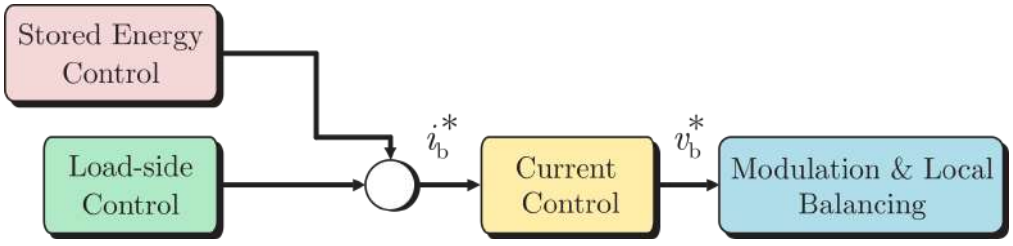

Figure 4.1: Typical Control Scheme for M3C and other MMCs.

the inner circulating currents are identified [in the case of the M3C there are four circulating currents, as shown in (3.4).

In this chapter, each control stage of the conventional control approach is described with its typical and traditional control scheme. As described in the following sections, most M3C variables are controlled with a SISO approach, where several control loops are used based on linear controllers.

4.1. Stored Energy Control

As initially specified, Stored Energy Control of the M3C is usually sub-divided into the 4.1.1 Total Stored Energy Control, 4.1.2 Balancing of the CCVs and 4.1.3 Mitigation of Low-frequency Oscillations.

4.1.1. Total Stored Energy Control

The target of this stage is to regulate the average value of all the capacitor voltages of the M3C, by tracking a given reference. The dynamic model of the average capacitor-voltage of the converter is obtained from a total stored energy model. For the M3C, the total stored energy w_{total}, is defined as,

$$w_{\text{total}} = \sum_{r=1}^{\text{N}_\text{T}} \frac{1}{2} \text{C}_r v_{\text{C}r}^2, \tag{4.1}$$

where N_T is the total number of cells of the MMC, and C_r and $v_{\text{C}r}$ are, respectively, the capacitance and the capacitor voltage corresponding to the r-th cell.

By using the principle of energy conservation, the following relation is stated:

$$\frac{\text{d}w_{\text{total}}}{\text{d}t} = p_{\text{in}} - p_{out} - p_{losses} \tag{4.2}$$

where p_{in} and p_{out} are, respectively, the input/output port power of the converter, and p_{losses} is the corresponding losses related to the converter.

For regulating the total stored energy, conventional Active Front-end (AFE) methodologies can be implemented if the input port is connected to a power grid [81, 1]; moreover, a vector current control scheme with a synchronous reference frame aligned with the input grid voltage can be used, which allows an active and, when applicable, reactive power regulation by d- and q-axis currents, respectively [82]. This is depicted in Figure 4.2, where the input port currents $\mathbf{i}_{\alpha\beta}$ are constructed from the total stored energy control scheme. The difference between variable $\Psi_{\text{C}0}$ and the given reference $\Psi_{\text{C}0}^{\text{ref}}$ are the inputs of a PI-controller that defines the d-axis input current reference in a Synchronous Reference Frame aligned with the input grid voltage. The phase-angle of the input grid is estimated using a Phase-locked Loop (PLL). Finally, the output signals are the input port current references in $\alpha\beta$ form.

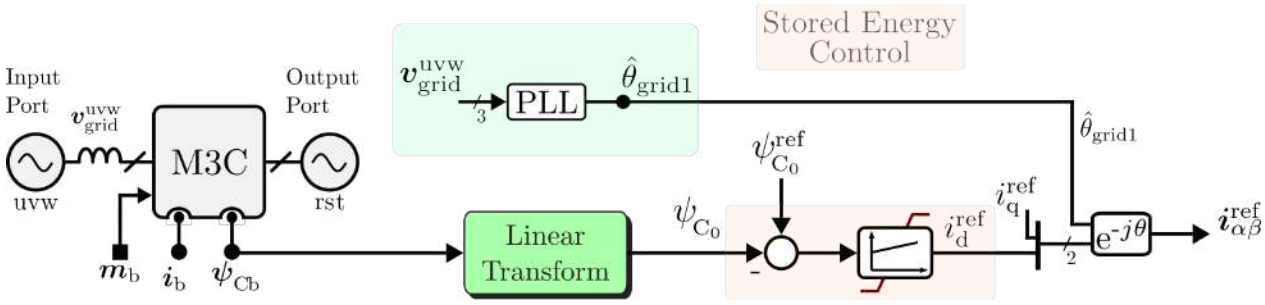

Figure 4.2: Traditional total stored energy control based on a PI-controller for M3C regulation.

4.1.2. CCV Balancing Scheme

Because the regulation of the total stored energy of the M3C does not specify any redistribution among the nine clusters, it is mandatory to include a scheme that assigns the stored energy among the CCVs or SSCVs[22, 24, 23]. To accomplish this, the main target of this strategy is to match the average voltage components of all the CCVs, where closed-loop control strategies are preferred and linear transforms are used for decoupling different cross terms in the system relationships. The control scheme is generally based on PI-controllers with transformed CCVs (T-CCVs) as inputs. The output signals of the PI-controllers are then used to construct the circulating current references, where the phase angles related to the input and output port voltages are required. Figure (4.3) illustrates a general control scheme for balancing the CCV terms of an M3C, where three sub-stages are clearly defined: Linear transform for the CCVs, PI-controllers, and circulating currents development ($\mathbf{i}^{\text{ref}}_{\text{circ}}$).

Due to the natural coupled relations among the four circulating currents (manipulated variables) with the nine SSCVs, the SSCVs balancing schemes have complex architectures that vary according to the linear transform used (like Double$-\alpha\beta\gamma$ or $\Sigma\Delta$ Double$-\alpha\beta\gamma$ transforms defined in [22, 24, 23]). Whether using the Double$-\alpha\beta\gamma$ or the $\Sigma\Delta$ Double$-\alpha\beta\gamma$ transform, the balance among clusters is achieved by adjusting the DC value of the defined T-SSCVs or T-CCVs. More specifically, and as shown in (3.8), the main target is accomplished when the eight T-SSCVs are regulated to a null average value, where, commonly, the high-frequency components are neglected because they are filtered out by the relatively large capacitance value. The output signals of the SSCV or CCV balancing scheme are

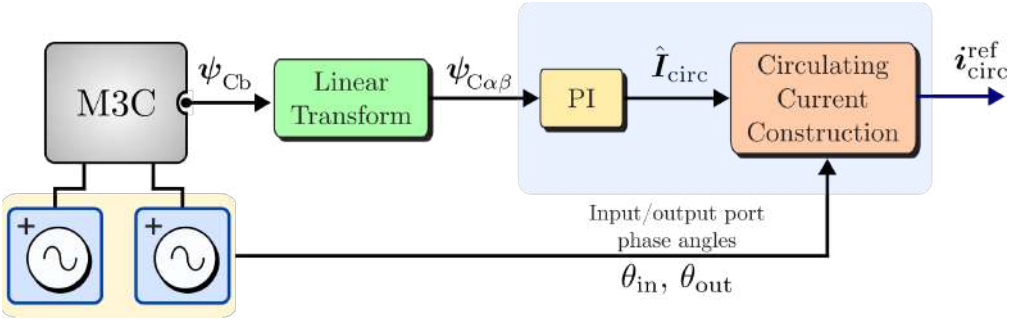

Figure 4.3: Traditional CCV balancing structure based on PI-controllers for MMC regulation.

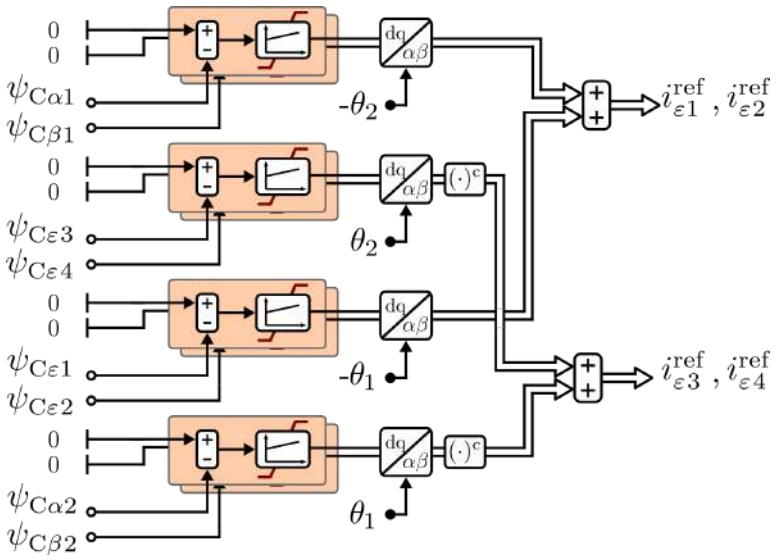

Figure 4.4: CCV balancing scheme based on the procedure and transform introduced by Diaz et al..

the circulating currents of the M3C, which are specified according to the linear transform implemented. The relationship among the circulating currents with the T-SSCVs is non-linear and dependant on the input and output port voltages [23].

In [24], a closed-loop control method with the Double$-\alpha\beta\gamma$ transform is reported, where the eight T-CCV terms are regulated using P-controllers. The output signals are then multiplied by sinusoidal functions with specific phase angles calculated from the input and output port frequencies. In order to improve the performance of this scheme, in [13, 23, 21] the T-CCVs measurements are filtered to mitigate the high-frequency components; moreover, the P-controllers are replaced for PI-controllers in comparison with the strategy proposed in [24]. In Figure 4.4, the balancing scheme described in [13] is illustrated, where eight PI-controllers are used. The reference signals are null for all the controllers, phase angles θ_1 and θ_2 are related to the input and output port voltages, respectively. Additionally, the operator $(\cdot)^c$ corresponds to the complex conjugate of the input.

4.1.3. Mitigation of Low-frequency Oscillations

Depending on the working frequency ranges related to the input and output ports, the M3C can operate within a critical frequency range, where large amplitude low-frequency oscillations are produced in the capacitor voltages.

The CCV balancing scheme is usually designed for Different Frequencies Mode (DFM) operation of the M3C, where no low-frequency voltage oscillations are expected in the floating capacitors. Therefore, when an extended range operation that includes near input frequency is required, additional considerations and methodologies have to be included.

By using the $\Sigma\Delta$ transformation, introduced in [22] and shown in (3.3), each critical range

is decoupled and identified with an specific pair of transformed CVVs. At present, the Equal Frequencies Mode (EFM) [$f_g \approx f_m$] has been the most studied critical range operation.

Regarding as to when a mitigation strategy could be required, or when the converter is in EFM, there is not a unified criteria. In practice, the CCV balancing scheme is utilised in a predefined condition, such as $|f_m \pm f_g| > \Delta f$, where Δf depends on the M3C rating, design parameters and tolerance band. Usually, $\Delta f \in$ [3-5]Hz, which is a value selected by heuristic criteria, as used in [21]. For example, in a electrical drive solution whose operation range includes EFM, the CCV balancing scheme is disabled when $|f_m \pm f_g| < \Delta f$, and a mitigation scheme is then enabled.

At present, the reported control strategies to achieve EFM operation are sub-divided into two categories: open-loop and closed-loop schemes.

Open-loop Schemes

The open-loop methodology was the first approach presented for controlling the M3C during EFM [24, 83]. Initially in [24], a complementary reactive power compensation in the grid-side is proposed for EFM. In other words, this approach implies that the low-frequency oscillations are mitigated by extra input port reactive injection. The reported results exhibit acceptable behaviour for limited operating conditions, where equal voltage magnitudes in both the input/output ports is the presented scenario.

In [83], a scheme based on common-mode voltage and circulating current injection for operation during EFM is proposed. The Double$-\alpha\beta\gamma$ is adopted, and the circulating currents are defined according to the specification of the common-mode voltage, the measured port currents and the port voltages. For desirable operation, it is recommended that the frequency of the common-mode voltage be one or two times higher than the input and output port working frequencies. This requirement aims to avoid unnecessary extra low-frequency components.

Closed-loop Schemes

The reported closed-loop control schemes are based on the measurement of the transformed CCVs (T-CCVs) to define further control signals [13, 36, 21].

In [21], a control for EFM operation is proposed using the $\Sigma\Delta$Double$-\alpha\beta\gamma$ representation of the M3C, where a broad operating range, including EFM, is experimentally validated. Figure 4.5 illustrates the implemented control scheme, where $v_{\mathrm{C1}\alpha}^{\Sigma\Delta}$ and $v_{\mathrm{C1}\beta}^{\Sigma\Delta}$ are the affected T-CCV terms with low-frequency oscillations, and θ_g with θ_m are the phase sequence of the voltage related to the input and output ports. The EFM control is achieved by defining a high frequency common-mode voltage and, afterwards, injecting circulating currents using a vector control scheme based on PI-controllers. In [36], the control of the M3C is achieved by using an optimisation approach, where natural frame modelling is used. The scheme defines an optimal common-mode voltage waveform and circulating current values according to the

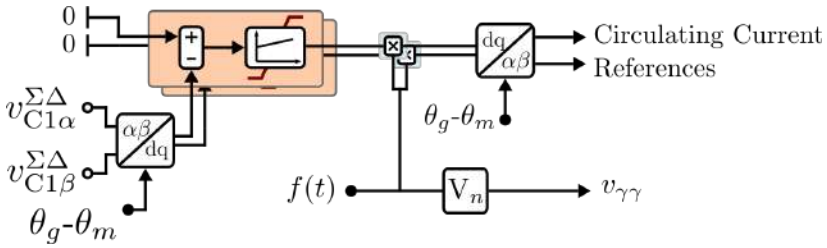

Figure 4.5: Mitigation control based on closed-loop scheme, proposed by Diaz et al..

proposed problem formulation.

4.2. Arm Current Regulation

As described in the modelling section, the use of a linear transform allows interpreting the arm current dynamics of the M3C as four separated input/output port circuits and four linear independent circulating circuits. In Figure 4.6, the methodology of the arm-current regulation for MMCs, including the M3C, is shown. With this approach, the regulation of the decoupled circuits can be achieved by conventional schemes, where the control of the port currents depend on the corresponding external system dynamics.

Since the input and output port can be decoupled entirely in the M3C, vector control is frequently used when the input port is a conventional balanced grid and when the load is passive, or an electrical machine [81]. Conversely, since the circulating current references are defined by the stored energy balancing scheme, where there are non-linear relationships, the resultant reference signals have at least two frequency components related to the frequencies of the input and output port [23, 21]. Moreover, the frequency components of the circulating current references could vary depending on the connected load or on the application (for instance, an electrical drive). Therefore, due to the reasons mentioned above, regulation of the circulating currents is usually realised using a SISO scheme based on four P-controllers (one per circulating current) [11, 25, 26, 21].

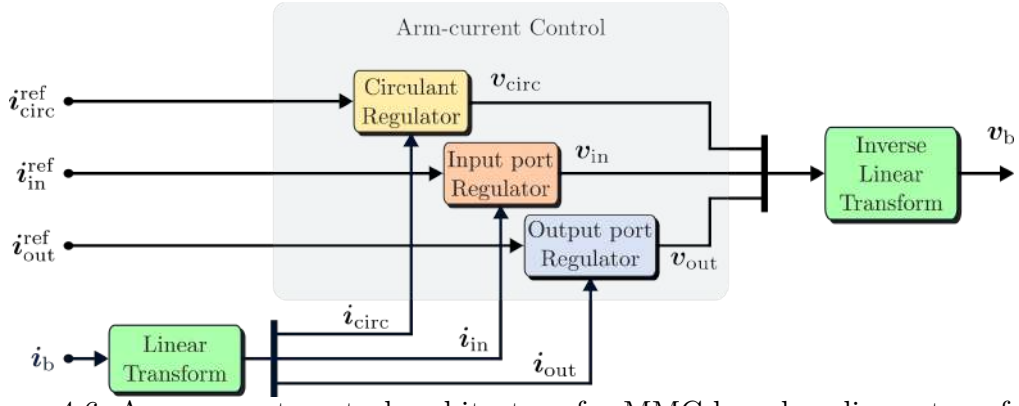

Figure 4.6: Arm-current control architecture for MMC based on linear transform.

4.3. Local Balancing Control

The local balancing scheme is closely linked to the modulation stage, and it is dependant on the instantaneous current polarity and the synthesised voltage of the respective branch. Most of the reported methods can be categorised into two main groups: local balancing with individual added signals and local balancing based on pulse-pattern reassignment [84, 85, 86]. The former group is mostly implemented with PS-PWM, where further signals are added to the original voltage references predefined by the arm current controllers. These signals are obtained from additional controllers for each module which requires proper tuning to avoid unstable overall operation [87]. The latter local balancing method is based on redistributing the original pulse pattern of a conventional modulation stage without affecting its overall pulse distribution [88, 89]. Redistribution of the pulse patterns is established from a priority list of the capacitor voltages and the output power sign; typically, these strategies are related with LS-PWM or NLM because they naturally induce uneven power distribution among the modules of each cluster[1, 90]. The uneven distribution is used to conveniently reassign the pulse patterns for regulating the capacitor voltages of each arm. Figure 4.7 illustrates both schemes.

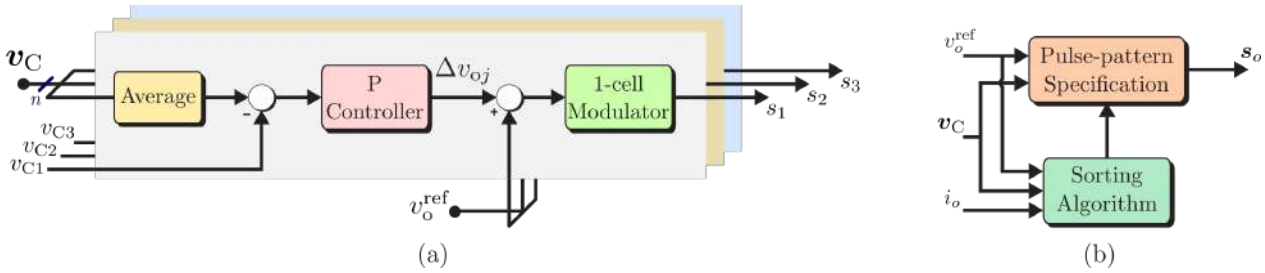

Figure 4.7: (a) Local Balancing scheme based on signal addition (3-cell arm) proposed by Kawamura et al.. (b) Local Balancing scheme based on sorting algorithm proposed by Kammerer et al..

4.4. Chapter Summary

In this chapter, the conventional three-stage control for regulating the M3C is introduced. The use of a linear transform is critical for this approach, where decoupled input, output and circulating current dynamics are obtained. This feature allows the use of separated current control schemes, where the circulating currents are commonly regulated by P-controllers The total stored energy control loop is usually based on a PI-controller, where the output is a current reference signal for the input port current control.

The CCV balancing scheme is obtained by controlling eight T-CCV variables to a zero average value. In the linear approach, eight PI controllers have been proposed, where their output signals are used with the input/output port voltage phase-angles to construct the circulating current references. This approach presents good results in DFM operation of the M3C.

If the M3C operates in EFM, a common-mode voltage is required. Usually, the frequency of this voltage is chosen to be sufficiently high to not interfere with other T-CCVs. A closed-loop vector control scheme for mitigating the low-frequency capacitor voltage oscillations have been proposed. In this scheme, a synchronous reference frame rotating at the difference between the input and the output port voltages is used.

In the available literature exists two main approaches to achieving local balancing control. One method uses LS-PWM or NLM with a priority list constructed from the capacitor voltage magnitudes. Depending on the charge status of the cluster, the list is arranged in an increasing or decreasing order. Conversely, the other proposed approach uses PS-PWM schemes with additional correcting signals into their modulation indexes. Both methods exhibit satisfactory results.

Chapter 5

Overview of Model Predictive Control Schemes for the M3C Control

As is well known, Model Predictive Control (MPC) schemes have been widely proposed for power electronics and drive solutions, where its inherent high-bandwidth response with straightforward integration of system non-linearities and operational constraints are the most attractive features [11, 29]. In the context of Power Electronics, most of the MPC schemes can be divided into two main groups: Finite-control-set MPC (FCS-MPC) and Continuous-control-set MPC (CCS-MPC) [30, 31, 32, 33, 34]. The former approach directly defines the switching status of all the semiconductors of the converter at every processing time; on the other hand, the CCS-MPC defines continuous output signals that have to be synthesised by a modulation stage.

Regarding MPC strategies applied to MMCs, most of the reported works are based on FCS-MPC approaches, where different converter models, and approximations, have been proposed [34]. Since the control of any MMC requires regulation of the floating capacitor voltages and arm currents, the related model is coupled and non-linear. Taking into consideration that the modelling is a fundamental aspect in any MPC methodology [30, 91], in the case of MMCs there are different approaches in order to implement a MPC scheme.

In this chapter, an overview of MPC schemes for M3C, and MMCs, is discussed. The purpose is to show what is the actual context of the published MPC strategies for M3C and MMC regulation. Initially, this chapter introduces the FCS-MPC and CCS-MPC schemes with their important features. Afterwards, the small number of MPC schemes for the M3C are presented.

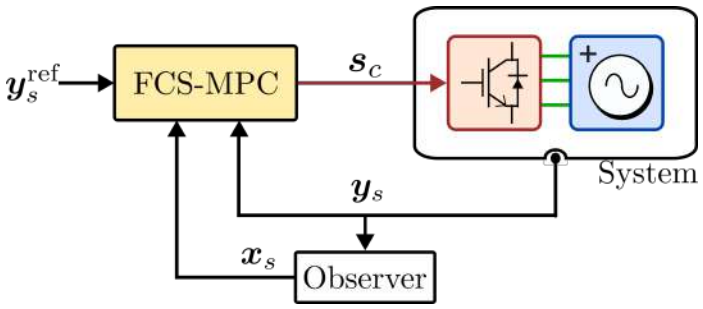

Figure 5.1: Finite-Control-Set MPC (FCS-MPC) regulation scheme. $\boldsymbol{s}_c$ represents the switching states of the converter, $\boldsymbol{y}_s$ is the measured variables, and $\boldsymbol{x}_s$ is the state variables of the system.

5.1. Finite Control Set MPC Schemes

As shown in Figure 5.1, the basic structure of this scheme is based on the regulation of the system by directly defining the switch states $\boldsymbol{s}_c$ at every sampling/processing time. Therefore, since there are a finite number of possible switching states of the converter, there exists a finite number of feasible predictions at every instant. At present, the most reported MPC scheme for power electronics solutions is the FCS-MPC with a prediction horizon equal to one, i.e N_f=1 [31, 30, 92].

For FCS-MPC schemes with N_f=1, the number of possible solutions is just defined by the number of different feasible switching states of the controlled converter. Additionally, the election of which solution is the best is strictly dependant of the definition of the cost function weights, where each $\boldsymbol{s}_i$ feasible switching state will define a related cost function value J_i. From these results, the required state is chosen according to the lowest cost, which is commonly identified by using an exhaustive search methodology. Taking into consideration that the switching states of a converter increase exponentially when the number of levels or switches increments, the related FCS-MPC burden naturally grows in *at least* the same proportion [93, 94, 31]. Therefore, in such cases the exhaustive search methodology should be somehow optimised.

On the other hand, FCS-MPC schemes with prediction horizon higher than one, have been reported with successful results [95, 31, 96, 97]. As has been stated in the literature, a greater horizon improves the performance of the MPC in several aspects, but, although seems an attractive option, the related computational burden and searching space of the scheme increases considerably. Therefore, the use of exhaustive search methods are no longer suitable and other alternatives have to be considered, where sphere-decoding based algorithms have been preferred [31, 98].

Another relevant drawback of FCS-MPC schemes is the widespread presence of extra harmonic content in the spectrum of the regulated variables. This fact is still present even when the selected sampling period of the FCS-MPC is high (∼20kHz), where the presence of low-order harmonic content can not be completely neglected [30].

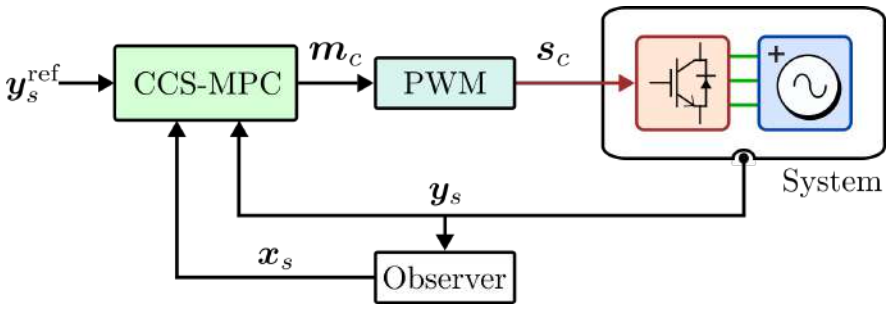

Figure 5.2: Continuous-Control-Set MPC (CCS-MPC) regulation scheme.$\boldsymbol{m}_c$ represents the modulation indexes, $\boldsymbol{s}_c$ is the switching state vector of the converter, $\boldsymbol{y}_s$ is the measured variables, and $\boldsymbol{x}_s$ is the state variables of the system.

In order to redistribute the widespread harmonic spectrum, Modulated FCS-MPC has been reported in the literature [99, 100, 101, 102]. This FCS-MPC scheme consists of the use of a second optimisation stage that ensures a fixed output switching frequency of the controlled device, keeping the inherent benefits of the FCS-MPC. However, there is an inherent increment of the computational burden due to the additional second optimisation stage; however, the sampling period can be increased due to the fixed switching frequency. Therefore, at some level or limit, this approach is attractive when the number of switches, or levels, yields a feasible computational burden. This limit can be enhanced if practical approximations are made (for instance, a reduction of the searching space).

5.2. CCS-MPC approach for Power Electronics Control

CCS-MPC schemes are based on an average model of the plant, where all the related variables (including the actuator signals) are continuous. Unlike FCS-MPC approaches, the discrete switching signal election is changed to the specification of the related output voltages or the corresponding modulation indexes [41, 91, 103, 104, 105, 106].

As depicted in Figure 5.2, the illustrated CCS-MPC scheme is based on the specification of continuous modulation index signals. These values can be either the output voltages of the respective converter arm/modules or the duty cycles of a space vector modulation scheme too.

After the output signals are defined from the CCS-MPC step, a modulation stage is required and traditional PWM or Space Vector approaches are usually preferred [32].

5.2.1. Resolution methods for CCS-MPC

Contrary to FCS-MPC approaches, the optimal solution of the CCS-MPC is obtained with a different methodology. Generally, the resolution of FCS-MPC problems are based on exhaustive search or sphere decoding methods; however, for CCS-MPC other concepts and strategies are required to calculate the optimal solution [107, 108, 109]. The mathematical formulation of the CCS-MPC approach is commonly known as an Inequality Constrained

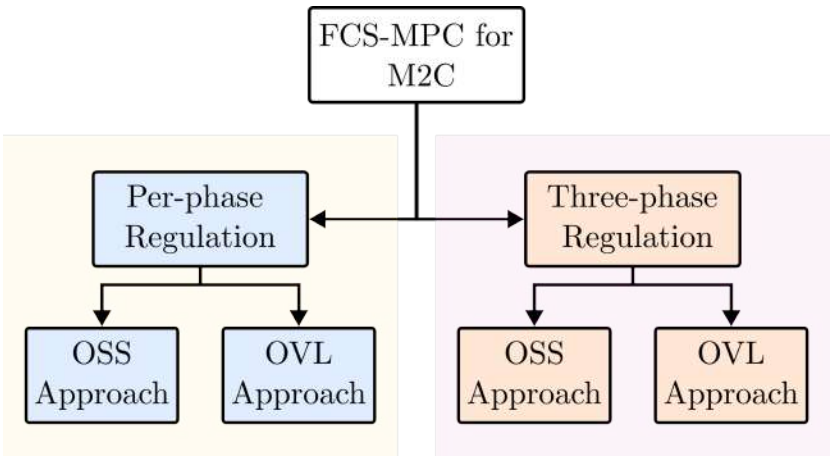

Figure 5.3: Proposed MPC strategy classification according to Dekka et al..

Quadratic Programming (IC-QP) problem, where there are several available solvers to obtain the required solution. Most of these methodologies can be classified into two main fields: (a) Active-set and (b) Interior-point methods [110, 111]. The Active-set methods are preferred when the size of the QP is relatively small; conversely, interior-point methods are frequently used when the dimension of the problem is considerably higher [109].

Other approaches, such as Explicit MPC are also an attractive alternative when the constraints and weights of the formulation are invariant, which allows an off-line computation of the QP problem [105, 106, 91]. Additionally, approaches based on analytical solution of a unconstrained QP problem formulation also have been reported [80, 84].

5.3. Control of MMCs based on Model Predictive Control

Regarding MPC strategies applied to MMCs, most of the reported works are based on FCS-MPC approaches, where different converter models, and approximations, have been proposed [34].

5.3.1. Control of the M2C by FCS-MPC

For M2C approaches based on FCS-MPC, the proposals can be categorised depending on the three-phase or per-phase model approach [34]. The former regulates the M2C by considering all of the six clusters with one control scheme, whereas the later regulates the converter by three separated controllers (one per output phase). When the number of power cells is considerable, the FCS-MPC approach is not feasible with its natural definition (even with a prediction horizon of one), since the available searching space dramatically increases [30]. For that reason, the majority of the reported works use variations of the conventional FCS-MPC for M2C, which implies simplifications of the searching space to yield a feasible computational burden.

FCS-MPC strategies for the M2C can be also classified into Optimal Switching State (OSS)

and Optimal Voltage Level (OVL) methods. The OSS directly defines the switching states of the converter and, therefore, it is the natural FCS-MPC derivation for M2C [34]; conversely, the OVL methodology defines voltage levels or vectors of the converter, and requires another stage to define the switching states. In comparison, there are several aspects that can define which approach, OSS or OVL, is more attractive [34]. Regarding computational burden, OVL approaches have lower complexity than OSS in general; however, OSS methods exhibit higher bandwidth. In terms of steady state performance, both schemes exhibit comparable performance with acceptable results [112].

5.4. Overview of MPC schemes used for M3C Regulation

The implementation of both FCS-MPC and CCS-MPC schemes for the M3C has received little attention in the literature. In this section, the schemes that have been proposed are described with their corresponding features and limitations.

5.4.1. FCS-MPC approach for the M3C

In [35], the M3C is regulated by a sub-converter methodology, where each of these sub-converter is regulated separately from the rest [see Figure 5.4]. The coupling among the sub-converters is achieved by using current reference signals. The load side port of the M3C is seen as a zero-sequence current injection from the sub-converter perspective. In order to reduce the computational burden, just one module per arm is free to modify its switching status at each processing period.

As the first approach of FCS-MPC for the M3C, it does not report experimental results nor operation during the critical frequency range. Additionally, the inner balancing scheme of each sub-converter induces undesirable current imbalances at the grid-side.

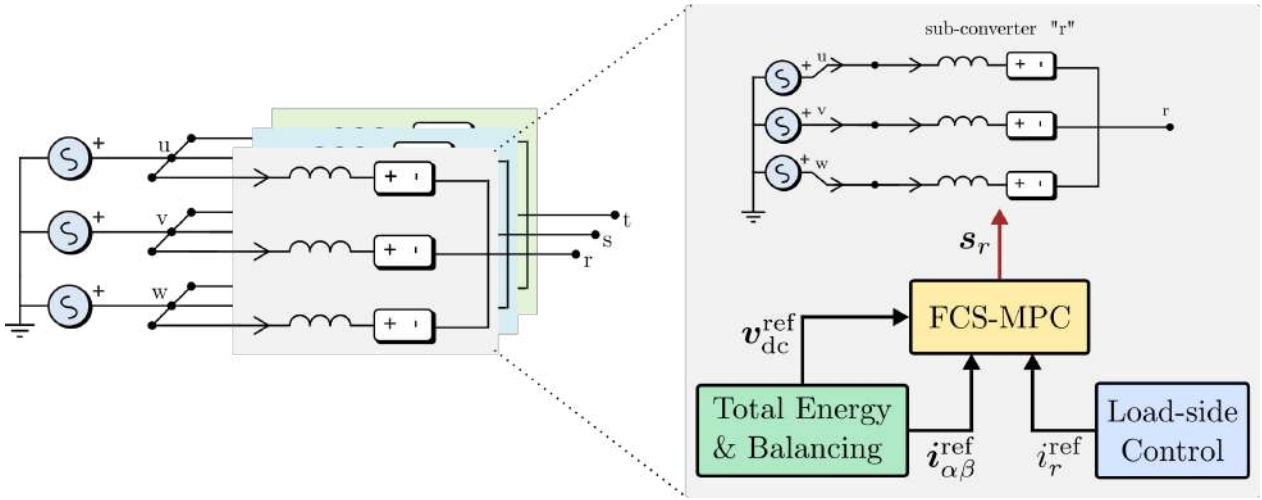

Figure 5.4: FCS-MPC scheme based on sub-converter independent regulation.

5.4.2. Three-stage optimisation approach

The reported work [36] proposes an optimisation approach for regulating the capacitor voltages of the M3C for Equal Frequencies Mode (EFM) and Different Frequencies Mode (DFM) [36]. Specifically, this strategy is based on a cascaded optimisation methodology [see Figure 5.5], where the output signal variables are the common-mode voltage and the circulating current reference signals. The first stage sets the common-mode voltage in accordance with the available CCVs in each cluster, which is computed from the input/output port voltages defined from the port current controllers. The second stage defines nine independent optimal current values that regulate the CCVs oscillations, which are calculated according to the capacitor voltage condition of each of the nine arms. Due to the requirement to not affect the port currents, additional correcting terms are added in a third stage to force a feasible current injection that does not affect the ports. Afterwards, the regulation of the circulating currents is achieved with traditional P-controllers.

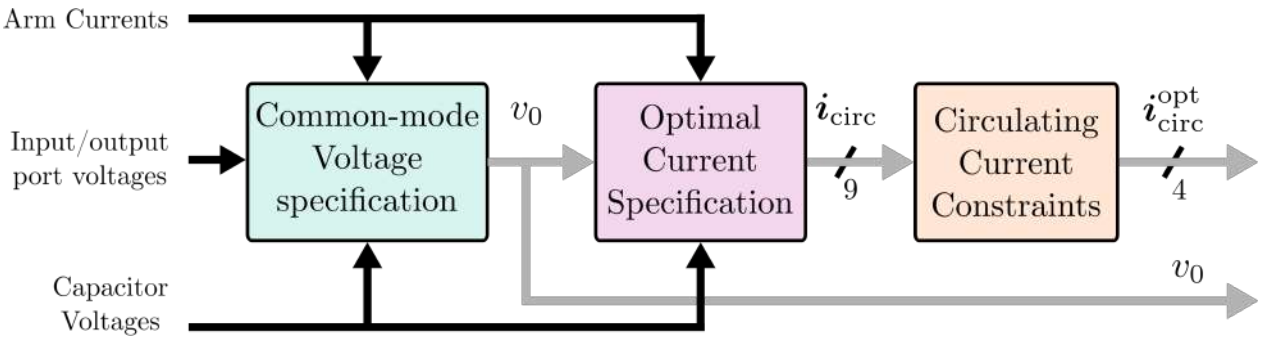

Figure 5.5: Three-stage optimisation scheme for full-frequency range operation proposed by Fan et al..

5.4.3. Generalised Approach for MMC Control with an Optimisation Stage

In [78], a generalised modelling and procedure for controlling the MMCs is proposed by using a steady state model. Particularly, this scheme uses an optimisation approach for regulating the stored energy of the converter, which requires the definition of customisable degrees of freedoms [see Figure 5.6]. In the article, the author defines circulating current frequency components as degrees of freedom, which aim to minimise the THD of the M3C arm currents. However, other specifications can be used as degrees of freedom.

Although the overall scheme is interesting in terms of the generalised view of the MMC control, validation of the scheme is only shown for DFM, where any critical frequency range is avoided. Additionally, non trivial extra adjustment of the computed stored energy is shown and the computation of the solution is based on steady frequency components in the circulating currents. Furthermore, the requirement of using linear independent degrees of freedom is not further discussed.

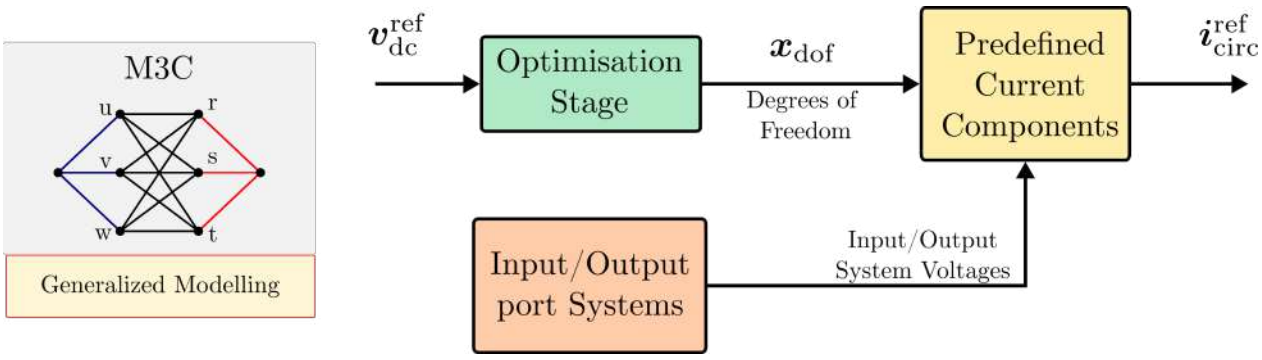

Figure 5.6: Stored Energy Control of the scheme proposed by Karwatzki et al..

5.5. Chapter Summary

In this chapter, an introduction of the main MPC approaches for power electronics, MMCs and the M3C have been shown. As indicated, most of the reported MPC works in the field of power electronics are based on Finite-control-set MPC (FCS-MPC) schemes, where the switching status of the converter are evaluated in the defined cost function. On the other hand, the Continuos-Control-Set MPC method defines continuous signals as outputs.

For the MMC family, most of the reported MPC works are focused on the M2C control with FCS-MPC. In these articles, the searching space is reduced to avoid the high computational burden related to the vast feasible switching status. Two different tendencies have been adopted to minimise searching space: OSS and OVL. In OSS, the optimal switching state is directly defined. Conversely, in OVL, the output voltages are specified from the optimisation problem; therefore, an additional stage is required to determine the switching states. At present, both approaches are actively being reported. Regarding the M3C, only one FCS-MPC approach has been reported with only simulation results. Unfortunately, the reported work shows important limitations, such as undesirable imbalanced current injection at the input port side and high switching restriction.

In contrast, a generalised optimal control approach for MMCs has been reported. This method is based on a steady-state power model of the MMC, and user-defined constraints are required. There is no straightforward procedure to adjust the behaviour or performance of the scheme, and no results are shown for EFM operation.

Finally, and closer to a CCS-MPC approach, a three-stage optimisation scheme have been reported to control the M3C. The common-mode voltage and the circulating current references are obtained for DFM and EFM operation. The first stage sets the common-mode voltage in accordance with the available CCVs in each cluster. The second stage defines optimal currents that regulate the CCV oscillations, defining nine independent current values based on the individual condition of each of the nine arms. To transform the solution obtained into a feasible current injection, the third stage includes equality constraints that determine the final four independent circulating currents. Although this method is interesting and useful,

division of the circulating current problem into two stages means that the resultant values can be a sub-optimal solution of the initial optimisation problem. Moreover, there is only one degree of freedom to adjust the performance of the scheme.

Chapter 6

Proposed Control Scheme for the M3C Based on CCS-MPC

To achieve a well-suited regulation of the M3C with wide-frequency range, the proposed scheme in this work is based on a cascaded MPC control strategy [see Figure 6.1]. The overall regulation is sub-divided into three stages [113, 22, 21]:(a) Stored Energy Control, (b) Arm Current Control and (c) Modulation and Local Balancing. Specifically, the scope of this work aims to regulate the Cluster Capacitor Voltages (CCVs) and the circulating currents of the M3C through a two-stage Continuous- Control-Set Model Predictive Control strategy (CCS-MPC), as depicted in Figure 6.1.

The first MPC stage is related to the balancing of the stored energy, where optimal circulating current references are the output signals, which are defined by an optimisation problem aiming to balance the CCVs, using their equivalent T-SSCVs as inputs. From the defined optimisation problem, an analytical solution is obtained, which defines the control law of this stage with a fixed computational burden. The second stage aims to regulate the circulating currents, where the output signals of this stage are the corresponding circulating voltages. In the formulation of this MPC problem, the maximum arm current and cluster capacitor voltages of the M3C are included as constraints, allowing a versatile arm current-voltage saturation scheme of the M3C. To obtain the optimal solutions when some constraints are active, an active-set algorithm is implemented.

The reasoning behind the two-stage MPC scheme is closely linked to feasible implementation even with a limited control platform hardware. As shown in the results section, the proposed scheme is suitable for implementation on a control platform based on a TMS320C6713 DSP board introduced in 2006 in the market, with promising results.

The structure of this chapter starts by defining the CCV Regulation Stage, where the optimisation problem formulation and the achievement of its corresponding analytical optimal solution are described. Afterwards, the Circulating Current MPC stage is explained, where

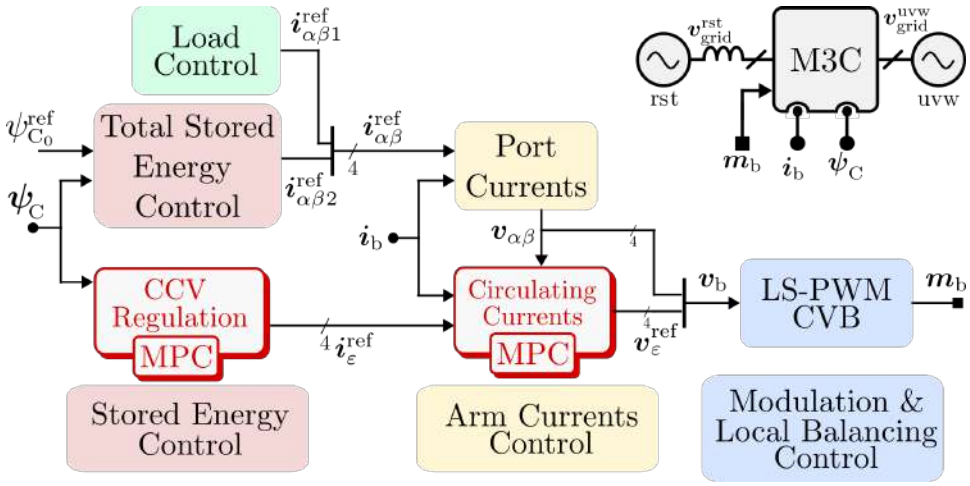

Figure 6.1: Proposed Control Scheme for the M3C based on a two-stage CCS-MPC.

the formulation of the optimisation problem and the definition of the constraints are stated; finally, the active-set algorithm to solve the second MPC stage is introduced.

6.1. CCV Balancing Scheme Based on CCS-MPC

In order to regulate the stored energy among the nine clusters, a CCS-MPC with finite horizon 1 is proposed [114, 91]. The inputs of this MPC scheme are the input/output port voltages defined by the corresponding port current controllers. Subsequently, the outputs of this MPC stage are the circulating current references that are used in the following MPC stage.

Specifically, this first MPC stage is an Equality Constrained Quadratic Programming problem (EC-QP) [107, 109], which has the following structure

$$\begin{aligned} &\underset{\boldsymbol{x}_{k+1},\ \boldsymbol{u}_k}{\text{Minimize}} && J = \hat{\boldsymbol{x}}_{k+1}^T \boldsymbol{Q} \hat{\boldsymbol{x}}_{k+1} + \hat{\boldsymbol{u}}_k^T \boldsymbol{R} \hat{\boldsymbol{u}}_k \\ &\text{subject to} && \hat{\boldsymbol{x}}_{k+1} = \boldsymbol{A}\hat{\boldsymbol{x}}_k + \boldsymbol{B}\hat{\boldsymbol{u}}_k + \hat{\mathbf{d}}_k \end{aligned} \tag{6.1}$$

where $\hat{\boldsymbol{x}}_{k+1}$ is the predicted error state, $\hat{\boldsymbol{u}}_k$ is the actuator signal, matrices $\boldsymbol{A}$ and $\boldsymbol{B}$ are established according to the plant of the controlled system, and $\mathbf{d}_k$ is a measurable disturbance. $\boldsymbol{R}$ and $\boldsymbol{Q}$ are the cost matrices of the actuator and the state respectively, where it is strongly required that the former be a symmetric positive-definite matrix and the latter be symmetric and positive semi-definite [114, 91]. As can be seen from the formulation, the equality constraint represents a dynamic behaviour of the state variables with the actuator and disturbance variables as inputs. Regardless of the type of constraints, a QP formulation of the cost function implies that there is a unique optimal solution, and several well-studied mechanisms and methodologies can be used for finding the optimal value [107, 109]. This feature will also be used to define the circulating current MPC control scheme.

It is worth mentioning that the formulation in (6.1) can be extended by including

inequality constraints, such as the maximum tolerable CCV or maximum circulating current. However, the inclusion of inequality constraints increases the computational burden of the control algorithm, which could lead to infeasible implementation for the control platform (TMS320C6713 DSP board) used. Despite this limitation, adequate tuning of the parameters $\boldsymbol{R}$ and $\boldsymbol{Q}$ allows a good overall M3C performance during steady and transient operation. Furthermore, the saturation scheme included in the second MPC stage reinforces the overall dynamic performance of the M3C.

The original formulation shown in (6.1) can be simplified by substituting the equality constraint into the cost function, resulting in the following formulation,

$$\underset{\hat{\boldsymbol{u}}_k}{\text{Minimize}} \quad J = \left(\hat{\boldsymbol{u}}_k - \hat{\boldsymbol{u}}_{unc,k}\right)^T \boldsymbol{H} \left(\hat{\boldsymbol{u}}_k - \hat{\boldsymbol{u}}_{unc,k}\right) \tag{6.2}$$

which is an equivalent formulation of (6.1) with exactly the same global solution $\hat{\boldsymbol{u}}_{unc,k}$, and where subscript *unc* refers to an *unconstrained solution* of the Quadratic Problem (QP), because no inequality constraint is included [31, 115]. The analytical value of $\hat{\boldsymbol{u}}_{unc}$ is defined as :

$$\begin{aligned} \hat{\boldsymbol{u}}_{unc,k} &= -\boldsymbol{H}^{-1}\boldsymbol{B}^T\boldsymbol{Q}(\boldsymbol{A}\hat{\boldsymbol{x}}_k + \hat{\mathbf{d}}_k) \\ \boldsymbol{H} &= \boldsymbol{B}^T\boldsymbol{Q}\boldsymbol{B} + \boldsymbol{R} \end{aligned} \tag{6.3}$$

Equation (6.3) gives, respectively, the optimal unconstrained solution of the optimisation problem and the resultant cost matrix. This simplified formulation has the same solution as the problem depicted in (6.1), for the argument $\hat{\boldsymbol{u}}_k$, which matches with the solution shown in the Annexed section.

Finally, computation of (6.3) is sufficient to define the optimal solution of (6.1).

6.1.1. Regulation of the Stored Energy Control Based on CCS-MPC

Based on the analysis in the previous sub-section, an optimal control strategy to regulate the SSCVs can be obtained. Firstly, to implement a CCS-MPC strategy for regulating the T-SSCVs, the following discretised form of (3.10) (obtained using the Forward Euler method) is introduced,

$$\boldsymbol{\psi}_{\mathrm{C}\alpha\beta\varepsilon,k+1} = \boldsymbol{\psi}_{\mathrm{C}\alpha\beta\varepsilon,k} + \boldsymbol{B}_{\mathrm{d},k}\mathbf{i}_{\varepsilon,k} + \mathbf{d}_{\mathrm{d},k}, \tag{6.4}$$

where $\boldsymbol{B}_{\mathrm{d},k}$=$\mathrm{T_s}\boldsymbol{B}_{\mathrm{C}}[k]$ is the sampled matrix $\boldsymbol{B}_{\mathrm{C}}(t)$ [see (3.11)] at the k-th instant, $\mathrm{T_s}$ is the sampling period, and $\mathbf{d}_{\mathrm{d},k}$=$\mathrm{T_s}\mathbf{d}_{\mathrm{C}}[k]$ is the sampled disturbance $\mathbf{d}_{\mathrm{C}}(t)$ [see (3.12)] at the k-th instant.

As shown in (6.1), the following required state and actuator signal errors are established,

$$\hat{\boldsymbol{x}}_k = \boldsymbol{\psi}_{\mathrm{C}\alpha\beta\varepsilon}^{\mathrm{ref_{MPC}}} - \boldsymbol{\psi}_{\mathrm{C}\alpha\beta\varepsilon,k} \tag{6.5}$$

$$\hat{\boldsymbol{u}}_k = \mathbf{i}_{\varepsilon}^{\mathrm{ref_{MPC}}} - \mathbf{i}_{\varepsilon,k}^{\mathrm{ref}} \tag{6.6}$$

where $\boldsymbol{\psi}_{\mathrm{C}\alpha\beta\varepsilon}^{\mathrm{ref_{MPC}}}$ and $\mathbf{i}_{\varepsilon}^{\mathrm{ref_{MPC}}}$ are, respectively, the reference signals from the MPC formulation, which are defined according to the required control goals [114, 91]. For the control scheme presented, $\boldsymbol{\psi}_{\mathrm{C}\alpha\beta\varepsilon}^{\mathrm{ref_{MPC}}}=\mathbf{0}_{8\mathrm{x}1}$ is imposed as the required first goal. In addition, it is desirable to achieve this ideal condition by utilising the smallest circulating current magnitudes. In this regard, $\mathbf{i}_{\varepsilon}^{\mathrm{ref_{MPC}}}=\mathbf{0}_{4\mathrm{x}1}$ is defined as the second control goal.

Using these goal definitions, the CCS-MPC scheme has the following structure,

$$\underset{\boldsymbol{\psi}_{\alpha\beta\varepsilon,k+1},\ \mathbf{i}_{\varepsilon,k}^{\mathrm{ref}}}{\text{Minimize}} \qquad J = \boldsymbol{\psi}_{\mathrm{C}\alpha\beta\varepsilon,k+1}^{T}\boldsymbol{Q}_{\mathrm{e}}\boldsymbol{\psi}_{\mathrm{C}\alpha\beta\varepsilon,k+1} + \mathbf{i}_{\varepsilon,k}^{\mathrm{ref}\,T}\boldsymbol{R}_{\mathrm{e}}\mathbf{i}_{\varepsilon,k}^{\mathrm{ref}} \tag{6.7}$$

$$\text{subject to} \qquad (6.4)$$

Using (6.2) and (6.3), the following optimal solution is obtained for (6.7),

$$\mathbf{i}_{\varepsilon,k}^{\mathrm{ref}} = \underbrace{\boldsymbol{H}_{\mathrm{e},k}^{-1}\boldsymbol{B}_{\mathrm{d},k}^{T}\boldsymbol{Q}_{\mathrm{e}}}_{\boldsymbol{K}_{\mathrm{e},k}}(-\boldsymbol{\psi}_{\mathrm{C}\alpha\beta\varepsilon,k} - \mathbf{d}_{\mathrm{d},k}) \tag{6.8}$$

where $\boldsymbol{H}_{\mathrm{e},k} = \boldsymbol{B}_{\mathrm{d},k}^{T}\boldsymbol{Q}_{\mathrm{e}}\boldsymbol{B}_{\mathrm{d},k} + \boldsymbol{R}_{\mathrm{e}}$ is the 4x4 resultant cost matrix, which changes at every k-th instant according to $\boldsymbol{B}_{\mathrm{d},k}$.

As shown in (6.8), the proposed control law can be interpreted as a closed loop scheme based on a P-controller with time variant 4x8 MIMO gain $\boldsymbol{K}_{\mathrm{e},k}$, as illustrated in Fig. 6.2. The MIMO gain $\boldsymbol{K}_{\mathrm{e},k}$ changes according to the input/output port voltages at every sampling period, and the specified cost weights of matrices $\boldsymbol{Q}_{\mathrm{e}}$ and $\boldsymbol{R}_{\mathrm{e}}$. Similarly, $\mathbf{d}_{\mathrm{d},k}$ can be seen as a feed forward term in the scheme that depends on the input/output port currents and voltages.

It should be noted that implementation of the proposed control is straightforward. No states have to be saved, unlike the conventional linear methods shown in [21, 116], and the same calculations are done at every sampling period, regardless of the number of cells. Additionally, as described below, each penalty cost constant is a degree of freedom directly linked with each T-SSCV and circulating current, which gives a clear insight into which term requires regulation depending on the operating mode of the M3C.

Definition of Cost Matrices

To accomplish suitable T-SSCVs regulation, it is fundamental to define cost weight values for the cost matrices $\boldsymbol{R}_{\mathrm{e}}$ and $\boldsymbol{Q}_{\mathrm{e}}$. If the M3C operating range considers EFM, just the tuning of matrix $\boldsymbol{Q}_{\mathrm{e}}$ is modified with a simple adjustment.

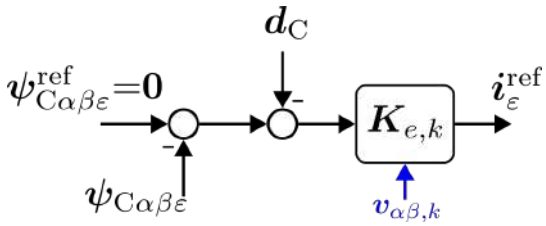

Figure 6.2: Block diagram scheme for the proposed control strategy based on CCS-MPC. For this application the MIMO gain $\boldsymbol{K}_{\mathrm{e},k}$ is a 4x8 time variant matrix.

According to the problem formulation (6.7), matrix $\boldsymbol{R}_{\mathrm{e}}$ is related to the cost weights of the circulating currents. Since there is not a particular priority among the circulating current magnitudes, all the costs are set identical:

$$\boldsymbol{R}_{\mathrm{e}} = r_{\mathrm{e}}\boldsymbol{I}_4 \tag{6.9}$$

This implies that each circulating current has the same cost error in (6.7) in the approach adopted.

In the case of the 8x8 matrix $\boldsymbol{Q}_{\mathrm{e}}$, the value of its coefficients are defined as:

$$\boldsymbol{Q}_{\mathrm{e}} = \boldsymbol{Diag}\ [q_0, q_0, q_0, q_0, q_{\varepsilon 12}, q_{\varepsilon 12}, q_{\varepsilon 34}, q_{\varepsilon 34}] \tag{6.10}$$

where the symbol $\boldsymbol{Diag}()$ denotes a diagonal matrix of size according to its inputs. As depicted in (6.10), the first four elements of the diagonal are equal to q_0, giving the same cost to the $\alpha\beta$ components of the vector $\boldsymbol{\psi}_{C\alpha\beta 0\varepsilon}$. Conversely, weights $q_{\varepsilon 12}$ and $q_{\varepsilon 34}$ are, respectively, related to the pairs $\psi_{C\varepsilon 1}$-$\psi_{C\varepsilon 2}$ and $\psi_{C\varepsilon 3}$-$\psi_{C\varepsilon 4}$, which are critically affected during EFM as described in Table 3.1.

Operation during DFM

Recalling section 3.3.1, in DFM operation, no undesirable low frequency power/CVV components are present. Therefore, in this operating range there is no specific priority among the T-SSCV for their regulation, and, hence, Q_{e}=$q_0\boldsymbol{I}_8$. Additionally, in this operating zone, the CMV is set to zero (v_0=0), since it is not necessary for regulating the CCVs.

For this operation zone, the gain $\boldsymbol{K}_{\mathrm{e},k}$ can be rewritten as,

$$\boldsymbol{K}_{\mathrm{e},k}=(\boldsymbol{B}^T_{\mathrm{d},k}\boldsymbol{B}_{\mathrm{d},k} + \frac{r_{\mathrm{e}}}{q_0}\boldsymbol{I}_4)^{-1}\boldsymbol{B}^T_{\mathrm{d},k} \tag{6.11}$$

where the ratio r_{e}/q_0 is chosen high enough to ensure $\det(\boldsymbol{K}_{\mathrm{e},k})\neq 0$ in any case. Additionally, because of the presence of the inverse operation and the matrix products involving the time-variant matrix $\boldsymbol{B}_{\mathrm{d},k}$, the coefficients of matrix $\boldsymbol{K}_{\mathrm{e},k}$ are also time dependant, with nonlinear relationships with respect to input/output port voltages..

From (6.11), it is important to remark that the ratio r_{e}/q_0 directly defines the system

bandwidth. Although the gain $\boldsymbol{K}_{\mathrm{e},k}$ is a time dependant parameter, the tuning of the cost weight ratio gives an insight of the system response. For instance, if r_{e}/q_0 is tuned to a lower value, the components of $\boldsymbol{K}_{\mathrm{e},k}$ will have higher values and, therefore, the bandwidth is increased. On the contrary, if r_{e}/q_0 is increased, the system dynamics will become slower.

Operation during EFM

Depending on the phase sequence at the output port, the low-frequency CCV oscillations related to EFM could appear either on pair $\psi_{\mathrm{C}\varepsilon 1}$-$\psi_{\mathrm{C}\varepsilon 2}$ or $\psi_{\mathrm{C}\varepsilon 3}$-$\psi_{\mathrm{C}\varepsilon 4}$. In this work, the uvw and rst ports are balanced with positive-sequence, and, therefore, only the pair $\psi_{\mathrm{C}\varepsilon 3}$ and $\psi_{\mathrm{C}\varepsilon 4}$ exhibit large low-frequency oscillations in the system studied [see (3.23)-(3.24)]. However, the scheme presented is not limited to this case and is equally applicable for either phase sequence.

During this operating condition, the parameter r_{e} remains fixed, $q_{\varepsilon 12} = q_0$, and $q_{\varepsilon 34}$ is increased. This new control goal implies that the CCS-MPC scheme regulates pair $\psi_{\mathrm{C}\varepsilon 3}$-$\psi_{\mathrm{C}\varepsilon 4}$ in priority to the others, because their cost is greater in the optimisation function. The suitability of this approach has been validated by the good experimental performance obtained with this selection.

Unlike DFM, during EFM it is fundamental to inject Common-mode Voltage (CMV) to ensure adequate regulation of the CCVs [21, 36]. The impact of CMV can be seen at the first two rows of (3.13), where complex power terms $\dot{\boldsymbol{p}}_{\varepsilon 12}$ or $\dot{\boldsymbol{p}}_{\varepsilon 34}$ are regulated by terms $v_0\dot{\mathbf{i}}_{\varepsilon 12}$ and $v_0\dot{\mathbf{i}}_{\varepsilon 34}$, respectively.

Regarding the circulating currents, notice that the shape, phase, frequency, etc. of them do not have to be predefined, because they are automatically obtained from (6.8). Additionally, if the cost weight of the corresponding affected pair is increased during EFM, the circulating currents will adopt the shape of the CMV waveform to mitigate the low-frequency oscillations. This feature can be seen in the results shown in section 7.1.2.

The specification of the CMV waveform can follow several methodologies, where a high frequency signal is preferred to avoid extra low-frequency components [21, 117]. For instance in [36], the authors propose a CMV waveform that depends on the remaining CCV voltage of the M3C. In [21], a square waveform is used, where the fundamental and the third harmonic are used for the circulating current construction. Due to limitations on the experimental control platform, like the implementation of a single-edge PWM scheme with an equivalent switching frequency of 1kHz, a sinusoidal waveform with twice the input port frequency is adopted. The amplitude of the CMV is specified off-line according to the available CCV voltage. Regarding the tuning of $q_{\varepsilon 34}$, it can be adjusted online. For instance, using simulation work the elements of $\boldsymbol{Q}_{\mathrm{e}}$, as a function of the M^3C operating point, can be obtained and stored in a look-up table for online adjustment [118]. However, online adjustment of $\boldsymbol{Q}_{\mathrm{e}}$ is considered outside the scope of this work.

6.2. Circulating Current Control Based on CCS-MPC

As depicted in Figure 6.1, the output signals of the MPC scheme for circulating current regulation are the circulating voltages. Nevertheless, the presented scheme also integrates an interesting saturation scheme, which is useful during transient operation.

The second stage MPC is discussed in three subsections. Firstly, in Section 6.2.1, the general MPC formulation is introduced. Secondly, in Section 6.2.2, the integration of the constraints in terms of the state and actuator variables is introduced. Finally, in Section 6.2.3, a procedure to solve the optimisation problem is described.

6.2.1. CCS-MPC formulation

As a starting point for the scheme, the dynamics of the circulating currents are discretised by using a ZOH method with sampling time T_s [119]:

$$\mathbf{i}_{\varepsilon,k+1} = \boldsymbol{A}_{\varepsilon}\mathbf{i}_{\varepsilon,k} + \boldsymbol{B}_{\varepsilon}\boldsymbol{v}_{\varepsilon,k} \tag{6.12}$$

where $\boldsymbol{A}_{\varepsilon}$=$\boldsymbol{I}_4$, $\boldsymbol{B}_{\varepsilon}$=-$\frac{T_s}{\mathrm{L_b}}\boldsymbol{I}_4$ and $\boldsymbol{I}_4$ is an 4x4 identity matrix. Notice that the dynamics of each circulating current are dependent on its corresponding circulating voltage $\boldsymbol{v}_{\varepsilon,k}$, and there are neither external disturbances nor coupled interactions with other circulating currents or voltages. With this definition, the proposed MPC strategy for regulating the circulating currents is:

$$\begin{aligned} \underset{\hat{\boldsymbol{x}}_{k+1},\hat{\boldsymbol{u}}_k}{\text{Minimize}} \quad & J = \hat{\boldsymbol{x}}_{k+1}^T \boldsymbol{Q}_{\text{circ}} \hat{\boldsymbol{x}}_{k+1} + \hat{\boldsymbol{u}}_k^T \boldsymbol{R}_{\text{circ}} \hat{\boldsymbol{u}}_k \\ \text{subject to} \quad & \hat{\boldsymbol{x}}_{k+1} = \boldsymbol{A}_{\varepsilon}\hat{\boldsymbol{x}}_k + \boldsymbol{B}_{\varepsilon}\hat{\boldsymbol{u}}_k \\ & \text{-}\boldsymbol{v}_{\text{dc},k} \leq \boldsymbol{v}_{\text{b},k} \leq \boldsymbol{v}_{\text{dc},k} \\ & \text{-}\boldsymbol{I}_{\max} \leq \mathbf{i}_{\text{b},k+1} \leq \boldsymbol{I}_{\max} \end{aligned} \tag{6.13}$$

with

$$\hat{\boldsymbol{x}}_k = \mathbf{i}_{\varepsilon}^{\text{ref}} - \mathbf{i}_{\varepsilon,k} \tag{6.14}$$

as the circulating current error vector, with reference $\mathbf{i}_{\varepsilon}^{\text{ref}}$ defined by the stored energy control [see previous Section 6.1], and

$$\hat{\boldsymbol{u}}_k = \boldsymbol{v}_{\varepsilon}^{\text{ref}} - \boldsymbol{v}_{\varepsilon,k} \tag{6.15}$$

as the circulating voltage error. Because the system of (6.12) is entirely decoupled, a dead-beat control law is used mainly for its simplicity[31, 115]:

$$\boldsymbol{v}_{\varepsilon}^{\text{ref}} = -\frac{\mathrm{L_b}}{T_s}\hat{\boldsymbol{x}}_k. \tag{6.16}$$

where the resultant control law is a proportional controller.

Because there is not any requirement nor preference to regulate the circulating currents, the regulation of all current errors are considered equally important, and the weight cost

matrices $\boldsymbol{R}_{\text{circ}}$ and $\boldsymbol{Q}_{\text{circ}}$ are specified as diagonal with equal coefficients:

$$\begin{aligned} \boldsymbol{R}_{\text{circ}} &= r_{\text{circ}}\boldsymbol{I}_4 \\ \boldsymbol{Q}_{\text{circ}} &= q_{\text{circ}}\boldsymbol{I}_4 \end{aligned} \tag{6.17}$$

where $q_{\text{circ}} \geq 0$ and $r_{\text{circ}} > 0$ are constants with positive values [91].

The inequality constraints are specified by the current limits and Cluster Capacitor Voltages (CCVs) of the nine clusters, where it is important to highlight that the measured CCVs are considered as constant values during the sampling period. As depicted in the first stage MPC description, constraints related to CCV limits are not considered due to practical limitations. However, they can be included in the first-stage MPC, which defines the circulating current references. As will be discussed in the result sections, despite not including the CCV constraints, the obtained transient behaviour of the M3C is adequate. Therefore, with the aforementioned considerations, the implemented inequality constraints in the second stage MPC are 36 bound limits.

By replacing the equality constraint of (6.13) in the cost function, the following optimisation problem is obtained (refer to the Annexed section [31, 115]):

$$\begin{aligned} \underset{\hat{\boldsymbol{u}}_k}{\text{Minimize}} \quad & J = \frac{1}{2}\hat{\boldsymbol{u}}_k^T h_{\text{circ}}\hat{\boldsymbol{u}}_k - \hat{\boldsymbol{u}}_{unc,k}^T h_{\text{circ}}\hat{\boldsymbol{u}}_k \\ \text{subject to} \quad & \text{-}\boldsymbol{v}_{\text{dc},k} \leq \boldsymbol{v}_{\text{b},k} \leq \boldsymbol{v}_{\text{dc},k} \\ & \text{-}\boldsymbol{I}_{\max} \leq \mathbf{i}_{\text{b},k+1} \leq \boldsymbol{I}_{\max} \end{aligned} \tag{6.18}$$

with $h_{\text{circ}}=2(\text{T}_s/\text{L}_b)^2 q_{\text{circ}} + 2r_{\text{circ}}$ as the resulting cost of the new optimisation problem, and $\hat{\boldsymbol{u}}_{unc,k}=\text{-}2(h_{\text{circ}}^{-1} q_{\text{circ}} r_{\text{circ}})\hat{\boldsymbol{x}}_k$ as the optimal solution of (6.18) without considering the inequality constraints. It is worth mentioning that the defined optimal solution $\hat{\boldsymbol{u}}_{unc,k}$ is exactly the same as the initial problem (6.13).

Since the argument of formulation (6.18) is $\hat{\boldsymbol{u}}_k$, it implies that the introduced inequality constraints related to arm currents and voltages must be rewritten in terms of $\hat{\boldsymbol{u}}_k$. This task facilitates the implementation of the Quadratic programming solver described in Section (6.2.3).

6.2.2. Constraint Specification of the Proposed MPC problem

In this section, the procedure to redefine the constraints in terms of $\hat{\boldsymbol{u}}_k$, is detailed. To accomplish this goal, the dynamic relation (6.12), the input/output port voltages defined by the output current controllers, and the linear transform defined in (3.3) are considered.

CCVs constraints

The inequality constraints related to the available CCVs can be rewritten in terms of the transformed voltages by using (3.3):

$$-\boldsymbol{v}_{\mathrm{dc},k} \leq \mathbf{T}^{-1}_{\alpha\beta0\varepsilon}\boldsymbol{v}_{\alpha\beta0\varepsilon,k} \leq \boldsymbol{v}_{\mathrm{dc},k} \tag{6.19}$$

where the vector $\boldsymbol{v}_{\alpha\beta0\varepsilon,k}$ can be decomposed into

$$\boldsymbol{v}_{\alpha\beta0\varepsilon,k}=\begin{bmatrix}\boldsymbol{v}_{\alpha\beta0,k}\\ \boldsymbol{v}_{\varepsilon,k}\end{bmatrix} \tag{6.20}$$

Taking into consideration the definition shown in (6.15), hereinafter the following decomposition is used for the transformed voltage vector:

$$\begin{aligned}\begin{bmatrix}\boldsymbol{v}_{\alpha\beta0,k}\\ \boldsymbol{v}_{\varepsilon,k}\end{bmatrix} &= \begin{bmatrix}\boldsymbol{v}_{\alpha\beta0,k}\\ \boldsymbol{v}^{\mathrm{ref}}_{\varepsilon}\text{-}\hat{\boldsymbol{u}}_k\end{bmatrix}\\ &= \begin{bmatrix}\boldsymbol{v}_{\alpha\beta0,k}\\ \boldsymbol{v}^{\mathrm{ref}}_{\varepsilon}\end{bmatrix} - \begin{bmatrix}\mathbf{0}_{5\mathrm{x}4}\\ \boldsymbol{I}_4\end{bmatrix}\hat{\boldsymbol{u}}_k\end{aligned} \tag{6.21}$$

where the first term of the right hand of the relation is already known from the input/output port current control scheme and the circulating current control law used in the MPC scheme, and $\mathbf{0}_{5\mathrm{x}4}$ is a 5x4 matrix composed of zeros. Substituting this decomposition into (6.19), yields the following 18 limits:

$$\underbrace{\begin{bmatrix}v^{\mathrm{ref}}_{\mathrm{b1},k}-v_{\mathrm{dc1},k}\\ v^{\mathrm{ref}}_{\mathrm{b2},k}-v_{\mathrm{dc2},k}\\ v^{\mathrm{ref}}_{\mathrm{b3},k}-v_{\mathrm{dc3},k}\\ v^{\mathrm{ref}}_{\mathrm{b4},k}-v_{\mathrm{dc4},k}\\ v^{\mathrm{ref}}_{\mathrm{b5},k}-v_{\mathrm{dc5},k}\\ v^{\mathrm{ref}}_{\mathrm{b6},k}-v_{\mathrm{dc6},k}\\ v^{\mathrm{ref}}_{\mathrm{b7},k}-v_{\mathrm{dc7},k}\\ v^{\mathrm{ref}}_{\mathrm{b8},k}-v_{\mathrm{dc8},k}\\ v^{\mathrm{ref}}_{\mathrm{b9},k}-v_{\mathrm{dc9},k}\end{bmatrix}}_{\mathbf{L}_{v_{\mathrm{dc}}}} \leq \frac{1}{3}\underbrace{\begin{bmatrix}2 & 0 & 2 & 0\\ -1 & -\sqrt{3} & -1 & -\sqrt{3}\\ -1 & \sqrt{3} & -1 & \sqrt{3}\\ -1 & -\sqrt{3} & -1 & \sqrt{3}\\ -1 & \sqrt{3} & 2 & 0\\ 2 & 0 & -1 & -\sqrt{3}\\ -1 & \sqrt{3} & -1 & -\sqrt{3}\\ 2 & 0 & -1 & \sqrt{3}\\ -1 & -\sqrt{3} & 2 & 0\end{bmatrix}}_{\mathbf{C}_u}\hat{\boldsymbol{u}}_k \leq \underbrace{\begin{bmatrix}v^{\mathrm{ref}}_{\mathrm{b1},k}+v_{\mathrm{dc1},k}\\ v^{\mathrm{ref}}_{\mathrm{b2},k}+v_{\mathrm{dc2},k}\\ v^{\mathrm{ref}}_{\mathrm{b3},k}+v_{\mathrm{dc3},k}\\ v^{\mathrm{ref}}_{\mathrm{b4},k}+v_{\mathrm{dc4},k}\\ v^{\mathrm{ref}}_{\mathrm{b5},k}+v_{\mathrm{dc5},k}\\ v^{\mathrm{ref}}_{\mathrm{b6},k}+v_{\mathrm{dc6},k}\\ v^{\mathrm{ref}}_{\mathrm{b7},k}+v_{\mathrm{dc7},k}\\ v^{\mathrm{ref}}_{\mathrm{b8},k}+v_{\mathrm{dc8},k}\\ v^{\mathrm{ref}}_{\mathrm{b9},k}+v_{\mathrm{dc9},k}\end{bmatrix}}_{\mathbf{U}_{v_{\mathrm{dc}}}} \tag{6.22}$$

with $\mathbf{L}_{v_{\mathrm{dc}}}=-\boldsymbol{v}_{\mathrm{dc},k}+\boldsymbol{v}^{\mathrm{ref}}_{\mathrm{b},k}$ and $\mathbf{U}_{v_{\mathrm{dc}}}=\boldsymbol{v}_{\mathrm{dc},k}+\boldsymbol{v}^{\mathrm{ref}}_{\mathrm{b},k}$ as inferior and upper limits in vector form, and $\boldsymbol{v}^{\mathrm{ref}}_{\mathrm{b},k}=\mathbf{T}^{-1}_{\alpha\beta0\varepsilon}\begin{bmatrix}\boldsymbol{v}_{\alpha\beta0,k}\\ \boldsymbol{v}^{\mathrm{ref}}_{\varepsilon}\end{bmatrix}$ as the output voltage reference considering (6.16).

The resultant inequality constraint depends on the value of the measured currents and, therefore, it changes at every sampling period.

Current Limit Constraints

Similarly, the arm current limits can be stated by the transformed current terms:

$$-\boldsymbol{I}_{\max} \leq \mathbf{T}^{-1}_{\alpha\beta0\varepsilon}\mathbf{i}_{\alpha\beta0\varepsilon,k+1} \leq \boldsymbol{I}_{\max} \tag{6.23}$$

where $\mathbf{i}_{\alpha\beta0\varepsilon,k+1}=\begin{bmatrix}\mathbf{i}_{\alpha\beta0,k+1}\\ \mathbf{i}_{\varepsilon,k+1}\end{bmatrix}$. Moreover, taking into account (6.12) and (6.15) yields:

$$\begin{aligned}\begin{bmatrix}\mathbf{i}_{\alpha\beta0,k+1}\\ \mathbf{i}_{\varepsilon,k+1}\end{bmatrix} &= \begin{bmatrix}\mathbf{i}_{\alpha\beta0,k+1}\\ \mathbf{i}_{\varepsilon,k}\end{bmatrix}+\begin{bmatrix}\mathbf{0}_{5\text{x}1}\\ -\frac{T_s}{\mathrm{L_b}}(\boldsymbol{v}^{\mathrm{ref}}_{\varepsilon}-\hat{\boldsymbol{u}}_k)\end{bmatrix}\\ &= \begin{bmatrix}\mathbf{i}_{\alpha\beta0,k+1}\\ \mathbf{i}_{\varepsilon,k}\end{bmatrix}-\frac{T_s}{\mathrm{L_b}}\begin{bmatrix}\mathbf{0}_{5\text{x}1}\\ \boldsymbol{v}^{\mathrm{ref}}_{\varepsilon}\end{bmatrix}+\frac{T_s}{\mathrm{L_b}}\begin{bmatrix}\mathbf{0}_{5\text{x}4}\\ \boldsymbol{I}_4\end{bmatrix}\hat{\boldsymbol{u}}_k\end{aligned} \tag{6.24}$$

If the models of input/output ports are not clearly defined it could be stated that $\mathbf{i}_{\alpha\beta0,k+1}\approx\mathbf{i}_{\alpha\beta0,k}$, which can be a good approximation when the sampling frequency is reasonably high, and the sampling time is relatively small when compared to the time constants associated with the load dynamics. We refer to this as the "**MPC Strategy with Saturation Scheme A**". If the models of input/output ports are known, the computation of an estimation for $\mathbf{i}_{\alpha\beta0,k+1}$ can be calculated online and it helps to obtain a better definition of the bounds for each sampling period. We refer to this as the "**MPC Strategy with Saturation Scheme B**".

Regardless of which saturation scheme is used, if an estimation of the output currents is known at instant "k+1", it can be used in (6.23) to define the following 18 additional bounds:

$$\underbrace{\begin{bmatrix}-\frac{\mathrm{L_b}}{T_s}(I_{\max}+\mathrm{i}_{\mathrm{b}1,k})+\Delta v_{\mathrm{b}1\varepsilon}\\ -\frac{\mathrm{L_b}}{T_s}(I_{\max}+\mathrm{i}_{\mathrm{b}2,k})+\Delta v_{\mathrm{b}2\varepsilon}\\ -\frac{\mathrm{L_b}}{T_s}(I_{\max}+\mathrm{i}_{\mathrm{b}3,k})+\Delta v_{\mathrm{b}3\varepsilon}\\ -\frac{\mathrm{L_b}}{T_s}(I_{\max}+\mathrm{i}_{\mathrm{b}4,k})+\Delta v_{\mathrm{b}4\varepsilon}\\ -\frac{\mathrm{L_b}}{T_s}(I_{\max}+\mathrm{i}_{\mathrm{b}5,k})+\Delta v_{\mathrm{b}5\varepsilon}\\ -\frac{\mathrm{L_b}}{T_s}(I_{\max}+\mathrm{i}_{\mathrm{b}6,k})+\Delta v_{\mathrm{b}6\varepsilon}\\ -\frac{\mathrm{L_b}}{T_s}(I_{\max}+\mathrm{i}_{\mathrm{b}7,k})+\Delta v_{\mathrm{b}7\varepsilon}\\ -\frac{\mathrm{L_b}}{T_s}(I_{\max}+\mathrm{i}_{\mathrm{b}8,k})+\Delta v_{\mathrm{b}8\varepsilon}\\ -\frac{\mathrm{L_b}}{T_s}(I_{\max}+\mathrm{i}_{\mathrm{b}9,k})+\Delta v_{\mathrm{b}9\varepsilon}\end{bmatrix}}_{\mathbf{L}_{I_{\max}}} \leq \mathbf{C}_u\hat{\boldsymbol{u}}_k \leq \underbrace{\begin{bmatrix}\frac{\mathrm{L_b}}{T_s}(I_{\max}-\mathrm{i}_{\mathrm{b}1,k})+\Delta v_{\mathrm{b}1\varepsilon}\\ \frac{\mathrm{L_b}}{T_s}(I_{\max}-\mathrm{i}_{\mathrm{b}2,k})+\Delta v_{\mathrm{b}2\varepsilon}\\ \frac{\mathrm{L_b}}{T_s}(I_{\max}-\mathrm{i}_{\mathrm{b}3,k})+\Delta v_{\mathrm{b}3\varepsilon}\\ \frac{\mathrm{L_b}}{T_s}(I_{\max}-\mathrm{i}_{\mathrm{b}4,k})+\Delta v_{\mathrm{b}4\varepsilon}\\ \frac{\mathrm{L_b}}{T_s}(I_{\max}-\mathrm{i}_{\mathrm{b}5,k})+\Delta v_{\mathrm{b}5\varepsilon}\\ \frac{\mathrm{L_b}}{T_s}(I_{\max}-\mathrm{i}_{\mathrm{b}6,k})+\Delta v_{\mathrm{b}6\varepsilon}\\ \frac{\mathrm{L_b}}{T_s}(I_{\max}-\mathrm{i}_{\mathrm{b}7,k})+\Delta v_{\mathrm{b}7\varepsilon}\\ \frac{\mathrm{L_b}}{T_s}(I_{\max}-\mathrm{i}_{\mathrm{b}8,k})+\Delta v_{\mathrm{b}8\varepsilon}\\ \frac{\mathrm{L_b}}{T_s}(I_{\max}-\mathrm{i}_{\mathrm{b}9,k})+\Delta v_{\mathrm{b}9\varepsilon}\end{bmatrix}}_{\mathbf{U}_{I_{\max}}} \tag{6.25}$$

where $\mathbf{L}_{I_{\max}}=-\frac{\mathrm{L_b}}{T_s}(\boldsymbol{I}_{\max}+\mathbf{i}_{\mathrm{b},k})+\Delta\boldsymbol{v}_{\mathrm{b}\varepsilon}$ is the lower bound, and $\mathbf{U}_{I_{\max}}=\frac{\mathrm{L_b}}{T_s}(\boldsymbol{I}_{\max}-\mathbf{i}_{\mathrm{b},k})+\Delta\boldsymbol{v}_{\mathrm{b}\varepsilon}$ is the upper bound in vector form, with $\Delta\boldsymbol{v}_{\mathrm{b}\varepsilon}=\mathbf{T}^{-1}_{\alpha\beta0\varepsilon}\begin{bmatrix}\mathbf{0}_{5\text{x}1}\\ \boldsymbol{v}^{\mathrm{ref}}_{\varepsilon}\end{bmatrix}$.

Incorporation of the Constraints into the Cost Function

The resultant constraints defined in (6.22) and (6.25), expressed in terms of the argument $\hat{\boldsymbol{u}}_k$, are computed at every sampling period and are suitable for implementation in the

Active-set algorithm. However, there are several redundancies in the obtained bounds, which can be simplified to achieve a more efficient final algorithm. Specifically, it can be seen that each row of vector $\mathrm{C}_{u,j}\hat{\boldsymbol{u}}_k$ has two upper and two lower limits, which, respectively, are defined by the arm current and the CCV limits. Therefore, in the following procedure, it is shown how the original 36 bounds can be reduced to 18, by using straightforward simplifications and maintaining the same benefits as the original formulation.

For the j-th cluster, the following lower bounds are defined,

$$\begin{bmatrix} \mathrm{L}_{I_{\max,j}} \\ \mathrm{L}_{v_{\mathrm{dc},j}} \end{bmatrix} \leq \mathrm{C}_{u,j}\hat{\boldsymbol{u}}_k \tag{6.26}$$

where $\mathrm{L}_{I_{\max,j}}$ and $\mathrm{L}_{v_{\mathrm{dc},j}}$ are the j-th element of vectors $\mathbf{L}_{I_{\max}}$ and $\mathbf{L}_{v_{\mathrm{dc}}}$, respectively. Additionally, $\mathrm{C}_{u,j}$ is the j-th row of matrix $\mathbf{C}_u$, which is defined in (6.22).

As depicted in (6.26), if the constraint related to the maximum between $\mathrm{L}_{I_{\max,j}}$ and $\mathrm{L}_{v_{\mathrm{dc},j}}$ value is met, the other constraint is automatically met too. Therefore, (6.26) can be replaced by just one constraint as,

$$\mathrm{Max}\left\{\mathrm{L}_{v_{\mathrm{dc},j}}; \mathrm{L}_{I_{\max,j}}\right\} \leq \mathrm{C}_{u,j}\hat{\boldsymbol{u}}_k \tag{6.27}$$

With a similar procedure, the upper bounds for the same j-th cluster can be stated as,

$$\begin{bmatrix} -\mathrm{U}_{I_{\max,j}} \\ -\mathrm{U}_{v_{\mathrm{dc},j}} \end{bmatrix} \leq (-\mathrm{C}_{u,j})\hat{\boldsymbol{u}}_k. \tag{6.28}$$

where $\mathrm{U}_{I_{\max,j}}$ and $\mathrm{U}_{v_{\mathrm{dc},j}}$ are the j-th element of vectors $\mathbf{U}_{I_{\max}}$ and $\mathbf{U}_{v_{\mathrm{dc}}}$, respectively. Using the same analysis performed for the lower bounds, the two upper bounds can be replaced by the following constraint:

$$-\mathrm{Min}\left\{\mathrm{L}_{v_{\mathrm{dc},j}}; \mathrm{U}_{I_{\max,j}}\right\} \leq (-\mathrm{C}_{u,j})\hat{\boldsymbol{u}}_k \tag{6.29}$$

With the aforementioned considerations, the inequality constraints of (6.18) rewritten in terms of $\hat{\boldsymbol{u}}_k$ are incorporated as follows:

$$\underbrace{\begin{bmatrix} \mathrm{L}_u \\ -\mathrm{U}_u \end{bmatrix}}_{\boldsymbol{M}_u} \leq \underbrace{\begin{bmatrix} \mathbf{C}_u \\ -\mathbf{C}_u \end{bmatrix}}_{\boldsymbol{K}_u} \hat{\boldsymbol{u}}_k \tag{6.30}$$

where

$$\begin{aligned} \mathrm{L}_u &= \mathrm{Max}\left\{\mathrm{L}_{v_{\mathrm{dc}}}; \mathrm{L}_{I_{\max}}\right\} \\ \mathrm{U}_u &= \mathrm{Min}\left\{\mathrm{U}_{v_{\mathrm{dc}}}; \mathrm{U}_{I_{\max}}\right\} \end{aligned} \tag{6.31}$$

are the constraints utilised for the proposed MPC strategy. The operators "Max{}" and

"Min{}" compute the maximum and minimum values for each element of the respective input vectors. The outputs of these operators have the same size as the inputs. Therefore, the 36 constraints of the space defined from (6.22) and (6.25), are significantly reduced to 18 as shown in (6.31). These 18 constraints define the size of the matrices $\boldsymbol{M}_u$ and $\boldsymbol{K}_u$ as 18x1 and 18x4, respectively.

6.2.3. Implementation of the Strategy

To solve the optimisation problem stated in (6.18), an Active-set algorithm is used with the methodology discussed in [109].

The Active-set method states that the solution of the main Quadratic Programming (QP) problem of (6.18) is equivalent to the solution of the following Equality Constrained QP (EC-QP),

$$\begin{aligned} \underset{\hat{\boldsymbol{u}}_k}{\text{Minimize}} \quad & \frac{1}{2}\hat{\boldsymbol{u}}_k^T h_{\text{circ}}\hat{\boldsymbol{u}}_k\text{-}\hat{\boldsymbol{u}}_{unc,k}^T h_{\text{circ}}\hat{\boldsymbol{u}}_k \\ \text{subject to} \quad & \boldsymbol{K}_u^*\hat{\boldsymbol{u}}_k{=}\boldsymbol{M}_u^* \\ & (\boldsymbol{K}_u^*, \boldsymbol{M}_u^*) \in \boldsymbol{\mathcal{W}}^*, \end{aligned} \tag{6.32}$$

where $\boldsymbol{\mathcal{W}}^*$ is the set of active constraints defined from (6.30), with $\boldsymbol{K}_u^*$ and $\boldsymbol{M}_u^*$ as the matrices composed of the active row-vectors and elements from $\boldsymbol{K}_u$ and $\boldsymbol{M}_u$, respectively. Because the set $\boldsymbol{\mathcal{W}}^*$ is not known initially, an iterative procedure for finding $\boldsymbol{\mathcal{W}}^*$ and solving (6.32) is implemented. For every iteration, a rearranged EC-QP obtained from (6.32) is solved, which has the following structure for the j-th step,

$$\begin{aligned} \underset{\boldsymbol{p}_{k,j}}{\text{Minimize}} \quad & \frac{1}{2}\boldsymbol{p}_{k,j}^T h_{\text{circ}}\boldsymbol{p}_{k,j} + \boldsymbol{g}_{k,j}^T\boldsymbol{p}_{k,j} \\ \text{subject to} \quad & \boldsymbol{K}_{u,j}\boldsymbol{p}_{k,j} = \boldsymbol{0} \end{aligned} \tag{6.33}$$

where $\boldsymbol{p}_{k,j}$ is the argument, $\boldsymbol{g}_{k,j}$=-$h_{\text{circ}}(\hat{\boldsymbol{u}}_{k,j\text{-in}}{+}\hat{\boldsymbol{u}}_{unc,k})$ is a vector defined at every iteration according to the input $\hat{\boldsymbol{u}}_{k,j\text{-in}}$, and $\boldsymbol{K}_{u,j}$ is assembled from the selected row-vectors defined in $\boldsymbol{\mathcal{W}}_j$ according to the active constraints in the j-th iteration.

The solution of (6.33) is obtained using:

$$\begin{bmatrix} h_{\text{circ}}\boldsymbol{I}_4 & \boldsymbol{K}_{u,j}^T \\ \boldsymbol{K}_{u,j} & \boldsymbol{0} \end{bmatrix} \begin{bmatrix} -\boldsymbol{p}_{k,j}^* \\ \boldsymbol{\lambda}_{k,j}^* \end{bmatrix} = \begin{bmatrix} \boldsymbol{g}_{k,j} \\ \boldsymbol{0} \end{bmatrix} \tag{6.34}$$

where $\boldsymbol{p}_{k,j}^*$ is the optimal solution, and $\boldsymbol{\lambda}_{k,j}^*$ is the vector of Lagrange multipliers that has a length equal to the number of active constraints [109].

If $\boldsymbol{p}_{k,j}^* = \boldsymbol{0}$, it means that $\hat{\boldsymbol{u}}_{k,j\text{-in}}$ is the optimal value that minimizes (6.33). Moreover, if all the elements of $\boldsymbol{\lambda}_{k,j}^*$ are zero or positive, it implies that $\hat{\boldsymbol{u}}_{k,j\text{-in}}$ is the global optimal solution that satisfies (6.18) , and $\boldsymbol{\mathcal{W}}_j{=}\boldsymbol{\mathcal{W}}^*$.

If $\boldsymbol{p}_{k,j}^* = \boldsymbol{0}$ and at least one element of $\boldsymbol{\lambda}_{k,j}^*$ is negative, it implies that the computed

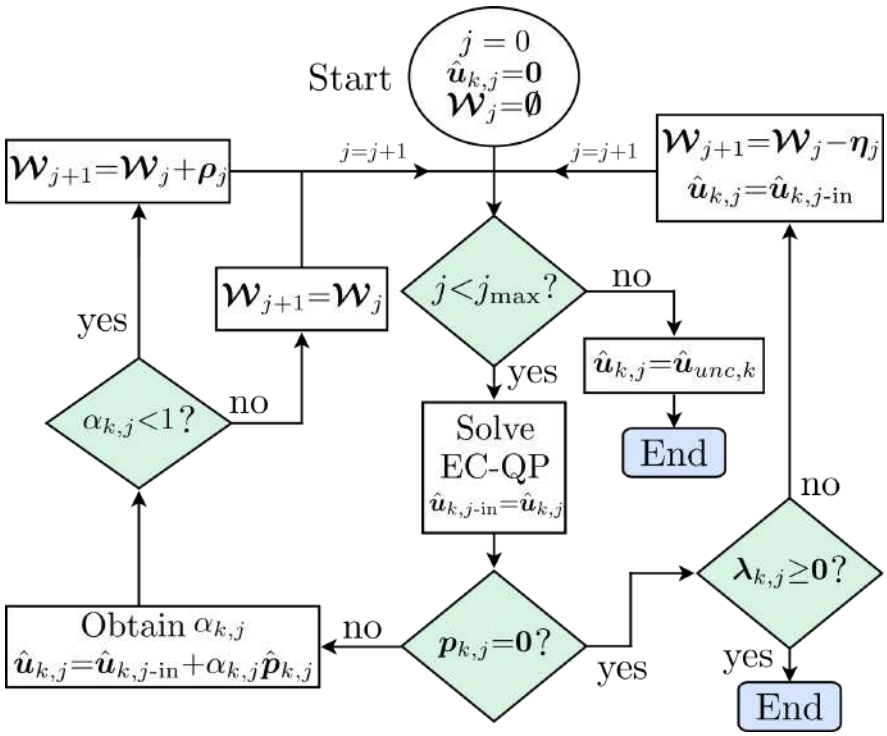

Figure 6.3: Flowchart of the implemented Active-set algorithm. The algorithm is performed at every sampling period.

solution does not satisfy all the activated constraints for (6.18) [109]; therefore, according to the active-set methodology, the constraint $\boldsymbol{\eta}_j \in \boldsymbol{\mathcal{W}}_j$ related to the most negative element of $\boldsymbol{\lambda}^*_{k,j}$ is removed, and a new iteration starts with a reduced set of active constraints (i.e, $\boldsymbol{\mathcal{W}}_{j+1}=\boldsymbol{\mathcal{W}}_j-\boldsymbol{\eta}_j$ and $\hat{\boldsymbol{u}}_{k,j} = \hat{\boldsymbol{u}}_{k,j\text{-in}}$).

On the other hand, if $\boldsymbol{p}^*_{k,j} \neq \mathbf{0}$ it implies that $\hat{\boldsymbol{u}}_{k,j\text{-in}}$ is not the optimal solution of (6.33) and it has to be updated according to

$$\hat{\boldsymbol{u}}_{k,j} = \hat{\boldsymbol{u}}_{k,j\text{-in}} + \alpha_{k,j}\hat{\boldsymbol{p}}_{k,j}, \tag{6.35}$$

where

$$\alpha_{k,j} = \min\left(1; \min_{(m_\gamma,\boldsymbol{k}_\gamma)\in\boldsymbol{\mathcal{V}}_j} \frac{m_\gamma - \boldsymbol{k}_\gamma^T\hat{\boldsymbol{u}}_{k,\text{in}}}{\boldsymbol{k}_\gamma^T\boldsymbol{p}_{k,j}}\right) \tag{6.36}$$

is the "step-length"parameter, $\boldsymbol{k}_\gamma$ is the γ-th row-vector of $\boldsymbol{K}_u$, m_γ is the γ-th element of $\boldsymbol{M}_u$, and $\boldsymbol{\mathcal{V}}_j$ is defined as the set of all non-active constraints that, for every γ-th element, satisfies $\boldsymbol{k}_\gamma^T\boldsymbol{p}_{k,j} < 0$.

If $\alpha_{k,j} < 1$ due to some constraint $\boldsymbol{\rho}_j \in \boldsymbol{\mathcal{V}}_j$, this element $\boldsymbol{\rho}_j$ is added to the active-set $\boldsymbol{\mathcal{W}}_j$ for the next iteration ($\boldsymbol{\mathcal{W}}_{j+1}=\boldsymbol{\mathcal{W}}_j + \boldsymbol{\rho}_j$).

A flowchart of the Active-set algorithm is illustrated in Fig. 6.3. To avoid the potential problem of the algorithm failing to converge, an iteration limit value $j_{\max}$ is set. If this value is reached, the iteration is stopped and the unconstrained solution is used.

In this work a value of $j_{\max}$=9 has been used because, after extensive simulation and experimental work, the algorithm never required more than 9 iterations to obtain the solution. Moreover, this limit was never reached during the experimental testing in any condition.

Therefore, in accordance with (6.15), the applied circulating voltage is determined by

$$\boldsymbol{v}_{\varepsilon,k} = \boldsymbol{v}_{\varepsilon}^{\text{ref}} - \hat{\boldsymbol{u}}_k \tag{6.37}$$

From this formulation, it is worth mentioning that if no constraints are active, then

$$\boldsymbol{v}_{\varepsilon,k} = k_p \hat{\boldsymbol{x}}_k. \tag{6.38}$$

with k_p=- $\left(\frac{\text{L}_\text{b}}{T_s}+2h_{\text{circ}}^{\text{-1}}q_{\text{circ}}r_{\text{circ}}\right)$ as a constant value, which is obtained by using expressions (6.16) and (6.18). Therefore, regulation of the circulating currents is accomplished by a proportional control scheme when no constraints are active.

6.3. Discussion

This section compares the proposed CCS-MPC approach with the M3C control schemes introduced in the previous chapters.

Linear Controllers Approach

- **Total Stored Energy Control:**

  The total stored energy control is achieved by regulating variable ψ_{C_0}. The conventional control scheme which regulates this variable uses a PI controller, where the output signal is the current reference signal of the input port current control. In the presented CCS-MPC approach, the regulation of ψ_{C_0} is based on the same principle: a PI-controller that defines the d-axis current reference of the output port control scheme. Therefore, there is not any particular difference with the previously reported approaches

- **Local Balancing Control:**

  Regarding local balancing control schemes, the presented CCS-MPC approach does not include any additional enhancement or difference from the conventional Phase-disposition PWM (PD-PWM) plus capacitor voltage sorting scheme used in previous works.

- **CCV Balancing Control:**

  In the conventional control based on linear controllers, each of the eight T-CCVs, which indicate the balancing status of the M3C, are regulated independently by eight PI-controllers. This approach is a SISO scheme, where the output signals are used

to construct the circulating current reference signals. The inherent coupling among the circulating currents and CCVs variables in the M3C dynamics are treated as disturbances at each individual control loop. Each output from the PIs define a component of one of the circulating current references; therefore, each current reference is composed of two of the CCVs PI outputs, and the development of the signals requires the estimation of the input/output port voltage phase-angles. If the M3C operates in EFM, an additional control adjustment must be included when the M3C changes from DFM to EFM. Usually, a filter stage is introduced, which implies a low-bandwidth performance of the overall mitigation scheme [21].

Compared with linear control schemes, the proposed CCS-MPC relies on a MIMO approach. The construction of the four circulating current references depends on the eight T-CCV measurements, the predefined input/output port voltages, and the common-mode M3C voltage. This implies that the overall M3C dynamics are considered in the development of all the output signals. Due to no integrator component in the control algorithm, no states are required to be saved. The transition from DFM to EFM does not require additional filter stages, and just the common-mode M3C voltage is needed. As further discussed in the simulation and experimental results chapters, a straightforward gain adjustment is beneficial for better performance. Still, it is not critical and depends on the common-mode voltage magnitude.

- **Arm Current Control:**

  Considering the decoupled input, output and circulating current dynamics obtained from the linear transform, the arm current regulation is commonly based on SISO approaches. Due to the different frequency components found in the circulating current reference signals, proportional controllers are frequently used. The output signals from each control scheme are the corresponding input, output and circulating voltages, respectively, and the saturation schemes of these loops are based on a separated approach, where the information between these outputs is not shared, and the limits are conservatively pre-defined.

  In the presented work, the arm current control includes a MIMO saturation scheme achieved by a CCS-MPC scheme for the circulating current control. The input/output port currents can be controlled with conventional methods using SISO approaches, where input/output port voltages are inputs of the CCS-MPC scheme. The presented approach is particularly attractive because it introduces an overall arm saturation scheme, where the arm current and output voltages limits can easily be integrated. This is especially helpful during transients. If no saturation limit is exceeded, the control law of the circulating current control is set as a conventional P-controller with a time-invariant gain. Conversely, if a limit is reached, the circulating voltages are modified optimally to maintain the arm currents and voltages within the margins. Moreover, this methodology avoids the presence of disturbance in the input/output port currents by only adjusting the circulating currents accordingly.

Control Schemes based on Optimal approaches

- **FCS-MPC approach [35]:**

  This work presents a sub-converter control approach, where the CCV balancing scheme generates negative sequence currents at the input port side. Moreover, the number of possible switching states is intentionally reduced at each sampling period to decrease the computational burden. Unfortunately, this consideration can omit the inclusion of the optimal solution in the search space.

  This FCS-MPC approach differs consistently from the proposed CCS-MPC. Firstly, in the CCS-MPC scheme, the CCV balancing is achieved through the circulating currents, which do not disturb the port currents. Additionally, the optimal solution is analytically obtained. Finally, the presented scheme is able to operate during EFM.

- **Three-stage optimisation approach [36]:**

  This approach is the most similar to the CCS-MPC proposed in this work of all the discussed control schemes. The circulating currents are defined by an optimisation approach, where the input/output port voltages with the common-mode voltages are required. Moreover, this approach can operate in EFM.

  Despite the similarities, the presented approach has only one degree of freedom to adjust the circulating currents. Moreover, it is not straightforward to observe a relationship between this value and system behaviour.

  In the proposed CCS-MPC approach, the strategy is based on an overall M3C model with transformed variables, where each transformed variable is related to a specific cost weight in the MPC formulation. Moreover, an analytical solution is obtained, and there is a direct relationship between the M3C critical operating modes with the available penalty costs. This methodology permits an easier understanding of the relationship between the system response and gains adjustment.

- **Generalised Approach for MMCs with an Optimisation Stage [78]:**

  This scheme is based on a steady-state model of the M3C. The optimal solution is obtained by defining a cost function with limited constraints. Therefore, the user must introduce extra equality constraints to achieve the optimal solution. These user-defined constraints are degrees of freedom that change depending on the M3C application. However, localising a gain adjustment that defines the M3C operation performance is not clear. Moreover, there is not any comment related to critical operating ranges.

6.4. Chapter Summary

In this chapter, the double-stage CCS-MPC approach is presented and discussed. The first stage consists of the CCV balancing scheme, which is based on T-SSCV variables, is defined, and the analytical solution is obtained. The weight costs of the optimisation problems are related to specific operation ranges of the M3C. Moreover, a simple version of the optimal solution is obtained and discussed for DFM operation.

Regarding the second MPC stage, which controls the circulating currents, the cost function's construction with its constraints is thoroughly explained. The weight costs are defined and set equally for all. Afterwards, an active set algorithm is introduced to obtain the solution of the proposed MPC.

Finally, a discussion section shows the comparison of the proposed scheme with the conventional linear controller approaches and those based on optimisation problems.

Chapter 7

Simulation Results

According to the presented methodology, the proposed control scheme is first tested through simulation work on PLEXIM *Plecs* software. The studied system is a 27-cell M3C, where balanced grids are connected at both the input/output ports. In the case of the input side, the utility grid has fixed magnitude and frequency, and is connected through series inductors L_{rst}. On the other hand, the output port grid is variable in amplitude and frequency, and it is connected through series inductors L_{uvw}. The variable output port grid is a degree of freedom of that can be used, for instance, to emulate an electrical machine.

The system details are specified according to the experimental prototype used and they are given in Table 7.1. Figure 7.1 exhibits the overall control scheme implemented in the simulation work, and Table 7.2 shows the controller parameters, where a sampling period of 160μs was used for the controllers and the carrier period.

Table 7.1: System parameters used in simulation work.

Experimental Prototype Parameters		
Number of Cells	n	27
Arm/port Inductances	L_b - L_{uvw} - L_{rst}	2.5mH - 2.5mH - 5 mH
Cell Capacitance/Voltage	C - v_C^{ref}	4.7mF - 133.33V
Port-grid line voltages	$V_{LL\text{-}rms}^{uvw}$ - $V_{LL\text{-}rms}^{rst}$	183.7-183.7 V

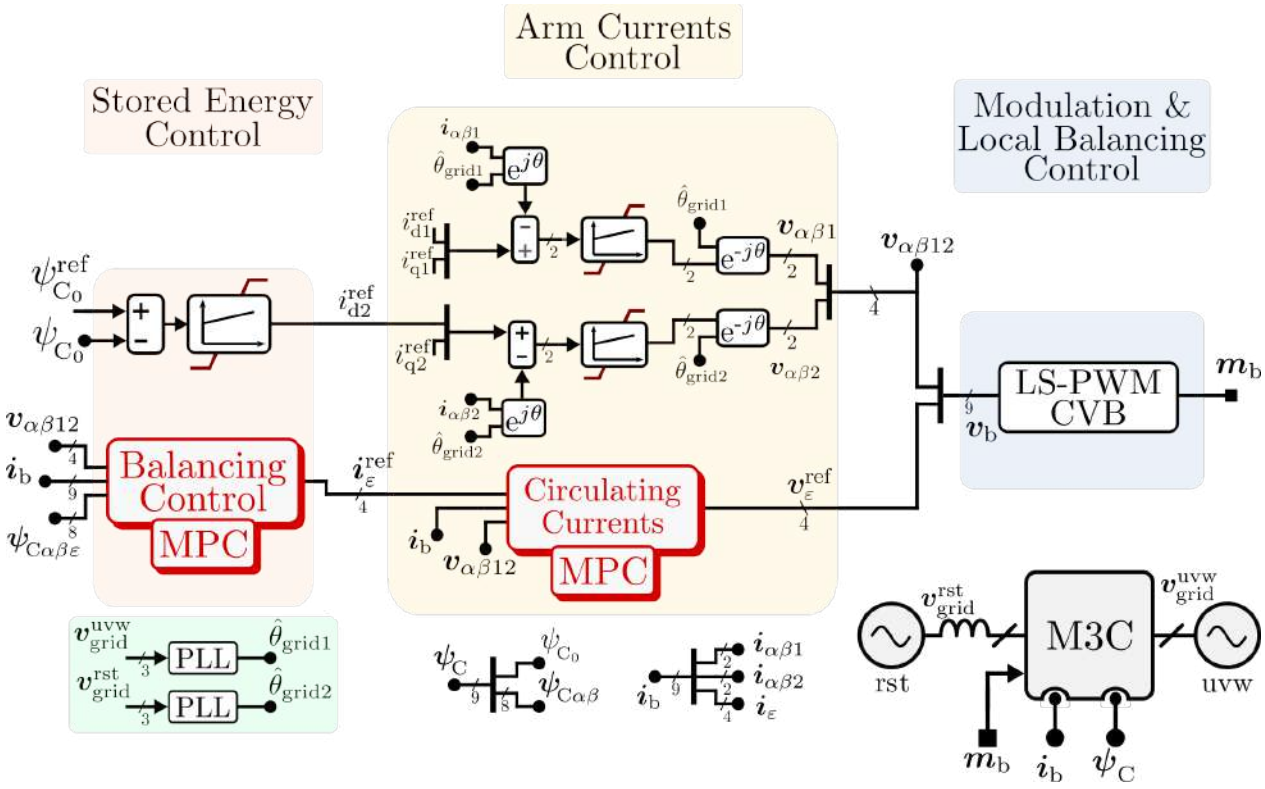

Figure 7.1: Overall control scheme used in PLECS simulation.

Table 7.2: Controller parameters for simulation tests.

Controller Parameters		
Sampling/Carrier Period	T_s	$160\mu s$
uvw-port Current Control	BW - ξ	166Hz - 0.756
rts-port Current Control	BW - ξ	230Hz- 0.938
Circulating Currents Control	BW - ξ	111Hz - 0.999
Total Stored Energy Control	BW - ξ	2.4Hz - 0.6
CCS-MPC Circulating	r_{circ} - q_{circ}	5 - 1
CCS-MPC	r_ε - q_0	1e5 - 5

As depicted in Figure 7.1, the total stored energy control is achieved by regulating $\psi_{C_0}^{\text{ref}}$ with a PI-controller. The output PI-controller signal is the d-axis current reference i_{d2}^{ref} that goes into the output port current control. Vector control schemes accomplish the input and output port current control with synchronous reference frames aligned with the corresponding grid phase-angles. The output port dq-axis reference signals, with the amplitude and frequency of the grid, are degrees of freedom. The local balancing of the system is achieved through a generic sorting algorithm with PD-PWM. [80].

The simulation results are grouped into two main sections: (A) CCV-Balancing Scheme Performance, and (B) Saturation Scheme performance of the Circulating current Control.

7.1. CCV-Balancing Scheme Performance

In this section, the presented results are exclusively focused on testing the performance of the CCV balancing scheme based on CCS-MPC described in Section 6.1, therefore, the saturation scheme proposed in Section 6.2 is not active in any condition.

7.1.1. Steady state performance at different weight costs

In this subsection, several tests were performed in DFM and EFM in order to observe the performance of the scheme in steady state at different cost weights $\boldsymbol{Q}_{\mathrm{e}}$ and $\boldsymbol{R}_{\mathrm{e}}$.

Diferent weight costs in DFM

In this operation mode, the output port power is set to 6.75kW/6.75kVAr, and the line voltage for both grid ports is set to 183.7V RMS. Five different output frequencies were tested: 10, 20, 30, 40 and 45 Hz. The MIMO gain $\boldsymbol{K}_{\mathrm{e},k}$, defined by (6.11), is varied by adjusting the ratio r_{e}/q_0 from 1e5/0.5 to 1e5/40, which is achieved fixing r_{e} at 1e5 and increasing q_0 from 0.5 to 40. Fig. 7.2 illustrates the maximum CCV ripple (referred to as CVV ripple max.), peak value of T-CCV (T-CCV max.), maximum amplitude of the circulating currents and the maximum value of the arm currents for all the performed tests. Both the CVV ripple max. and the T-CCV max. are shown as percentages of 400V, which defines $\psi_{\mathrm{C}_0}^{\mathrm{ref}}$=$400^2\mathrm{V}^2$. Initially, it is observed that when q_0 is increased, the maximum amplitudes of the circulating and arm currents increase consistently for all the working frequencies. Although CCV ripple max. and T-CCV max. have relatively low magnitudes at q_0=0,75, their magnitudes decrease even more as the weight is increased. However, since the maximum amplitudes of arm and circulating currents increase strongly at higher q_0, the corresponding currents can be excessive in comparison with those obtained at the initial cost weight. Therefore, the value q_0=0,75 is adopted as a good compromise because the CCV maximum ripple is regulated within an acceptable margin with lower current amplitudes.

Although the maximum CCV ripple tends to decrease as the frequency is increased, at 45Hz the ripple of the CCVs behaves conversely with respect to the ripple value obtained at 40Hz. This behaviour is produced because of the small value of $|\omega_1 - \omega_2|$; i.e. the low frequency energy terms of (3.23)-(3.24) become dominant with respect to the others. It should be noted that the CMV is set to zero for all these results, and its impact is not measured in the analysis of DFM.

Diferent weight costs in EFM

In this section, a similar study has been undertaken for EFM at a single output frequency of 49.5Hz with positive sequence, for different CMV amplitudes. The nominal CMV is defined as a 100Hz sinusoidal waveform with an amplitude of 40V (10 % of the CCV reference value). The results are shown in Fig. 7.3, where the same variables (max. CCV ripple, max. T-CCV, peak circulating current and peak arm currents) are shown at different values of the CMV

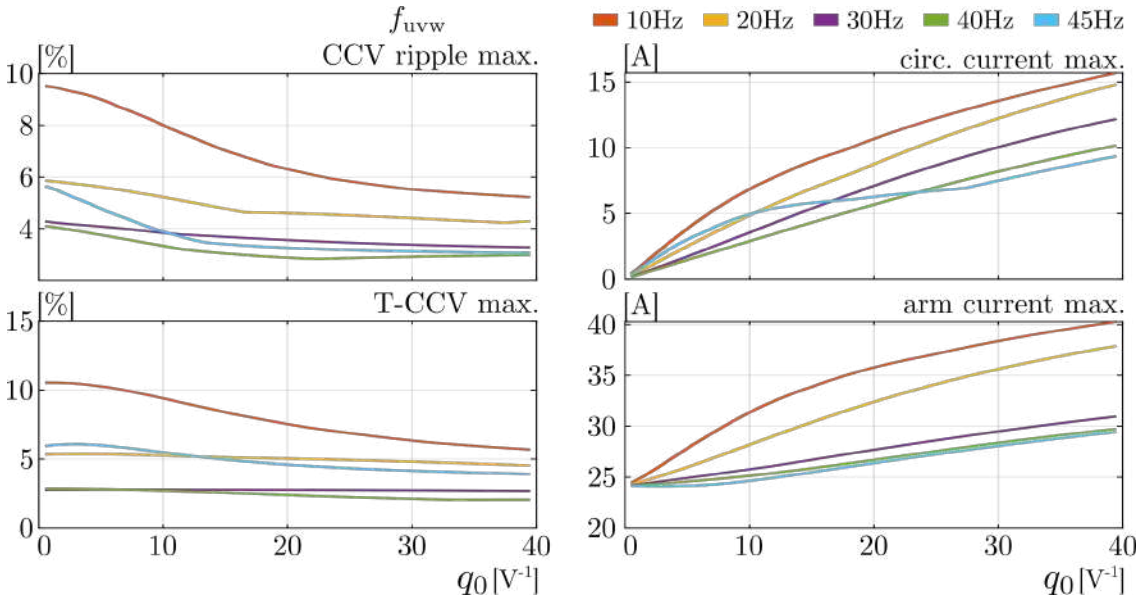

Figure 7.2: DFM steady state performance at 10, 20, 30, 40, 45Hz at different weight cost q_0. CCV ripple The operating conditions for both input output port were the same.

amplitude (100 % corresponding to 40V). Additionally, $q_{\varepsilon 12}$=q_0=0,75, r_e=1e5 and $10 < q_{\varepsilon 34} < 170$. From the results shown in Fig. 7.3, it can be seen that the arm current maximum tends to settle to (different) constant values for 100 % and 80 % CMV as the cost weight $q_{\varepsilon 34}$ is varied. For the 60 % and 50 % CMV values the arm current is still increasing when the maximum cost weight considered is reached. The CCV ripple max and T-CCV curves become more linear when the CMV is decreased. An interesting result is obtained for the CMV amplitudes of 100 % and 80 %, where the maximum T-CCV and CCV ripple max curves tend towards constant values. Finally, it can be concluded that during EFM, the maximum values of all the studied variables are highly dependant on the CMV amplitude, regardless of whether a high cost weight is used. For instance, to obtain 6 % for the maximum CCV ripple, $q_{\varepsilon 34}$ has to be tuned at 35, 57,109, $169V^{-1}$ for CMV amplitudes of 100 %, 80 %, 60 % and 50 %, respectively. For these cost weights, the resultant arm peak currents are, respectively, 25.1A, 26.5A, 29A and 31.4A. Therefore, for CCV ripple mitigation purposes, if the CMV amplitude is sufficiently high, the increasing rate of the arm current amplitude with respect to $q_{\varepsilon 34}$ become less relevant, and a higher penalty cost does not necessarily imply a significant increase in current amplitudes. Conversely, at lower CMV values, the circulating current amplitudes tend to acquire a linear relationship with $q_{\varepsilon 34}$, and the impact starts to be noticeable. In this range, tuning of the cost weight $q_{\varepsilon 34}$ is an important consideration in terms of the permitted maximum arm current.

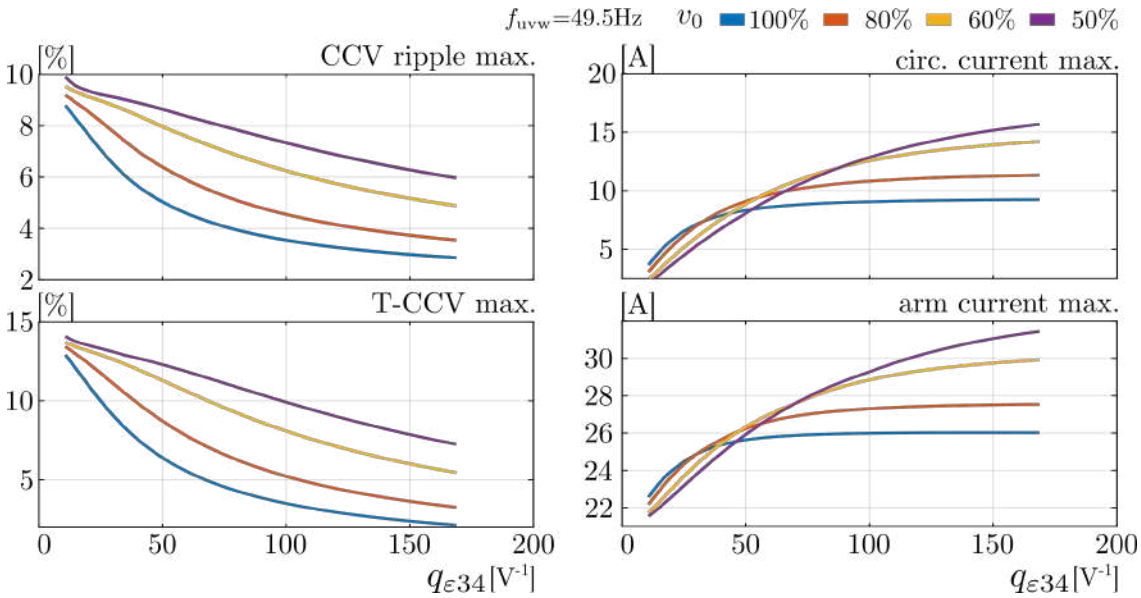

Figure 7.3: EFM steady state performance at 49.5Hz operation with different v_0 amplitudes and weight cost $q_{\varepsilon 34}$. Weight q_0=$q_{\varepsilon 12}$=0,75 in all scenarios.

7.1.2. EFM steady state performance with different CMV waveforms

Although the study of different CMV is out of scope in the presented work, it is worth highlighting that the proposed CCS-MPC scheme automatically adjusts the circulating current according to the CMV, regardless of the shape and frequency. In this section, the steady-state performance of the M3C with two different types of CMV with the same amplitude is presented: (a) Sinusoidal waveform, and (b) Trapezoidal waveform. The output grid power is set to 6.76kW/0.45kVAr at 49.5Hz, the CMV amplitude is 40V at 100Hz for both waveforms, the CCV reference value is 400V, and both grid voltages are 183.7V RMS line. Additionally, q_0=0,75, $q_{\varepsilon 12}$=75, and r_e=1e5. Figure 7.4 shows results for both cases, illustrating the CCVs and T-CCVs (in percentage of 400V), the circulating and arm currents, and the CMV (in percentage of 400V). As demonstrated, both cases exhibit good regulation of the CCV oscillations. The maximum ripple amplitudes are 5.3 % and 4.5 % for cases (a) and (b), respectively. This difference is also noticed in the arm currents where the maximum measured values are 22.15A and 21.65A for cases (a) and (b). A similar trend is seen in the circulating current. The reason why the CMV in (b) gives lower current and CCV amplitudes is related to the harmonic content of the trapezoidal shape. In this particular case, the fundamental has a value of 12.1 %, with a peak value 20.1 % higher than that of the sinusoidal form. Moreover, there are extra odd harmonics that have an impact in mitigating the low frequency terms of (3.23)-(3.24). This can be confirmed by the circulating current waveform shown in (II.b), where it takes the trapezoidal form in comparison to the shown in (II.a). As aforementioned, this current shape is generated automatically by the proposed control scheme, no extra considerations have to be made in the scheme other than to define the waveform of of v_0 in (6.8).

Although the inclusion of trapezoidal or square shapes can enhance the regulation of the CCVs with lower arm currents [120], the sinusoidal waveform is preferred in this work. The main reason for this decision is based on the issue of regulating circulating currents with high harmonic content using PWM schemes. Non-sinusoidal waveforms cannot be faithfully reproduced without using a high frequency index, which it implies an increasing of the carrier frequency in the PWM scheme and is not always possible [121]. In the Future Work section, further studies on the CMV waveform and frequency are recommended.

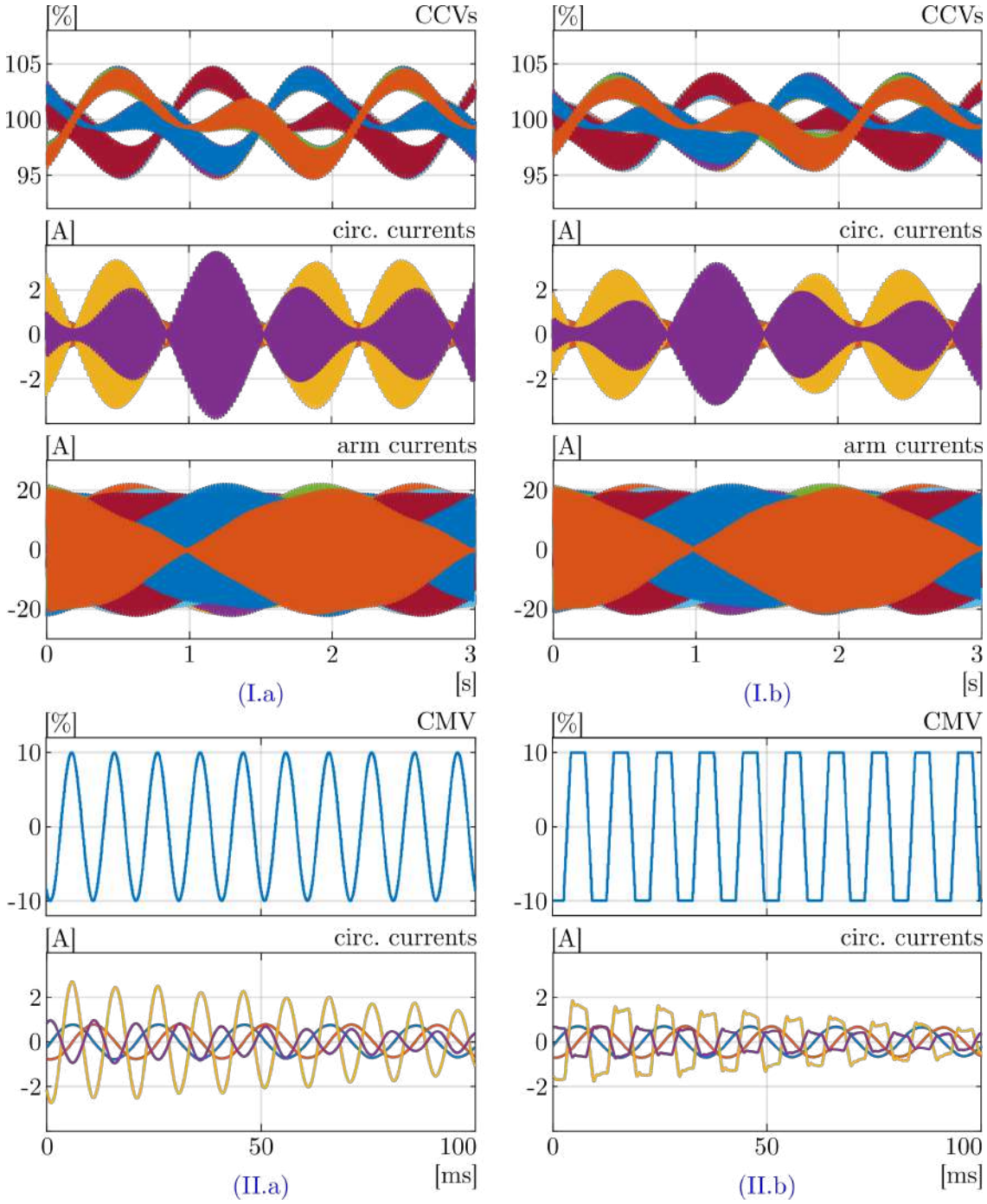

Figure 7.4: Simulation results of steady operation of during EFM with different v_0 waveform. (a) Sinusoidal shape. (b) Trapezoidal waveform. (I) Time frame of 3s. (II) Time frame of 100ms.

7.1.3. Dynamic ramp test in DFM operation

In order to verify the performance of the scheme during DFM, a start up ramp test is performed. At constant d-axis output port current, the frequency of the output port is linearly increased from 0Hz to 45Hz. The output port grid voltage is proportional to the output frequency, starting from 1V to 183.7V line voltage at 45Hz. The output port dq-axis currents are constant during the test, with the power reaching 6.75kW/0.9kVAr at 45Hz. The weight costs are r_ε=1e5 and q_0=5 during the whole test and the CCV reference value is set to 400V.

Fig. 7.5 depicts the results obtained in the test. Initially, at 2s, the uvw port d-axis current is suddenly changed to 15A with f_{uvw}=0Hz. Afterwards, at 2.5s, the frequency starts to increase at a constant rate until it reaches 45Hz at 11.5s. Fig 7.5(a) depicts the CCVs (as a % of 400V), output port frequency f_{uvw}, output port active and reactive power (P_{uvw} and Q_{uvw}, respectively as a % of 6.75kVA), circulating currents, arm currents, and dq-axis port currents during the whole test. Without losing generality, this behaviour emulates an electrical machine starting at a constant torque value. The CCVs ripple is below 5 % and the arm currents exhibit a smooth increase according to the transition of the output port voltage/frequency. The output power also smoothly increases following the frequency/voltage rise in the output port, without any disturbance.

Figure 7.5(b) shows a 0.3s interval of the same test while the frequency is 0Hz. Specifically, it illustrates the CCVs, arm currents, input/output port currents, and circulating currents when the output port d-axis current suddenly changes to 15A. As illustrated, the CCVs exhibit small oscillations after the transient, which are directly linked with the pair $\psi_{\text{C}_{\varepsilon 1}}$-$\psi_{\text{C}_{\varepsilon 2}}$, as previously indicated in Table 3.1 and in (3.12). The arm and output port currents persist with DC components after the d-axis step-change, as expected, with a stable a smooth response in the CCVs. The results demonstrate that at 0Hz with high torque and low power, the converter operates properly without any additional consideration than those specified for DFM applications. This is possible if the back-emf of the machine is low at this frequency range because the required power to start it up will be small. Therefore, it can be seen that the strategy presented is suitable for starting an electrical drive at constant torque from rest.

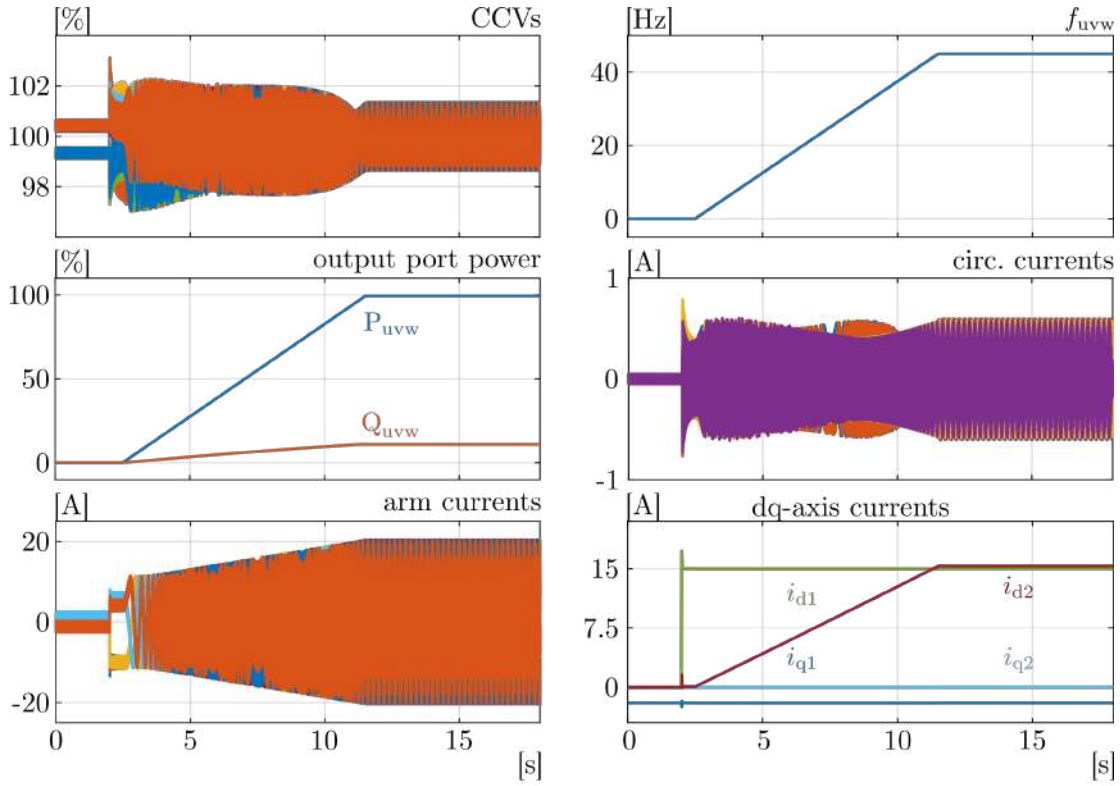

Figure 7.5: Dynamic ramp test from 0Hz to 45Hz output port frequency at constant output port dq-axis current references. (a) Complete time interval. (b) Time interval between 1.9 and 2 seconds.

7.1.4. Dynamic balancing test

To observe the dynamic performance of the scheme at different cost weights, the CCVs are intentionally distributed within a ±20 % spread of the nominal value. To achieve steady state operation with distributed CCV values, the T-SSCV reference signal $\boldsymbol{\psi}^{\mathrm{ref}}_{C\alpha\beta\varepsilon}$, shown in Fig. 6.2, is set with the desired non-zero perturbations. Afterwards, at 0.1s, $\boldsymbol{\psi}^{\mathrm{ref}}_{C\alpha\beta\varepsilon}$ is suddenly changed to zero. The grid voltage at both ports is set to 183.7V, and the output port is operating at 25Hz with power of 6.76kW/0.9kVAr. The CCV reference value is set to 450V for the duration of the test. Figure 7.6 illustrates the CVVs, the circulating currents, the arm currents and dq-axis port currents at two different cost weights: (a) q_0=0,75 and (b) q_0=5. In Both cases, r_ε=1e5.

From the results, it is clear that case (b) has a faster response than case (a). This is because the ratio r_e/q_0 is lower in case (b) and, therefore, the gain $\boldsymbol{K}_{\mathrm{e},k}$ has a higher value as described in section 6.1.1. The higher gain gives a faster response, which requires a larger circulating current than case (a). For example, the transient studied produces an arm current peak of 21.5 in case (a) and of 29.7A in case (b). The input d-axis current, related to the Total Stored Energy Control, has a small disturbance in case (b), which originates from the rapid change in the CCV values. The settling times are approximately 0.9s in case (a) and 0.2s in case (b). In case (a), the circulating current injection has a negligible influence on the arm current amplitudes which can be favourable to avoid hitting limits.

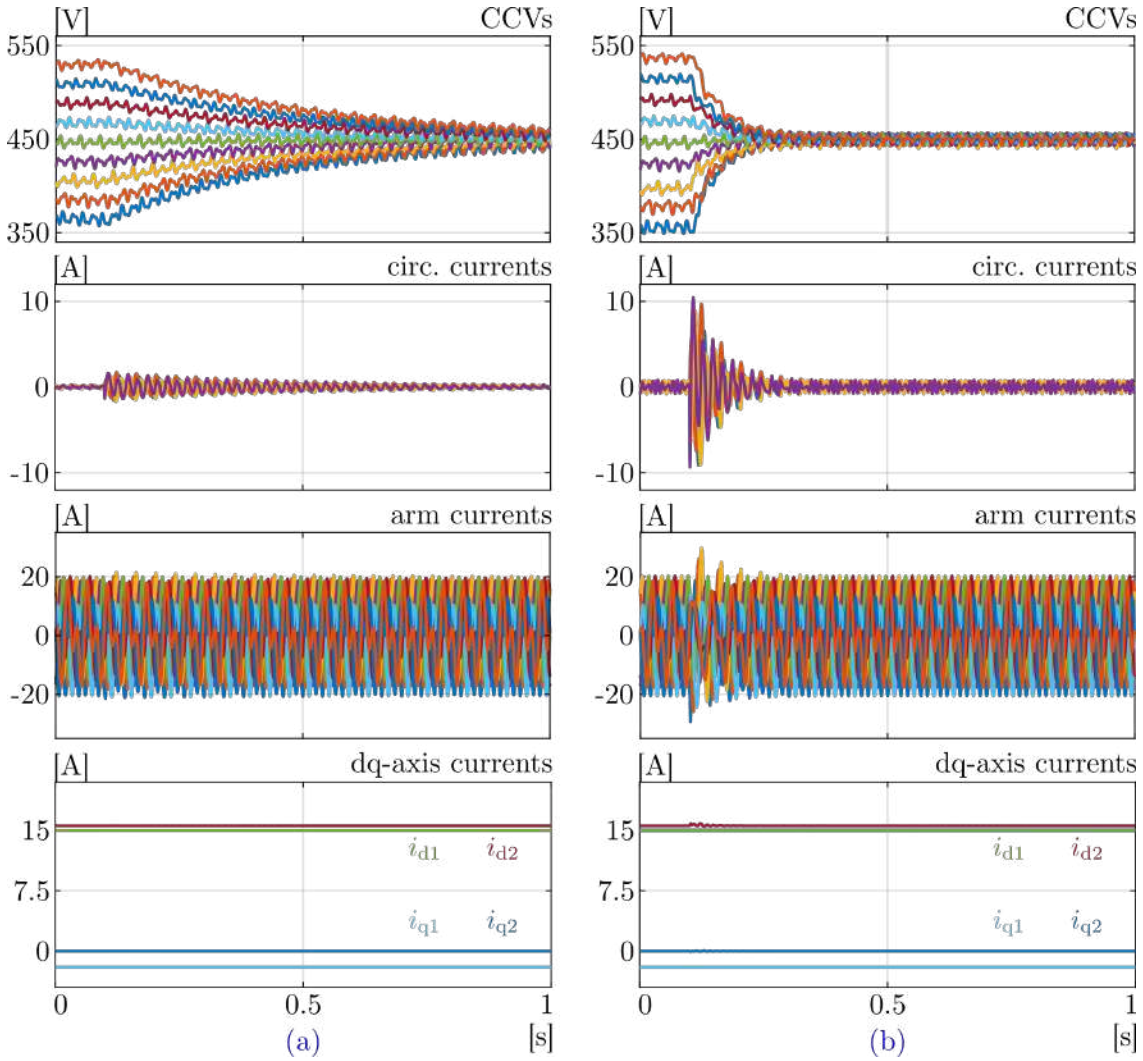

Figure 7.6: Sudden balancing test from perturbed CVV values. (a) q_0=0,75. (b) q_0=5,0.

7.2. Saturation Scheme performance

In this section, the presented results exclusively evaluate the performance of the Circulating Current CCS-MPC saturation scheme described in Section 6.2. The system and controller parameters are depicted in Table 7.1 and Table7.2.

7.2.1. Performance of the Proposed Control Strategy during sudden Step Changes in the Output Port Currents

In this section, the active power at the load side is suddenly stepped to a relatively high value by modifying the d-axis current reference of the output port to 27 % above the nominal value ($I_{d2}^{ref} = 19A$). After 300ms, this reference is decreased to the nominal value ($I_{d2}^{ref} = 15A$). At nominal conditions, the system is operating at 6.75kW/0.45kVAr/25Hz at the output port. The arm limit from the MPC saturation scheme is set to 24.5A. This test could emulate (for instance) a load impact on a motor drive.

The test starts at 50ms seconds (see Fig. 7.7), where the d-axis current reference of the uvw port is stepped from 0A to 19A for 200ms; afterwards, it is changed from 19A to 15A. The q-axis currents of the input/output ports are set to a constant value of 0A and -1A, respectively. The simulation results are shown in Fig. 7.7, where the arm currents, CCVs, circulating currents and the dq-axis input/output port currents are illustrated. Two scenarios are considered, the first one (left hand side of Fig. 7.7) shows the simulation results when the arm current saturation is not activated. At the right hand side the saturation scheme-B is enabled.

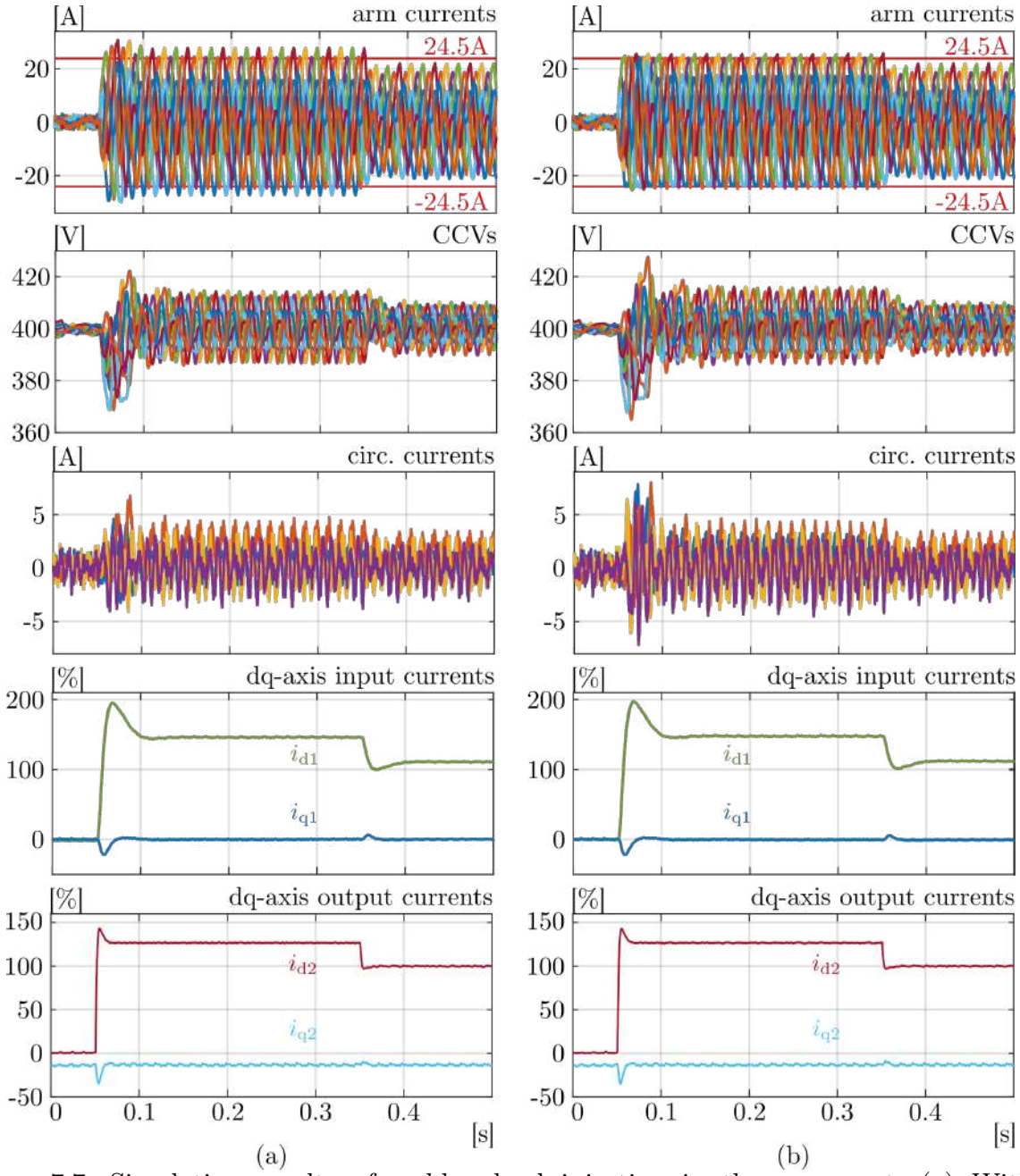

Figure 7.7: Simulation results of sudden load injection in the uvw port. (a) Without saturation; (b) Saturation scheme-B.

As shown, to maintain the energy balance, in both scenarios the sudden change of the output port d-axis current generates a fast increase of the d-axis power current current at the input port, which is driven by the Total Stored Energy Control. As shown in the arm-currents, when the no-saturation scheme is utilised, the arm currents have initial peaks near 30A (22.4 % higher than the 24.5A limit). For the scheme-B, the arm current peaks are decreased in amplitude to the 24.5A limit, with small current spikes around the defined bound. This implies that, in terms of arm current limitation, the proposed saturation scheme accomplishes the goal.

Due to the sampling process, there are current spikes above the limit, which are related to the modulation scheme (PD-PWM). These spikes are not necessarily measured, so the algorithm cannot take any action to limit this value. To obtain a better regulation, the peak value of the ripple could be considered when defining the value $I_{\max}$ [see (6.18)], for instance by setting the current limit to a lower value instead of 24.5A. This will mainly depend on the inductance values of the system and the carrier frequency.

For the simulation results presented in Fig. 7.7, using the saturation scheme-B in the control algorithm does not affect the regulation of the input/output currents of the M3C. Both the non-saturated and saturated cases show good performance in the regulation of the external dq-axis port currents. Additionally, in both scenarios, the CCVs exhibit relatively high magnitude spikes at the very beginning, which are related to the natural response due to the high load impact (the d-axis current is directly linked with the active power of the grid power supplies). Although the circulating currents have higher values in case (b) than in the non-saturated case, the arm-currents have lower peaks. This interesting feature is inherent to the proposed control strategy to maintain the cluster currents inside the predefined limits.

7.2.2. Performance of the Strategy when CCVs constraints are active

Although the proposed saturation scheme is intended to be mainly used during transient instances, the performance of the strategy is evaluated when the output cluster voltages periodically reach their CCVs limits. This situation emulates a system where the summation of the peak voltages at the rst and uvw ports are comparable to the CCV values.

To enter this operating condition, the input/output port grid voltages were increased an 12 % of the values specified in Table 7.1. Fig. 7.8 illustrates simulation results of this condition for the MPC saturation scheme-B with the output uvw d-axis and q-axis currents set to 15A and to -1A, respectively. The d-axis input port current was specified according to the Total Stored Energy Control.

The output cluster voltages $\boldsymbol{v}_{\mathrm{b}}$, with the ±CCVs, arm currents, circulating currents, active constraints, and input/output port currents are depicted in the attached figure.

As depicted in the upper-left side graph, the output cluster voltages ($\boldsymbol{v}_{\mathrm{b}}$) have several saturation periods due to the CCV limits. The number of active constraints plot, middle-right graph, depicts the number of active constrains. By inspecting the graphic located at the left-top of Fig. 7.8 it is concluded that most of the times it is an active CCV-related constraint

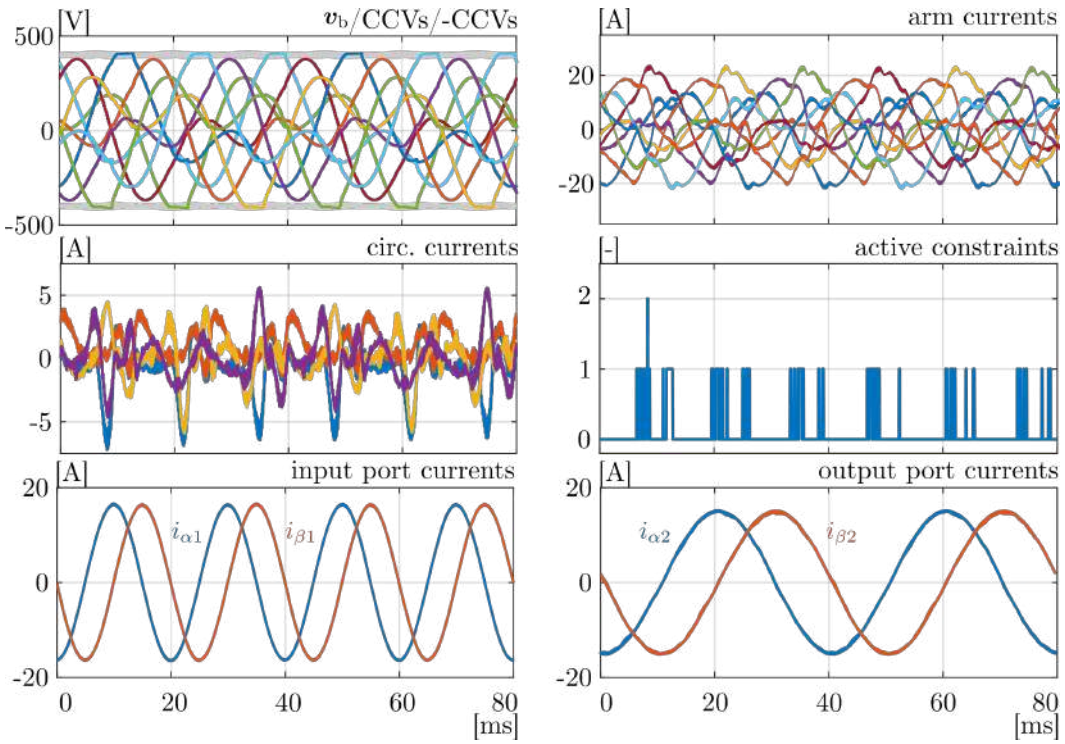

Figure 7.8: Simulation results considering saturation of output cluster voltages. Description from upper-left to the right and down: (1) output cluster voltages $\boldsymbol{v}_{\mathrm{b}}$ [coloured lines], CCVs and -CCVs [grey lines]; (2) arm currents; (3) number of active constraints; (4) circulating currents; (5) dq-axis rst-port currents; (6) dq-axis uvw-port currents.

(see the saturated tops of some of the waveforms). During all of the test, it is shown that the input and output port currents are unaffected when the arm is saturated, as depicted in their respective $\alpha\beta$ current plots. The circulating current could have some relatively high current peaks when a constraint is active, but the arm currents do not surpass the maximum limit of 24.5A when these peaks occur.

7.2.3. Performance of the Saturation Scheme-B Considering a Dynamic Balancing Test

To evaluate the performance of saturation scheme-B, a Transient Balancing Test (TBT) is performed: the stored energy in the M3C is intentionally unbalanced by using non-zero reference signals in the MPC CCV balancing scheme (see Figure 6.2). Then, the T-SSCVs references are suddenly changed to zero to induce high circulating currents for balancing the converter energy. The dq-axis currents of the output port are fixed at 15A-0A (6.75kW/0kVAr). In order to avoid CCVs limitations due to the forced imbalanced condition, the average CCVs reference used in the Total Stored Energy Control is set to 450V. The results are illustrated in Fig. 7.9, where the arm currents, CCVs, circulating currents, and $\alpha\beta$ input/output port currents are shown for two scenarios: (a) Without saturation scheme, and (b) Saturation scheme activated with an arm current limit of 24.5A. For both cases, the predefined operating conditions are the same.

From the figure, it can be seen that the arm currents are considerably reduced in case (b). Specifically, the arm current peak is decreased from nearly 40A to the defined limit of 24.5A. As can be seen in case (b), the arm currents exhibit saturated waveforms in their amplitudes.

Because of the saturation, the balancing period of the CCVs in case (b) is around 50ms longer than case (a). This behaviour is excepted in this case, since the balancing performance is limited due to the introduced MPC saturation. This can be seen in the circulating current waveforms of case (b), which have lower amplitudes than case (a) and have less smooth shapes. Regardless of the case, the input/output port currents are not affected during the test. This can be seen in the $\alpha\beta$ currents, which are basically the same in both cases.

7.2.4. Comparison of Saturation Scheme-B with a saturation scheme based on upper-level adjustments

To compare the performance of the saturation scheme with previous works, such as those reported in [24, 21], the MPC scheme-B is compared with a saturation scheme based on the adjustment of the CCV control scheme. Generally, the circulating current references defined by the CCV control scheme can be limited by two approaches. The first approach is to lessen the controller's bandwidth by tunning all the SISO controllers to a slower response. The other decreases the saturation limit of all the SISO controllers. Regardless of the methodology, both options aim to reduce the circulating current amplitudes during a transient performance. Conversely, the proposed CCS-MPC automatically limits the circulating currents if the

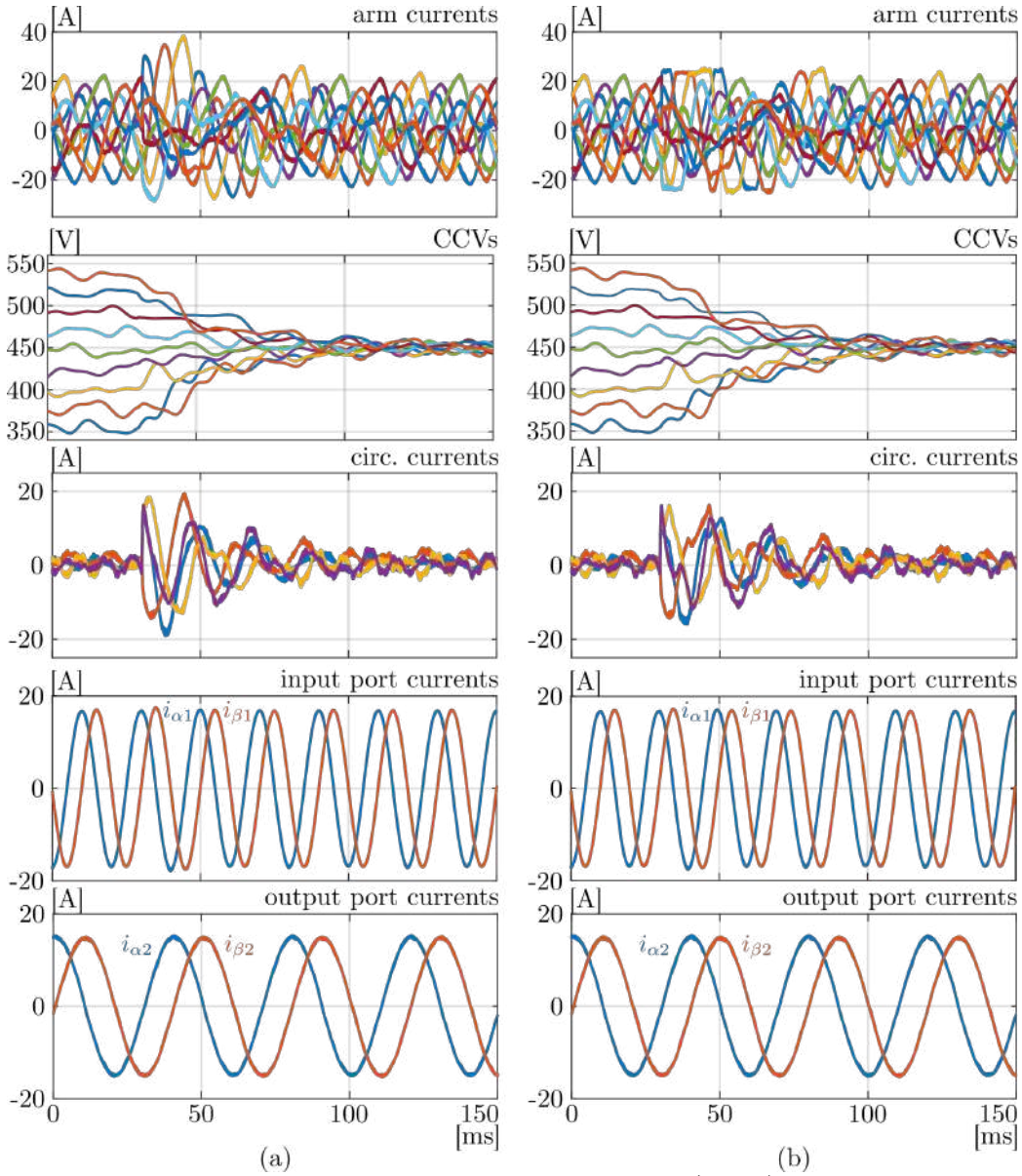

Figure 7.9: Simulation results of Transient Balancing Test (TBT) with the MPC saturation scheme activated with 24.5A limit. (a) Without saturation scheme (b) Saturation scheme-B enable with 24.5A.

maximum arm current limit is reached, without requiring any extra modification in the upper CCV control scheme.

In this section, two cases of TBT are performed with the same conditions shown in section . The two exhibited cases are (a) MPC scheme-B with 24.5A of arm current saturation and q_0=5, and (b) Disabled MPC saturation with q_0=2. The output port frequency is 35Hz for both scenarios; therefore, the MPC is in DFM operation. The results are shown in Figure 7.10.

As depicted in the results, both arm currents peaks reach ±24.5A as maximum levels. However, the corresponding circulating current amplitudes differ considerably. In case (a),

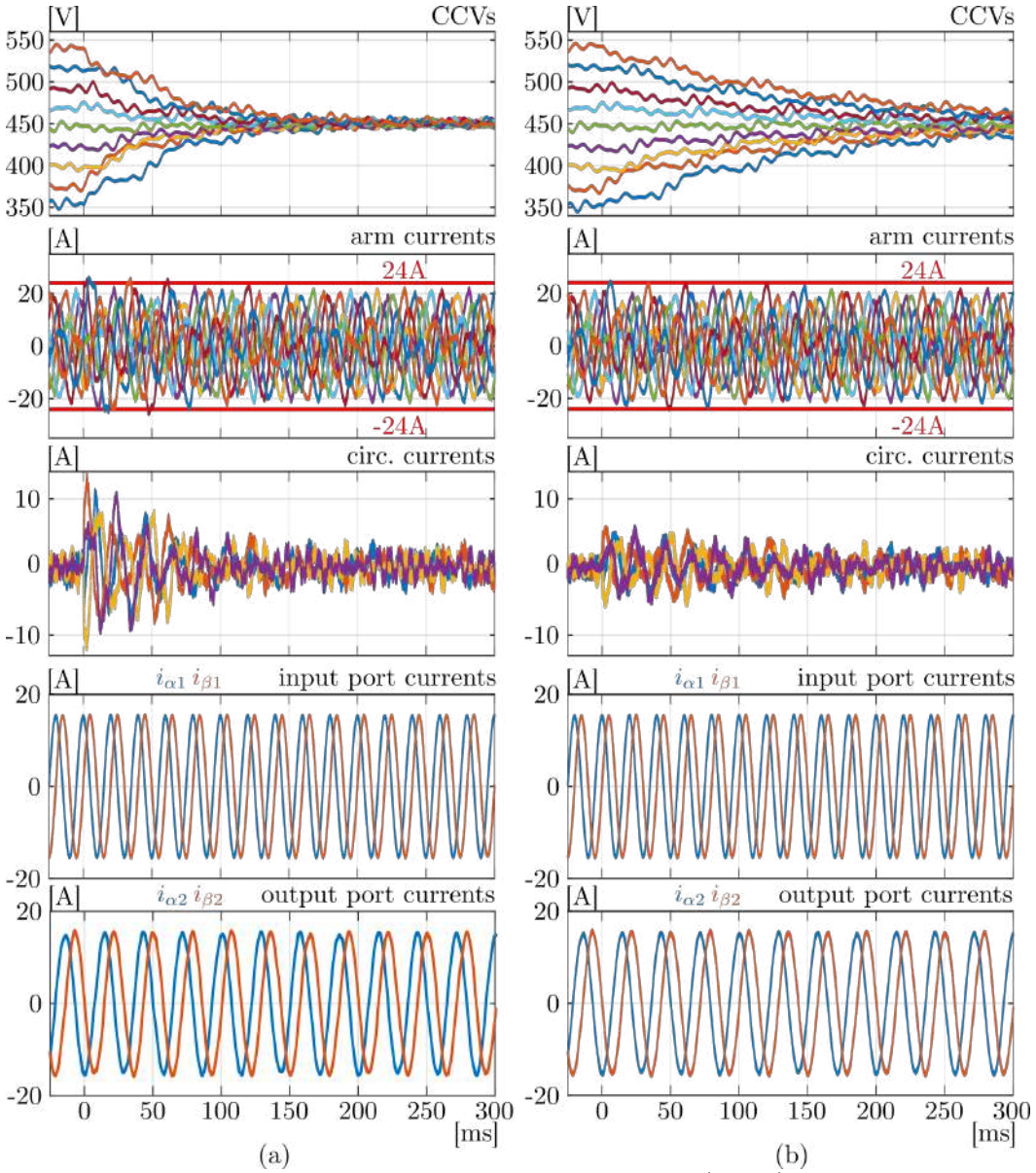

Figure 7.10: Simulation results of Transient Balancing Test (TBT) with the MPC saturation scheme activated at 24.5A limit and with CCV limitation. (a) Saturation scheme-B enable with 24.5A (b) Saturation scheme based on CCV control limitation.

the circulating current peaks are near 13A, whereas in case (b) are near 6A. Moreover, the CCV balancing performance is noticeably faster for case (a) rather than case (b). This faster response is produced because the MPC algorithm maximises the circulating current amplitudes without surpassing the maximum value allowed in the total arm current. Conversely, case (b) decreases the performance of the upper control stage, rendering sub-optimal performance. Furthermore, it is necessary to mention that defining q_0=2 in case (b) implies that the resultant arm current peaks are near 24.5A for the analysed TBT, which is the set limit for the MPC scheme-B for case (a). However, if another transient condition is required, the resultant arm current peaks could surpass these limits. Therefore, the limitation of the arm currents by adjusting the upper CCV controllers does not ensure the same arm

current maximum peaks for any case due to it being an open-loop adjustment.

Finally, for both scenarios, the input and output port currents are not distorted during the TBT, as depicted in their corresponding $\alpha\beta$ components. This behaviour is expected and follows the same tendency shown in the previous results.

7.3. Chapter Summary

In this chapter, simulation results of the proposed CCS-MPC scheme were exhibited, showing and analysing its steady-state and transient performance. Initially, the CCV balancing scheme performance is initially evaluated through several steady-state results. CCVs, T-CCVs, arm currents and circulating currents peak values are compared at different frequencies and weight costs in DFM operation. Similar results are shown at 49.5Hz output port frequency with different weight costs and common-mode voltage amplitudes for EFM operation. Finally, results at EFM with two different common-mode voltage waveforms but the same amplitude were analysed. Transient performance was evaluated with a sudden balancing test at DFM operation, where the CCVs are intentionally imbalanced and, then, the scheme is activated. Furthermore, a dynamic ramp test from 0Hz to 45Hz with a sudden output port current injection is shown.

Additionally, in the second CCS-MPC stage, several conditions that activate the saturation scheme were shown. Initially, the CCV constraints were activated, and the adjustment of the circulating currents to keep the input/output port performance is shown. Afterwards, the arm current constraints were activated by forcing the output port currents and, secondly, inducing high circulating currents in a balancing test. Finally, a comparison of MPC scheme-B with a method based on the limitation of the CCV control performance is introduced. The exhibited results show that the proposed scheme considerably enhances the performance of the CCV scheme.

Chapter 8

Experimental Validation

8.1. Experimental Set-up

To carry out the experimental validation in accordance with the proposed methodology, a prototype of a M3C available in *Power Electronic Control and Electrical Drives Laboratory* of the Electrical Department of the University of Chile (UCH) was used.

The description of the set-up is divided into the Control Platform and Power-stage sections, as shown below.

8.1.1. Control Platform

The purpose of the control platform is to measure the system variables summarised in Table 8.1, to perform the overall control routine, to define the firing pulses of the H-bridge legs, and to communicate with the PC host. For the implemented experimental prototype, the control platform used was composed of a DSP with three FPGA daughter boards. Additionally, the platform has a Host Port Interface (HPI) daughter board used to enable PC/DSP communication, and a fiber optic transmitter board. Moreover, a Host Port Interface (HPI) daughter board is used to enable PC/DSP communication.

(a) (b)

Figure 8.1: Control Platform: DSP, FPGAs, transmitter and HPI boards: (a)perspective view, (b)top view.

8.1.2. DSP Board

The DSP is a TMS320C6713 model, depicted in Figure 8.2 (a), with a 32-bit floating point architecture running at 225 MHz. The general architecture of the DSP is illustrated in Figure 8.2 (b), where the External Memory Interface (EMIF) supports 64MB of on board SDRAM memory, Flash ROM, and also a memory interface through an external bus connector. The access to the EMIF clock is limited to 100MHz.

The control algorithm was implemented using C language through Code Composer IDE; additionally, the HPI allows an uninterrupted communication between the host PC and the DSP's processor via an USB port. The communication interface between the host and the DSP is performed by Matlab with real-time interaction for data acquisition.

Table 8.1: Number of required measurements for the experimental M3C system prototype.

Variable	N° Measurements
Arm current	9
Capacitor Voltages	27
Output Port Voltages	4
Total	40

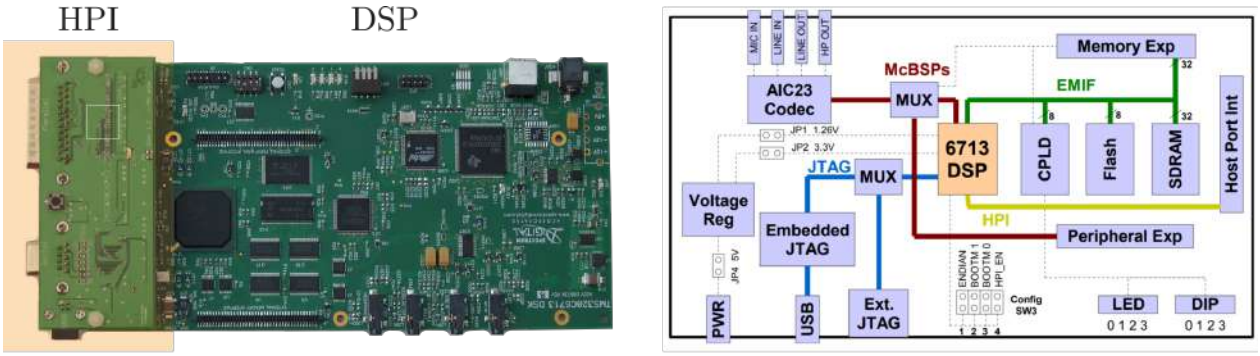

(a) (b)

Figure 8.2: TMS320C6713: (a) DSP+HPI board top view (b) overall architecture.

Daughter Boards

In addition to the DSP, the control platform is conformed of several daughter boards, where three FPGA boards were used. Specifically, the FPGA boards used in this work were designed by the PEMC Group of the University of Nottingham, which are based on a ProASIC3 FPGA with ten 14-bit A/D converters to measure analogue signals, 52 available GPIOs, bus connectors for DSP-FPGA data interaction through the DSP EMIF bus, hardware protection scheme for the input signals, and ten fibre optic transmitters mainly utilised for the PWM. Figure 8.3 (a) illustrates one of the FPGA boards.

For the specific M3C implementation, an interruption signal for the DSP, a Watchdog timer, 42 ADC conversion channels, and 55 fibre optic gating pulses are the required peripherals for the implementation. The main (master) FPGA generates the interrupt signal for the DSP, and defines the gating pulses for the power-cells by using a single-edge PWM scheme for each leg. The two remaining FPGA boards are mainly used for ADC measurements, where an extra ADC daughter board, shown in Figure 8.3 (b), is connected to the second daughter FPGA. Additionally, the fibre optic emitters are located in another daughter board directly connected to the master FPGA board (see Figure 8.3 (c)). The watchdog timer allows an uninterrupted real-time communication between the DSP and the FPGAs during the processing period; additionally, a protection scheme is set by conditioning the firing pulses when the communication is lost.

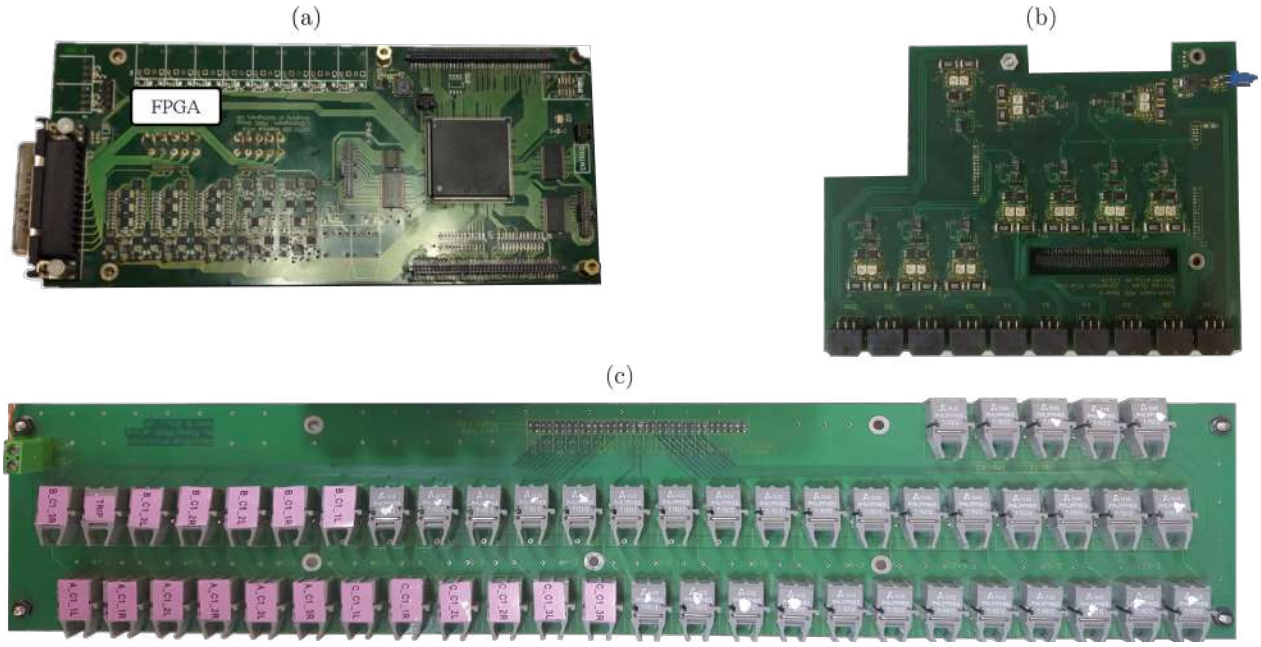

Figure 8.3: (a) PEMC FPGA board (b) ADC board (c) fibre optic board.

8.1.3. Power Stage

The power stage comprises a M3C converter of 27 full-bridge modules and two programmable sources connected to the input/output ports through inductances. The M3C prototype and the programmable power sources are shown in Figure 8.4 and 8.5, respectively. For the M3C, each power cell consists of two double-MOSFET modules IRFP4868PBF, rated for a nominal voltage of 300V and a nominal current of 70A.

The parameters of the system are depicted in Table 8.2, where, at input port rst, an Ametek Programmable Power Source Model CSW5550 is connected in series with series inductors of L_{rst}=5mH, whereas at output port uvw another Ametek Programmable Power Source Model MX45 is utilized with L_{uvw}=2,5mH filters. This values were used according to the availability in the laboratory.

Table 8.2: Parameters of the experimental prototype.

Equipment	Parameters	Experimental Prototype
M3C	Modules	27
	Nominal Power	6kVA
	Arm-Inductance	2.5mH
	Cell Capacitance	4.7mF
	Nominal DC Voltage	200V
rts-port Programmable Source	Model	AMETEK CSW5550
	Nominal Power	5.55kVA
	Output Voltage	0-540$V_{LL\text{-}rms}$
	Output Frequency	40-5000HZ
	Line Output Inductance	5mH
uvw-port Programmable Source	Model	AMETEK MX45
	Nominal Power	53kVA
	Output Voltage	0-480$V_{LL\text{-}rms}$
	Output Frequency	16-905Hz
	Line Output Inductance	2.5mH

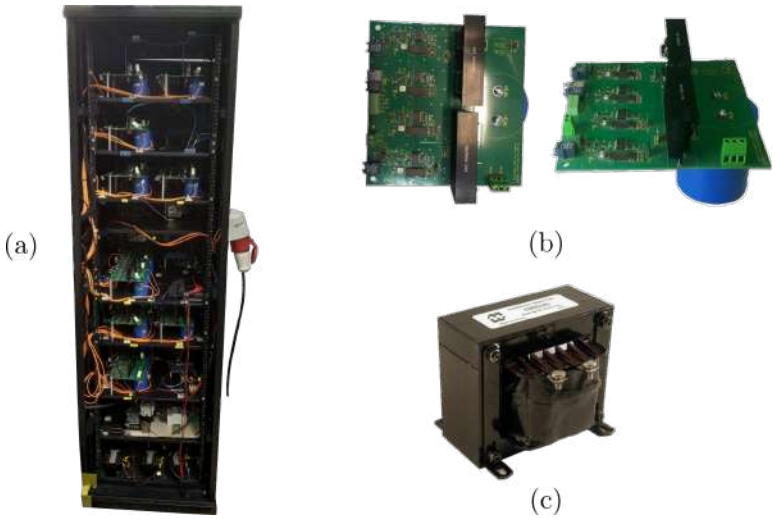

Figure 8.4: M3C experimental prototype. (a) Overall view of the M3C (b) top and lateral-perspective view of H-Bridge power cell. (c) Hammond arm inductance [2.5mH].

(a)  (b) 

Figure 8.5: Programmable power sources. (a)Ametek CSW5500 (b)Ametek MX45 Regenerative Source.

8.2. CCV Balancing Scheme Based on CCS-MPC

With the experimental prototype previously described, several tests were performed. Although the validation of the proposed scheme is fully implemented in the simulation results, due to computational burden limitation of the control platform, the experimental validation was realised with two different approaches. The first approach is the validation of the Stored Energy Balancing MPC scheme, but with P-controllers for regulating the circulating currents. Conversely, the second approach is the implementation of the circulating current control based on MPC, where the regulation of the CCVs is achieved through a traditional control scheme with linear controllers.

To validate the CCS-MPC scheme described in section 6.1 , the scheme shown in Figure 8.6 was implemented in the control platform. As depicted, the implemented scheme is the same as shown in Figure 7.1, but the circulating current MPC control is replaced by proportional controllers. This adjustment reduces the computational burden to a feasible value in the used control platform. Table 8.3 provides the parameters of the controllers, where the sampling period is $160\mu s$. The rst grid input frequency is fixed at 50Hz, and the uvw load port is also connected to a balanced grid, but with variable amplitude and frequency.

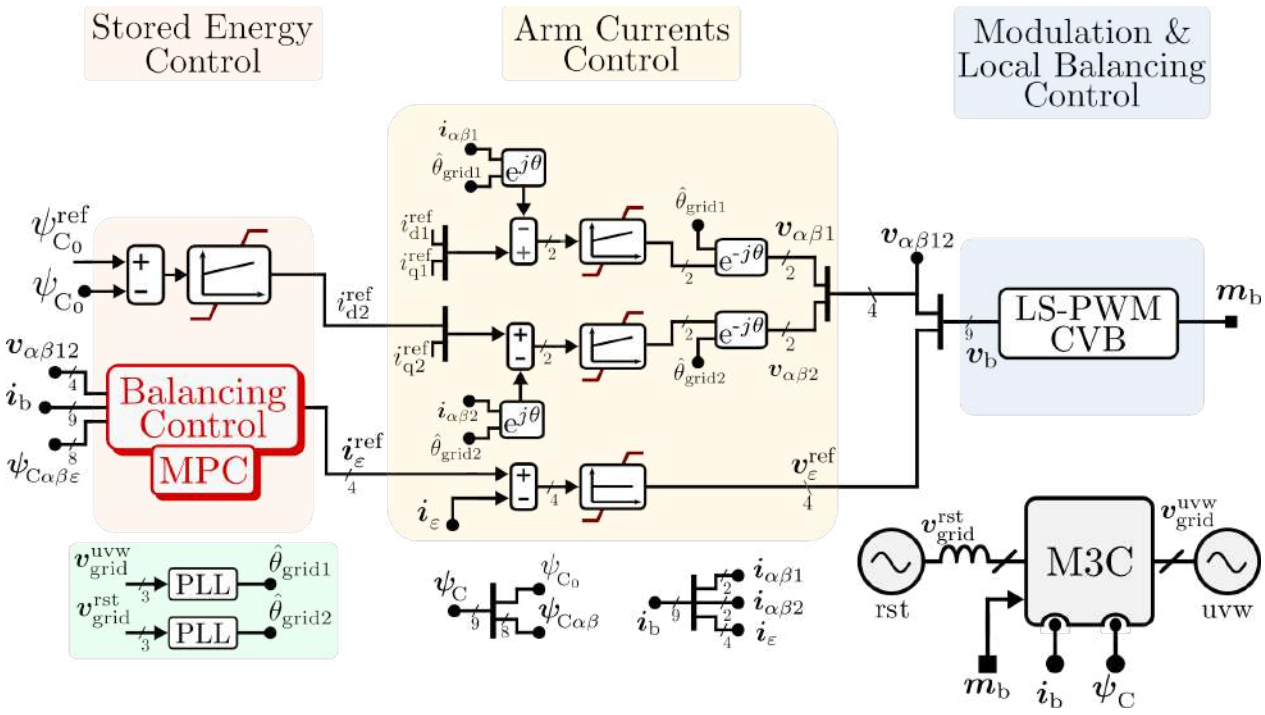

Figure 8.6: Control scheme for stored energy control based on CCS-MPC used in experimental validation.

Table 8.3: Controllers parameters for experimental validation of Stored Energy Control based on CCS-MPC.

Controller Parameters		
Sampling/Carrier Period	T_s	$160\mu s$
uvw-port Current Control	BW - ξ	166Hz - 0.756
rts-port Current Control	BW - ξ	230Hz- 0.938
Circulating Currents Control	BW - ξ	111Hz - 0.999
Total Stored Energy Control	BW - ξ	2.4Hz - 0.6
CCS-MPC (DFM)	r_ε - $q_{\varepsilon 12}$	1e5 - 5
CCS-MPC (EFM)	r_ε - $q_{\varepsilon 12}$	1e5 - 75
Common-mode Voltage	CMV-V_o	93V - 279V

8.2.1. Steady Operation Performance

Operation at Near Input Port Frequency

In this test, the grid frequency of the uvw port is set to 49.5Hz with positive sequence. The performance, considering three different values of the parameter $q_{\varepsilon 34} \in \{5, 75, 150\}$ is experimentally obtained. The output-port power references are 2.67kW and 446VAr, with the input port being operated at unity power factor. The CCVs, Transformed CCVs (T-CCVs), circulating currents and arm currents for each $q_{\varepsilon 34}$ value are depicted in Fig. 8.7. Scope shots are shown in Fig. 8.8.

As depicted in Fig. 8.7, when $q_{\varepsilon 34} > 5$, lower oscillation amplitudes in the CCVs and T-CCVs are observed, but with an increment in the magnitude of the circulating currents. Although this attractive feature enables a simple regulation of the CCV mitigation, after reaching a given $q_{\varepsilon 34}$ gain level there is not a substantial difference in the CCV oscillation amplitudes. This is concluded by comparing the results obtained with $q_{\varepsilon 34}$=75 and $q_{\varepsilon 34}$=150 in Fig. 8.7, where the CCV peak to peak values are similar, but with an increment of $\pm$1A in the circulating current amplitudes in the latter case.

In Fig. 8.8(a), oscilloscope traces of the port/arm currents and capacitor/output voltages are shown. The input and output currents have no noticeable distortion and they are not affected by the circulating currents. Fig. 8.8(b) shows that the capacitor voltages are well regulated without large low frequency oscillations.

Unless otherwise stated, in the rest of the experimental work of Section 8.2, the value of $q_{\varepsilon 34} = 75$ is assumed

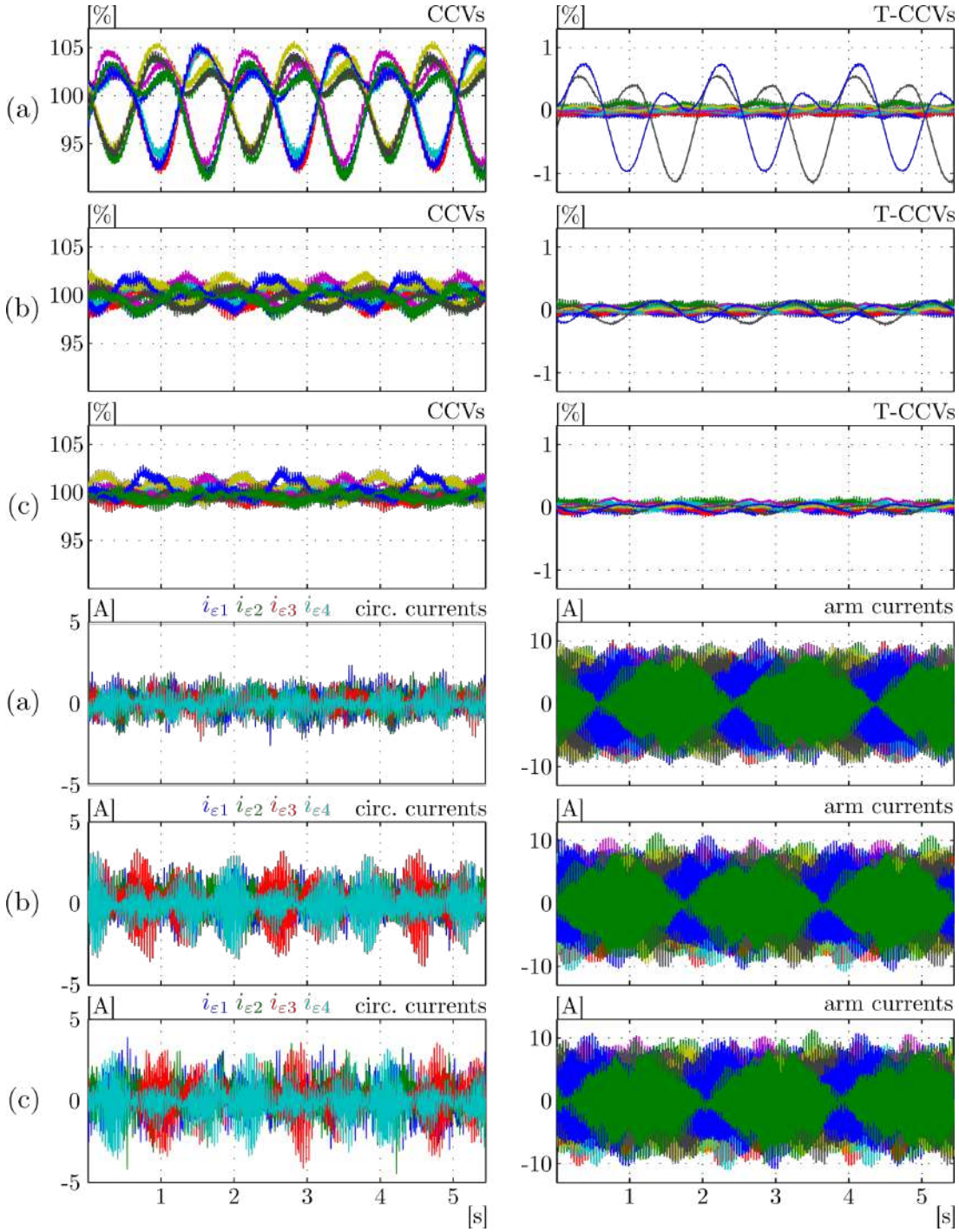

Figure 8.7: Steady operation of the converter with output port grid frequency of 49.5Hz at different MPC weight values. (a) q_{M}=5, (b) q_{M}=75, and (c) q_{M}=150.

Steady Operation at 50Hz

In this case, the output *uvw* port frequency is set at 50Hz (i.e. ω_1=ω_2). The power references at both ports have the same values as those used in the previous section. The results obtained for this test are shown in Fig. 8.9 and Fig. 8.10. The CCVs, T-CCVs, circulating currents and arm currents plots are shown in these graphics.

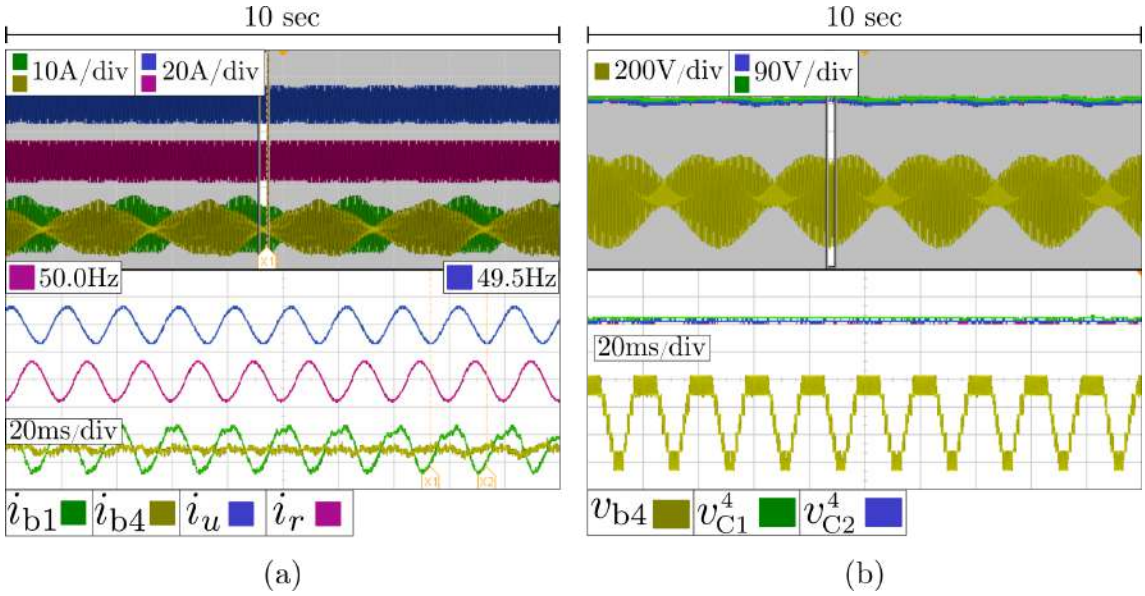

Figure 8.8: Experimental results with constant power demand at 49.5Hz in the output port.(a) Arm currents i_{b1}, i_{b4} with input/ output currents i_r and i_u. (b) Cluster output voltage v_{b4} with capacitor voltages v_{C1}^4 and v_{C2}^4.

As depicted in the CCVs and T-CCVs (see Fig. 8.9) , a steady state DC error is produced. This deviation is due to the inherent behaviour of strategies based on CCS-MPC, where no integrator is implemented by the control law [91]. Notwithstanding this drawback, the DC error is only 2 % and it is considered negligible. It is worth mentioning that this error can be further reduced by increasing the gain $q_{\varepsilon 34}$; however, as concluded from the results shown in Fig. 8.9(b)-(c), there is a trade-off between the reduction of the CCV errors and the amplitude of the circulating current magnitudes.

In Fig. 8.10(a), the arm currents i_{b1} and i_{b4} as well as the input/output currents i_r and i_u are shown; additionally, the output cluster voltage v_{b4}, the capacitor voltages v_{C1}^4 and v_{C2}^4 are shown in Fig. 8.10(b). The waveforms depicted confirm the good performance of the strategy. The arm and port currents, together with the capacitor voltages maintain stable and well regulated values during the whole 10-second period, even though this is a critical operating point producing instability if uncompensated (see Table 3.1). Using the proposed CCS-MPC, the large low frequency oscillations in $\psi_{C_{\varepsilon 3}}$ and $\psi_{C_{\varepsilon 4}}$ are avoided due to the MPC algorithm [see (6.8)], where the computed circulating currents are automatically defined with a straightforward procedure.

8.2.2. Dynamic Performance of the Strategy

Variable Output port Frequency at Constant Power Demand

In this test, the *uvw* port power is set to 2.67kW and 446VAr and the corresponding frequency is changed continuously with the following pattern (see Fig. 8.11): initially, the output grid frequency is 45Hz before it increases with a constant slope of 3.5Hz/sec to 52Hz

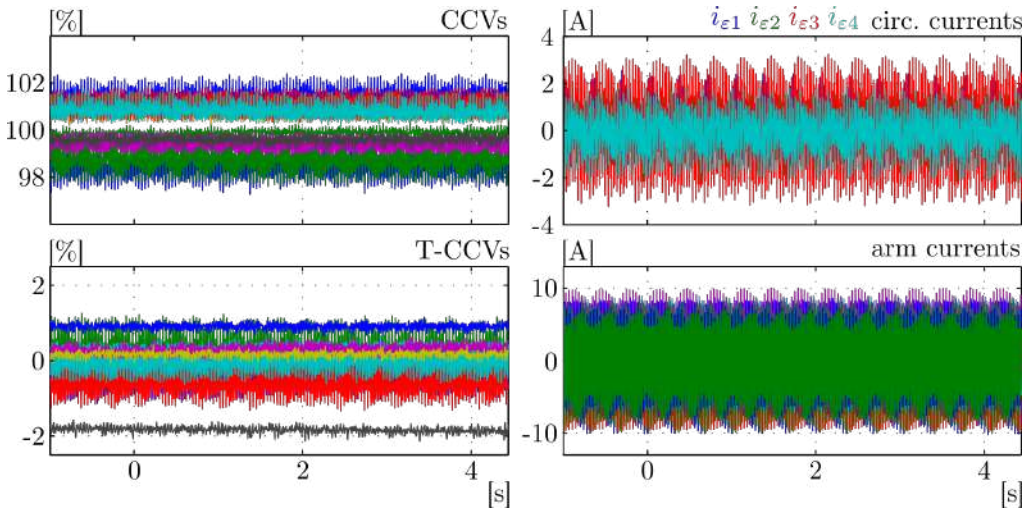

Figure 8.9: Steady operation of the converter with output port grid frequency of 50Hz with q_{M}=75.

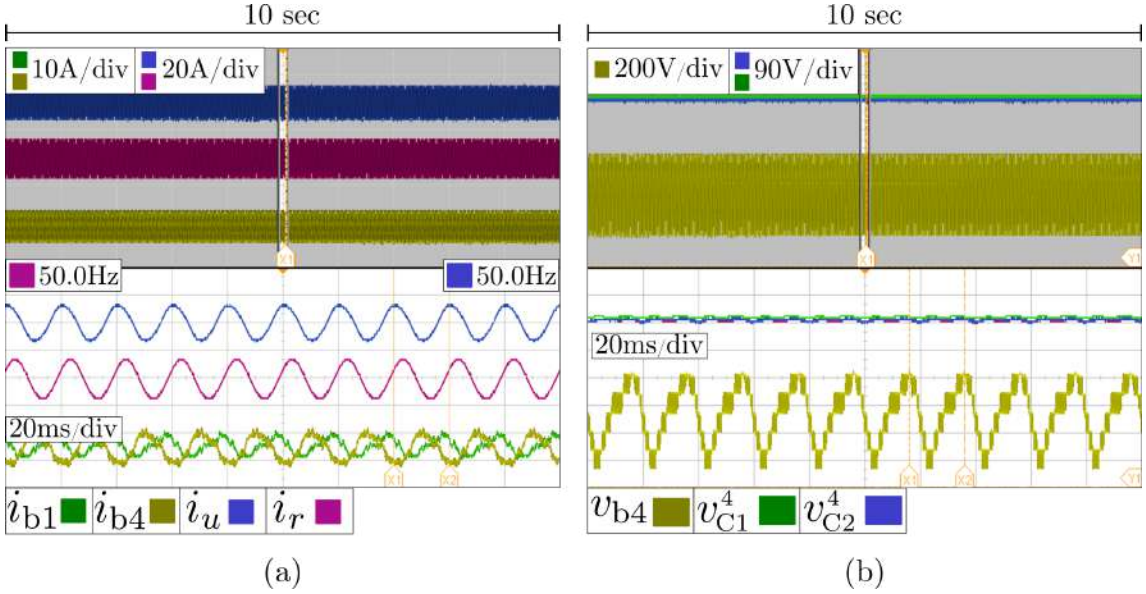

Figure 8.10: Experimental results with constant power demand at 50Hz in the output port.(a) Arm currents $\mathrm{i_{b1}}$, $\mathrm{i_{b4}}$ with input/ output currents i_r and i_u. (b) Cluster output voltage v_{b4} with capacitor voltages v_{C1}^4 and v_{C2}^4.

where it remains for one second. Subsequently, it decreases to 49.5Hz at a 2.5Hz/sec rate. The experimental results are depicted in Fig. 8.11 and Fig. 8.12.

In Fig. 8.11, the CCVs, T-CCVs, grid frequencies ω_1 and ω_2, dq-axis input/output port currents, output cluster voltages and arm-currents are shown; additionally, the CCVs and T-CVVs are illustrated in per unit with a base of 400V. As illustrated in the behaviour of CCVs and T-CCVs, the oscillations in the capacitor voltages reach ripple magnitudes of only 3 % of the nominal voltage. Moreover, the dq-axis input/output port currents are kept relatively constant during the entire test, and do not suffer significant disturbances. As

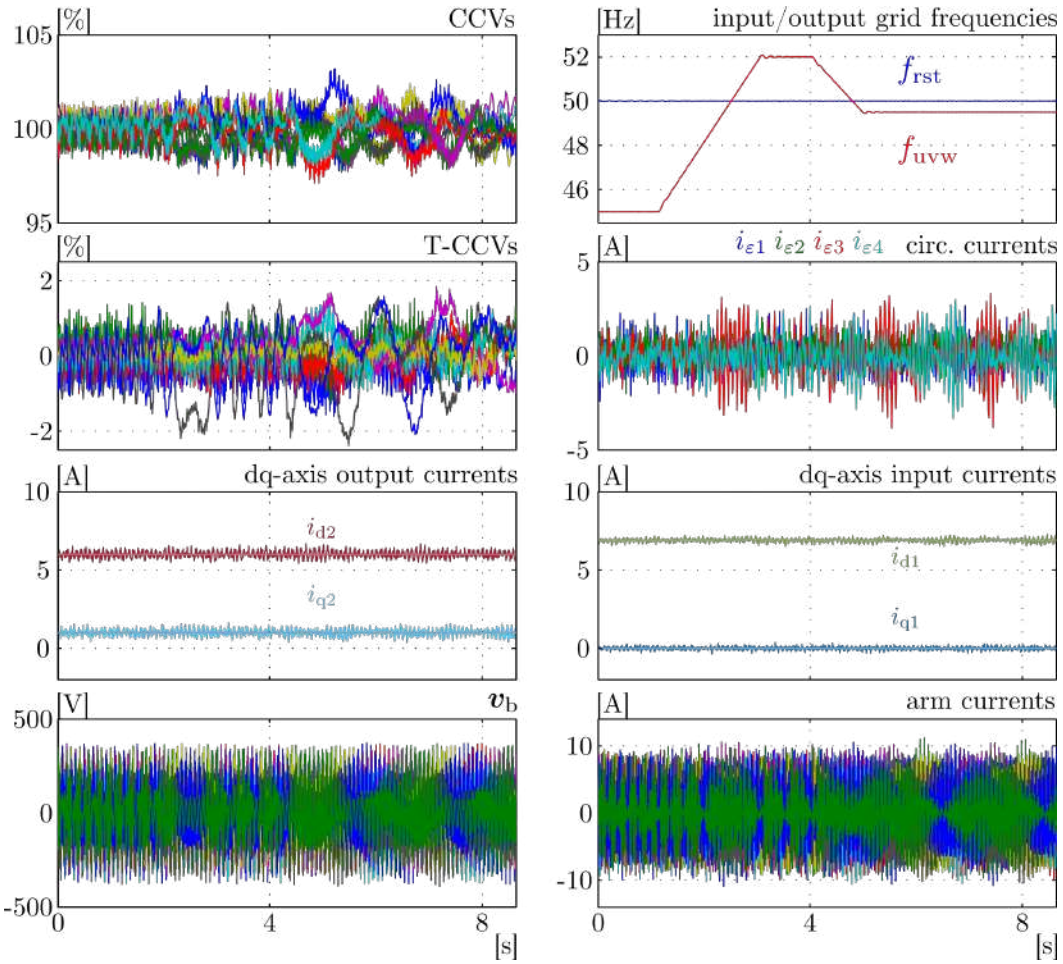

Figure 8.11: Experimental results of variable output frequency with constant power demand. CCVs and Transformed CVVs (T-CCVs) are shown in per unit with basis 400V.

expected, the injected circulating currents increase as the output port frequency approaches 50Hz operation (i.e. EFM), but the additional arm current amplitude compared to 45Hz operation is small.

In Fig. 8.12 (a)-(c), the arm currents $\mathrm{i_{b1}}$ and $\mathrm{i_{b4}}$ with input/output currents i_r and i_u are shown when the M^3C is operating with output frequencies of 45Hz, 52Hz and 49.5Hz respectively. Additionally, in Fig. 8.12 (d), the output cluster voltage v_{b4} with the capacitor voltages v^4_{C1} and v^4_{C2} are shown. Notice that for the results shown in Fig. 8.12, the port currents at either side have no additional distortion and the high frequency components of the circulating currents are not present at either port.

In general, the behaviour of all system variables is stable during the whole test, with higher current demand during near input frequency operation. Moreover, further modifications to the control law of (6.8), when entering EFM, are not required, due to the automatic adjustment of the output signals.

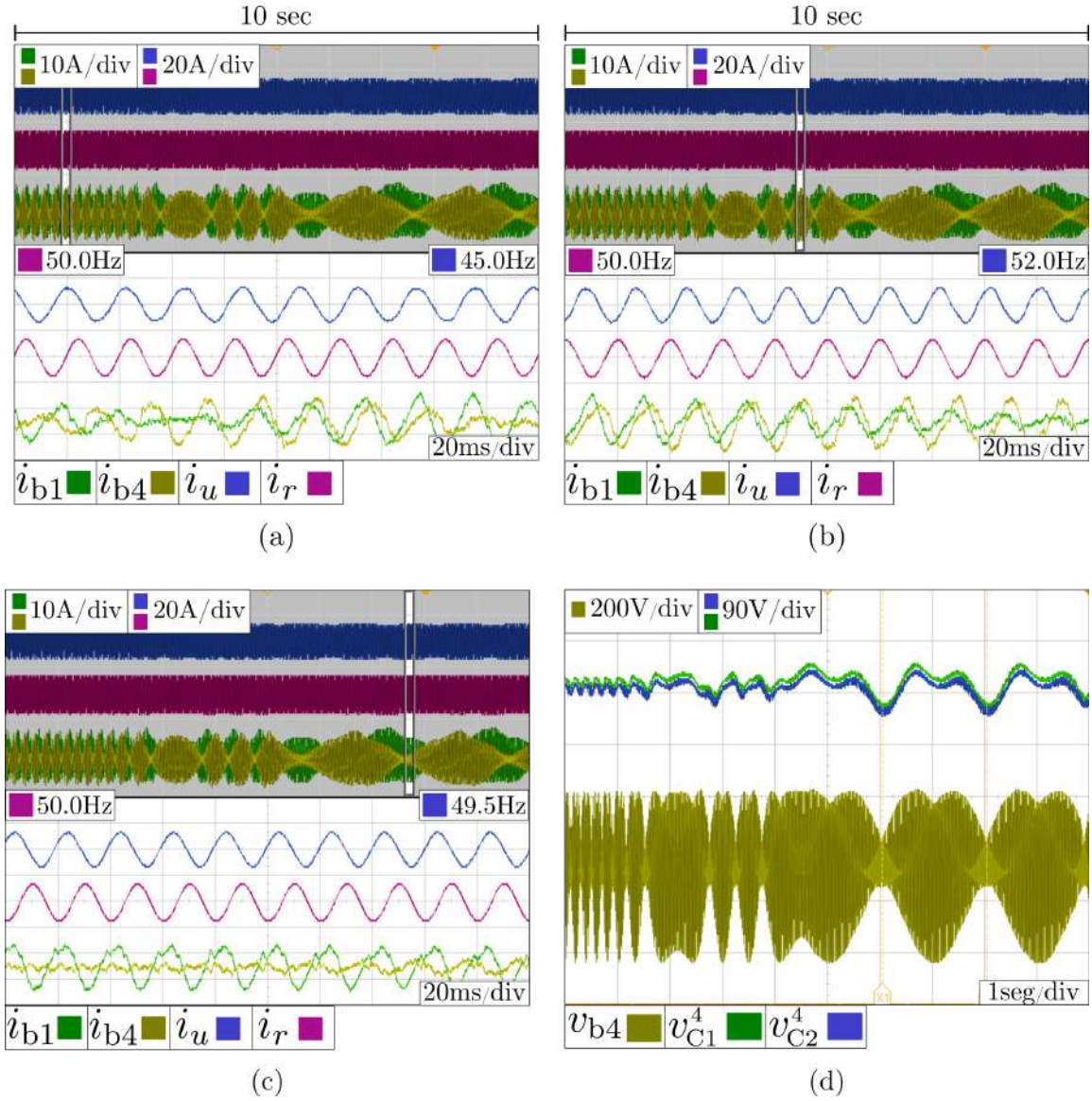

Figure 8.12: Experimental results of variable output frequency with constant power demand. Arm currents i_{b1}, i_{b4} with input/ output currents i_r and i_u are shown at specific operating frequencies (a)45HZ, (b)52HZ, (c)49.5HZ. Cluster output voltage v_{b4} with capacitor voltages v^4_{C1} and v^4_{C2} are shown in (d).

Sudden reversal in Reactive Power Demand

In order to induce a critical operating point, the output port grid frequency is set to 49.9Hz and its power reference is set to 0kW/2.67kVAr. As described in Section 3.3.1, the low-frequency CCVs oscillations during EFM are completely defined by the reactive power injection Q_2. The weight cost $q_{\varepsilon 34}$ is set with the same values defined in section 8.2.2.

With this operating condition, at 0 seconds a sudden change in the output port power demand to 0kW/-2.67kVAr is set, which induces a 180° phase change in the power oscillations that induce low-frequency components in the affected T-SSCV pair. The results are shown in Fig. 8.13, where the CCVs, T-CCVs, dq-axis input currents, dq-axis output currents,

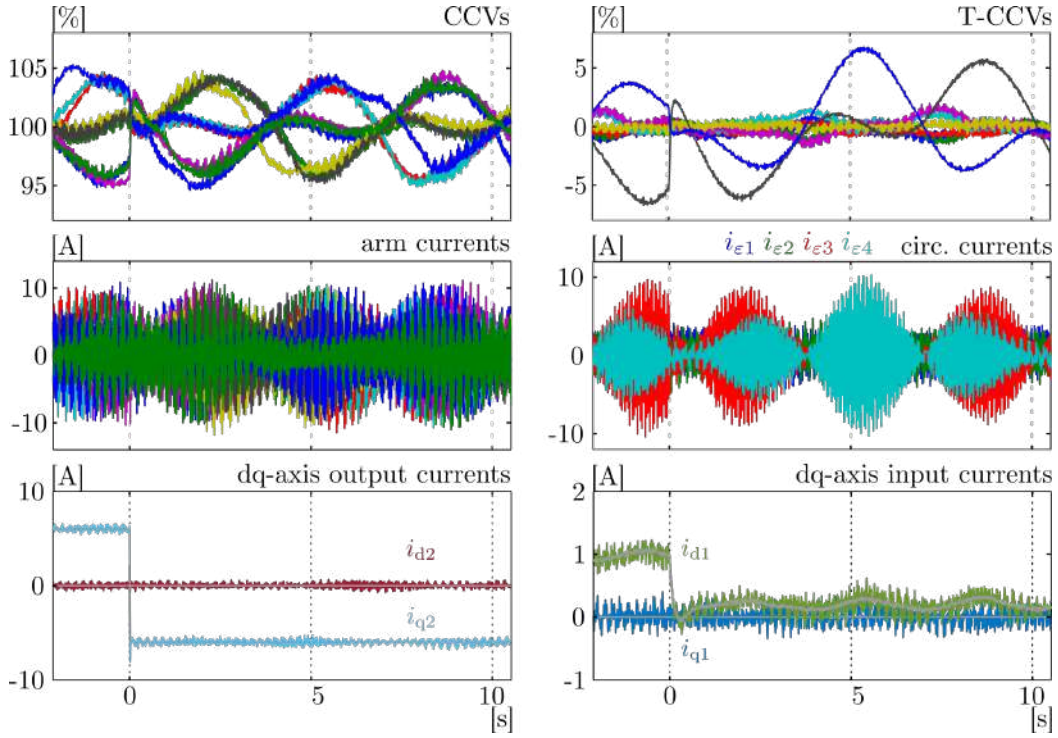

Figure 8.13: Experimental results of a sudden reversal in reactive power demand with 49.9Hz in the output port grid.

circulating currents and arm currents are depicted.

As illustrated in Fig. 8.13, the low-frequency oscillations are mainly generated by the reactive power in the load side. Moreover, the sudden change implies an instant sign reversal of the voltage oscillations related to the $\{\psi_{C_{\varepsilon 3}},\ \psi_{C_{\varepsilon 4}}\}$ terms. As expected, prior to the sudden change in the power demand, the CCVs are balanced with a low frequency oscillation around 5 %, which is related to the unfavourable critical operation point. As shown in the CCVs and T-CCVs the change in the oscillation phase angles is automatic and no transient increment of the CVVs oscillation amplitudes are identified. This test shows the favourable response of the proposed strategy, even during critical operating circumstances, with a fast and stable performance.

8.3. Circulating Current Control Based on CCS-MPC

As explained at the beginning of this chapter, validation of the CCS-MPC control for the circulating currents is done without considering the MPC scheme proposed for the CCV Balancing.

Specifically, the implemented control scheme is illustrated in Figure 8.14, where the main difference with the scheme presented in Figure 7.1 is that the stored energy balancing is replaced by a vector control scheme inspired by that proposed in Figure 4.4 [21]. Additionally, the control system design is focused only on DFM operation [21], which implies that mitigation of very large low-frequency oscillations of the capacitor voltages is not required.

The DSP sample-time and PWM-carrier period are set to T_s=320μs, the DC-voltage reference for all modules is 127V, the arm currents limit is $I_{\max}$=12A, and the line-voltage/frequency of the grid connected at rst-input port is 182V/50Hz (AMETEK CSW5550). The parameters of the controllers of the M3C are shown in Table 8.4.

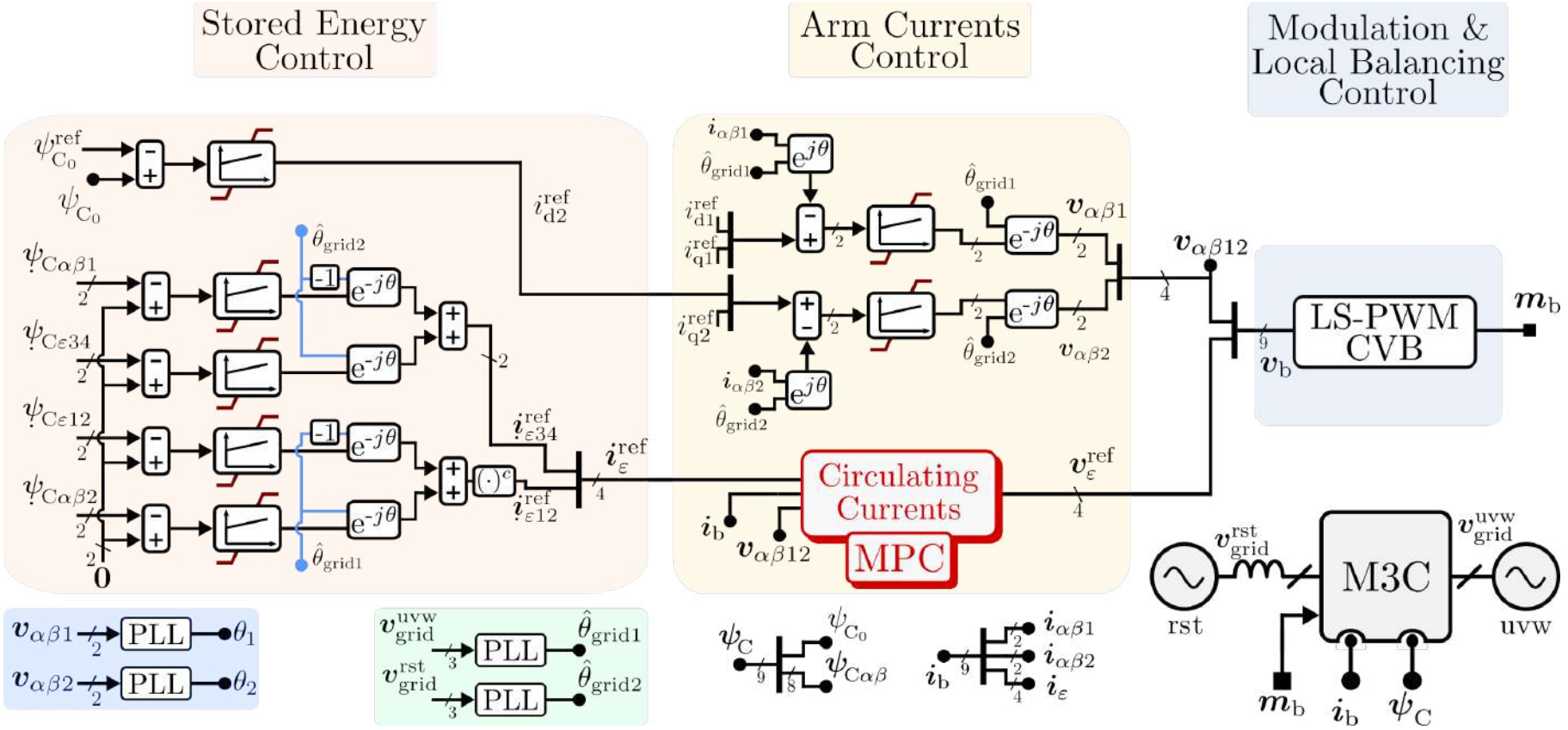

Figure 8.14: Control scheme for circulating current control based on CCS-MPC used in experimental set-up.

Table 8.4: Controller parameters for experimental validation of Circulating Current Control based on CCS-MPC.

Controller Parameters		
Sampling/Carrier Period	T_s	$320\mu s$
uvw-port Current Control	BW - ξ	165Hz - 0.99
rts-port Current Control	BW - ξ	253Hz- 0.99
Circulating Currents Control	BW - ξ	268Hz - 0.99
CCS-MPC	r_ε - q_ε	10 - 1
Total Stored Energy Control	BW - ξ	6.5Hz - 0.99
CVV Balancing Energy Control	BW - ξ	5.58Hz - 0.99

8.3.1. Performance of the MPC strategy Considering Variable Voltage and Frequency in Output Port.

To show the performance of the MPC scheme at different output frequencies, the voltage and frequency of the programmable power source at the uvw port was programmed for a ramp variation from 182V/45Hz to 90V/20Hz and vice versa in $\approx$ 1.25s. For the whole of this test the d-q axis current references uvw are set to 1A and 5A respectively. At the rst-input port, the q-axis reference is also constant at -5A whereas the d-axis reference is defined by the Total Stored Energy Control system. The experimental results for this test are shown in Figure. 8.15 and Figure 8.16.

The two plots related to the left-side column of Figure 8.15 illustrate the instantaneous grid voltages at the uvw port, where the amplitude variation can be identified; additionally, the upper plot in the middle column shows the grid-frequency of both the uvw and rst ports. The left and middle graphics of the second row show the peak grid voltages for both ports and the Cluster Capacitor Voltages (CCVs). The graphics of the right-side column depict the dq-axis currents of the uvw and rst ports, respectively. From these experimental results it is concluded that the dq-axis uvw output currents follow their respective references with negligible tracking error, while the d-axis reference at the rst-input port changes according to the active power specified by the Total Stored Energy Control. Notice that in this test the power at the port uvw is not constant because the uvw voltage varies between 182V to 90V with constant d-axis current reference. As shown in the CCVs plot, this dynamic variation produces small low frequency oscillations in the capacitor voltages.

Additional results corresponding to this experimental test are shown in the scope waveforms illustrated in Fig. 8.16. The steady state performance at 20Hz is shown in Fig. 8.16(a) and at 45Hz in Fig. 8.16(b). Notice that the system is stable with low distortion in the input and output current waveforms. The input/output currents i_r, i_u, and arm currents i_{b1}, i_{b4} are also shown in Fig. 8.16.

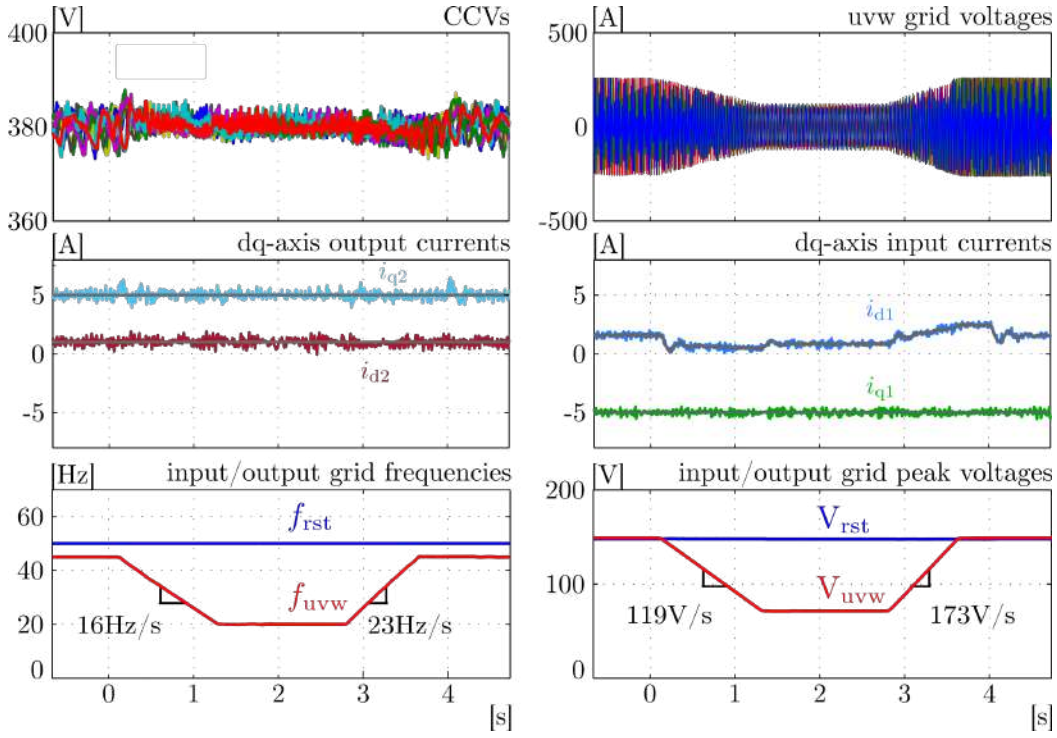

Figure 8.15: Experimental results of the proposed MPC strategy with cyclic variations on voltage/frequency at the uvw-port power source.

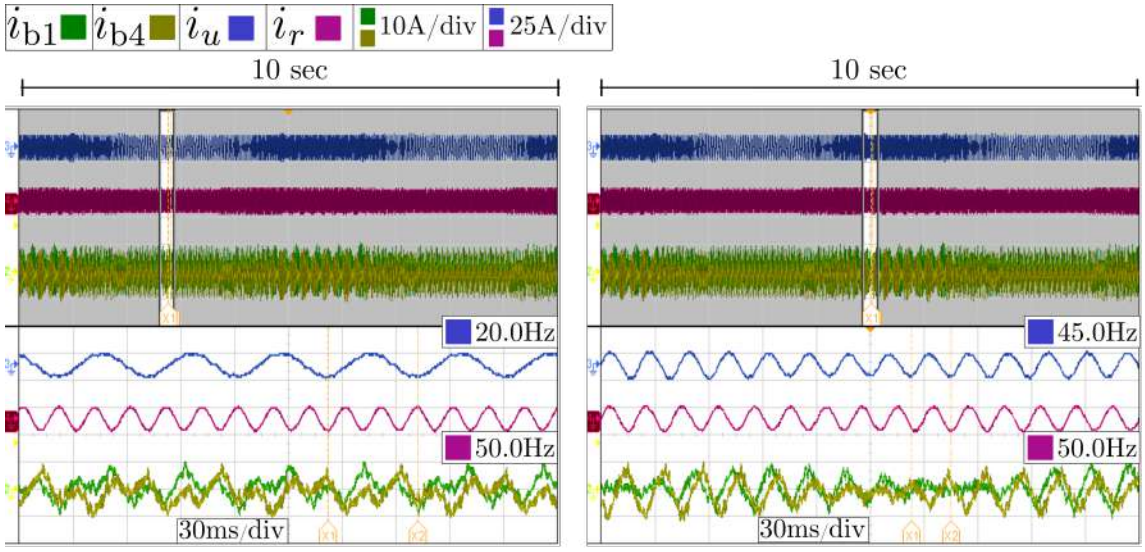

Figure 8.16: Experimental results of output and arm currents of the M3C at different voltage/frequency values at the uvw-grid. (a)Operation at 20Hz, and (b) Operation at 45Hz.

8.3.2. Comparison of Performance Achieved by the Proposed Saturation Schemes.

The experimental test used in this sub-section is designed to demand high magnitudes of circulating currents that exceed a predetermined arm-current limit. This allows experimental

verification of the saturation schemes discussed in Section 6.2.

In order to compare the performance of the saturation scheme-A and -B, a TBT (described in Section 7.2.4) is performed with the power source at the rst side set to 182V/50Hz, and the uvw power source set to 182V/25Hz. Balancing of the CCVs starts at t_{ON}=0s, followed by a transient at t_Q=20ms when the q-axis reference is stepped from 1A to 4A (445VAr to 1782VAr) at the uvw side, and from -1A to -4A (-445VAr to -1782VAr) at the rst side. The d-axis uvw current reference is set at 6A (2670W).The results of this test for the strategy without saturation, and for Scheme-A and Scheme-B (considering $I_{\max} = 12$A) are shown in Figures 8.17 to 8.20.

As shown in Figure 8.17 (a), when no saturation scheme is used, the arm currents reach peak values near 20A and exceed the defined ±12A limits several times. The input/output port currents are unaffected during the balancing of the CCVs, which lasts around 95ms. On the other hand, as shown in Figure 8.17 (b)-(c), the arm peak currents are limited with saturation scheme-A, but there still are a couple of short-duration current peaks close to 17A. In scheme-B the arm currents are mostly inside the predefined limits, with few undesirable spikes that surpass the ± 12A band, reaching a maximum value of ≈ 14A. Notice that the circulating currents have some high-frequency oscillating components which are produced by a combination of switching ripple and the fast dynamic response typically achieved by the predictive control algorithms. However, these oscillations in the circulating currents are not reflected in either the uvw or in the rst output port currents because the proposed CCS-MPC maintains even the fast oscillations of the circulating currents within the defined constraints.

As depicted in Figure 8.17 (c), scheme-B exhibits better arm current saturation performance than that achieved by scheme-A, maintaining the arm currents mostly inside the predefined band. In comparison with the unconstrained results shown in Figure 8.17 (a), CCV imbalance is corrected more rapidly when the non-saturation scheme is applied, but this is achieved by increasing the arm currents above the predefined limits. The step changes in the active and reactive dq-currents at the rst-input and uvw-output ports are also shown in Figure 8.17. According to the experimental results, the proposed saturation scheme included in the control strategy does not affect the dynamic or steady state performance of the input/output port currents, confirming that decoupled operation is achieved.

As shown in Figure 8.18, the number of activated constraints during the test for scheme-A and -B differ considerably. For scheme-A, there is mainly one active constraint for most of the transient, but there are some instances during the test where two constraints are activated simultaneously. Analysing the experimental data it is concluded that this occurs when both the upper and the lower current limits are reached in some of the arms. On the other hand, for scheme-B, there are more instances when two constraints are active in comparison with scheme-A. Even more, up to three arm-current constraints are activated simultaneously at a specific instant, achieving a better limitation of the arms currents than that obtained by scheme-A.

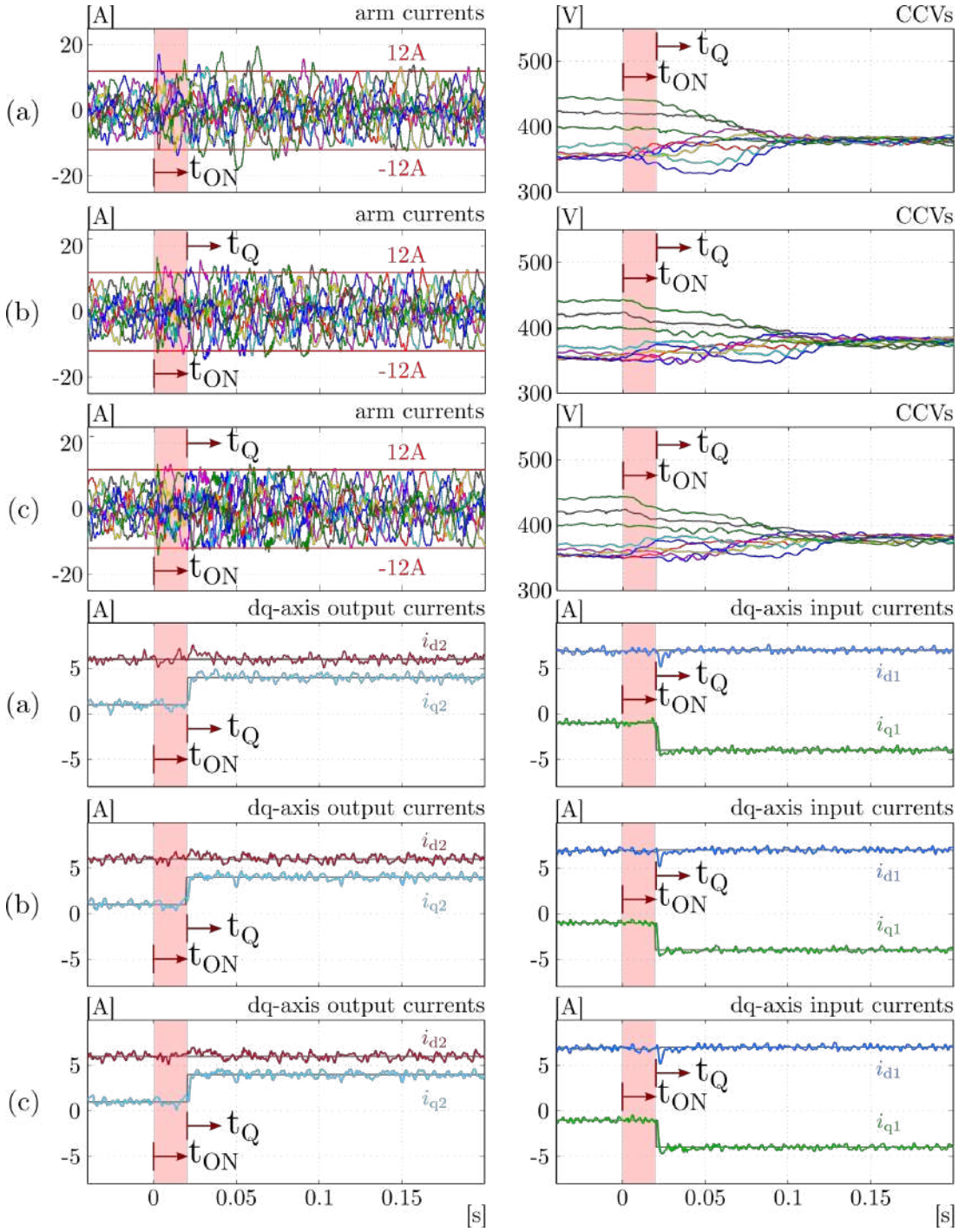

Figure 8.17: Experimental results for (a)Disabled Saturation (b)Saturation Scheme-A and (c)Saturation Scheme-B during TBT.

In Figure 8.20, the currents in the ports uvw and rst are shown, as well as two arm currents i_{b1} and i_{b4}. Figures (a), (b) and (c) show the experimental results for the no saturation scheme, saturation scheme-A and saturation scheme-B respectively. For all the schemes it is concluded that the output currents are not affected by the large changes in the circulating currents (after t_{ON}) confirming that the operation of the proposed M3C control system achieves decoupled operation.

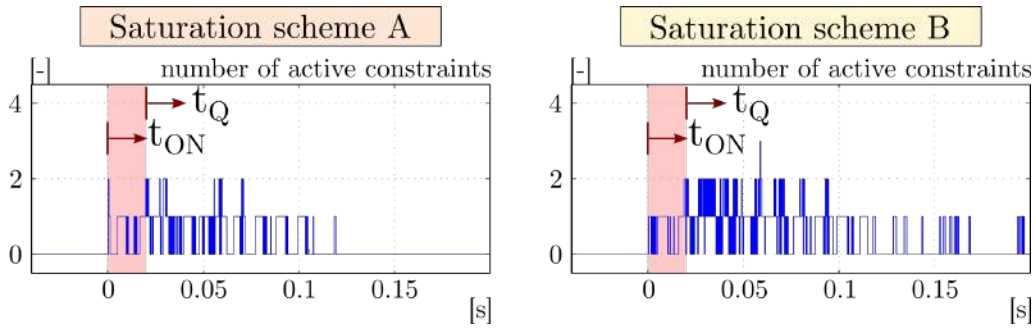

Figure 8.18: Number of active constraints for Saturation Scheme-A and Saturation Scheme-B during experimental TBT.

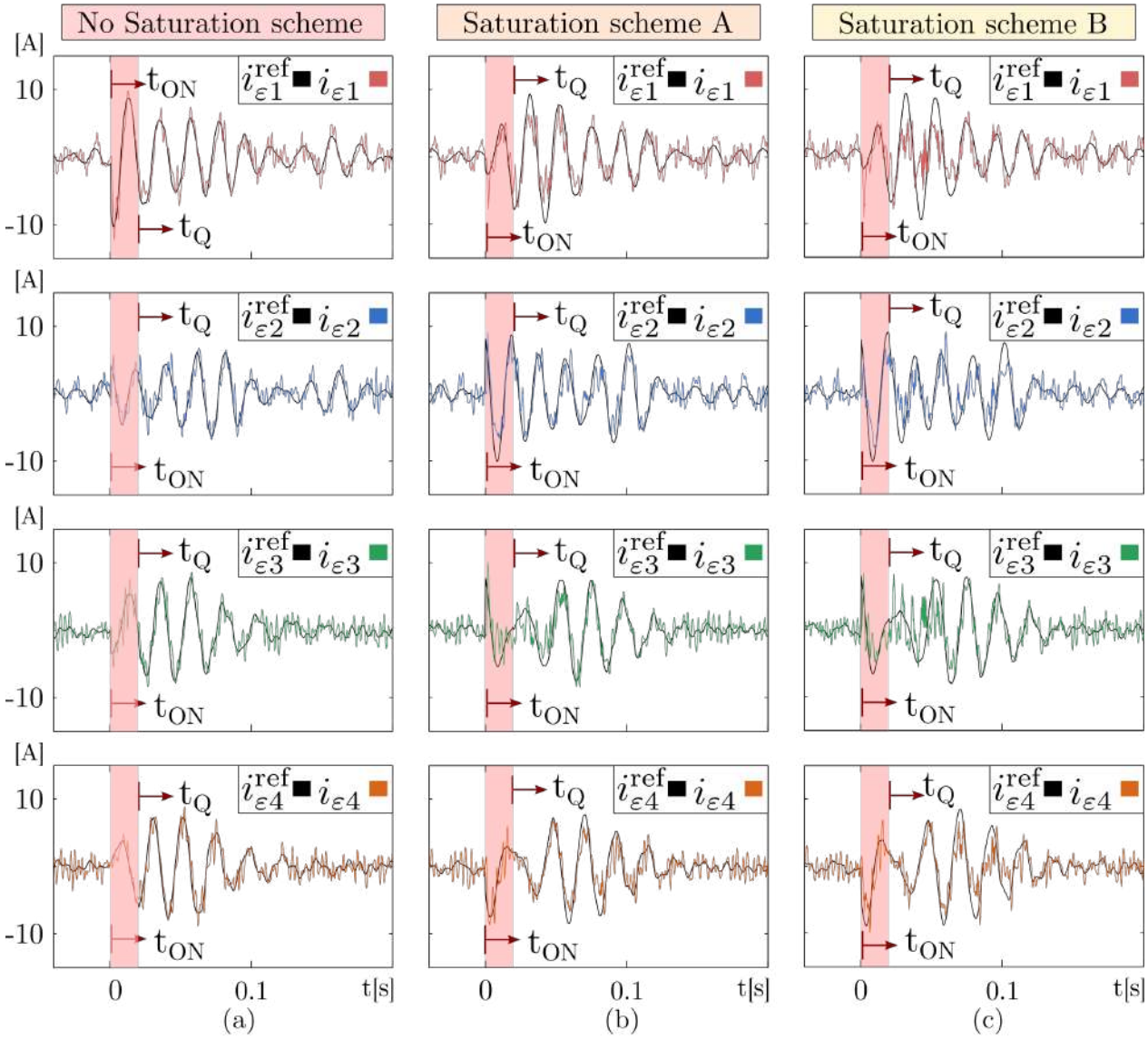

Figure 8.19: Experimental results of circulating currents with their respective references during Dynamic test. (a) MPC without Saturation, (b) Scheme-A and Scheme-B.

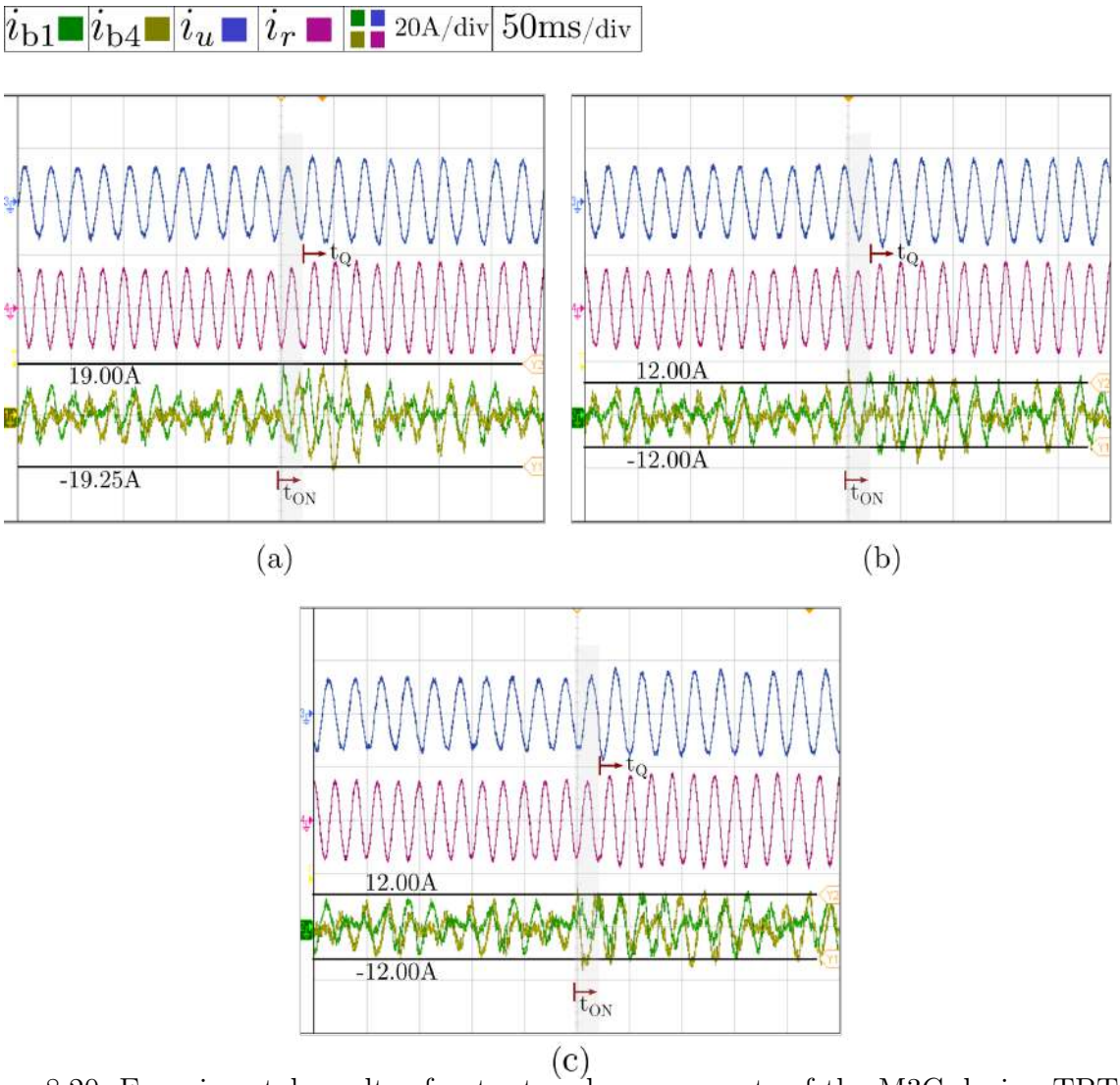

Figure 8.20: Experimental results of output and arm currents of the M3C during TBT. (a) MPC strategy without saturation scheme, (b) MPC strategy with saturation scheme-A and (c) MPC strategy with saturation scheme-B.

In Figure 8.19 the four circulating currents are shown for the three saturation schemes studied in this work. As shown in the plots, the tracking performance is better for the non-saturated case because the control algorithm does not consider the constrains to limit the circulating currents.

As shown in Figure 8.19 (b)-(c), the effects of the proposed saturation algorithms are clearly shown in the circulating current waveforms. Although relatively high-frequency oscillations are produced when the saturation scheme is activated, these values are not necessarily reflected in the arm currents in the natural coordinate domain. To reinforce this idea, notice that the tracking of the circulating currents is worst when the saturation scheme-B is used, which has better saturation performance than scheme-A. This behaviour is inherent in the MPC algorithm, because there is a trade-off between good tracking of the circulating current references and proper limitation when the maximum set values are reached by the

arm currents.

8.4. Chapter Summary

This chapter exhibits the experimental validation of the proposed CCS-MPC control. The results are divided into the CCV balancing scheme and the circulating current control scheme validation. In the former stage, steady-state results during EFM exhibit the scheme's stable and good performance. Moreover, two dynamic tests show the outstanding behaviour of the system in EFM, even during high disturbances induced by the output port. For the circulating current control, transient results in DFM highlight the scheme's benefits. A dynamic ramp test exhibits the good behaviour of the scheme when no saturation is required. Afterwards, MPC scheme-A, scheme-B and no saturation are compared for a TBT case with sudden input/output port current injection. The differences between scheme-A and scheme-B are relevant for the analysed case, where using the input/output port dynamic models improves the saturation performance.

Chapter 9

Summary and Conclusions

In the presented work a control scheme based on CCS-MPC is introduced. As initially stated, to the best of the author's knowledge, in the available literature there is not a publication with the same presented approach.

The presented scheme aims to balance the stored energy in the M3C, where the system inputs are the transformed CCVs, and the outputs are circulating voltages of the M3C. The strategy is defined into two cascaded stages: initially a CCVs regulation is done and, afterwards, the circulating current control is run. Both stages are based on a CCS-MPC formulation.

Due to capability limitations of the control platform used, the presented experimental validation was performed separately. In general, the performance of the proposed scheme shows successful simulation and experimental results, with attractive features.

Cluster Capacitor Voltages MPC stage

In this stage, the proposed CCS-MPC is based on a unconstrained quadratic programming problem, where its analytical solution is obtained. This analytical solution can be reinterpreted as MIMO gain control system with a feed-forward term and time variant gain. The output signals of the proposed scheme are the reference of the circulating currents of the M3C.

An important and attractive feature of this strategy is that it can be used for near input frequency operation without any additional complexity or modifications to the control law obtained. An additional advantage of the controller, when compared with the published approaches based on linear controllers, is that it automatically adjusts the waveform shape, magnitude and phase of the circulating current required to regulate the energies at the critical operating points when the port frequencies are similar or equal. Therefore, it is not necessary to predefine the parameters of the circulating currents (eg. shape, frequency, phase,etc.) for

mitigation purposes in the control algorithm.

Using the CCS-MPC, during DFM (or EFM) it is neither necessary to define the circulating current frequencies nor the sequences required to achieve the energy management. This is certainly an advantage when the CCS-MPC is compared to the conventional approaches based on linear components where the circulating current references to compensate the energies $[\boldsymbol{\psi}_{\alpha\beta}\ \boldsymbol{\psi}_{\varepsilon 12}\ \boldsymbol{\psi}_{\varepsilon 34}]$ are obtained from 8 energy control loops which have to be separately tuned and implemented to avoid coupling between them. Additionally,in the conventional approaches, the complexity is further increased considering that the circulating current references, required to balance the energy in the M3C, have to have several frequencies and positive/negative sequence components.

According to the obtained simulation and experimental work considering steady state and transient scenarios, the good results confirm the advantages of the proposed approach.

Circulating Current Control Second MPC Stage

Regarding this second stage, its most attractive feature relies on the available saturation scheme, which regulates the thermal limit of the arm currents of the M3C and the saturation of the arm output voltages. Saturation and thermal protection are important tasks which are very difficult to address using conventional linear controllers considering that, in a typical modular multilevel matrix converter, each cluster current has components of several frequencies and positive and negative sequences. Therefore, using linear methods it is difficult to implement optimal limitation of these circulating currents and, at the same time, to avoid affecting the input/output currents. However, this task is simple to achieve using the CCS-MPC methodology that, unlike conventional FS-MPC strategies, is suitable for experimental implementation with present control platforms, providing saturation when required.

The proposed saturation scheme is specially attractive during short-period high demand of circulating currents in transient conditions. Additionally, the saturation scheme is conveniently integrated into the MPC formulation for the regulation of the circulating currents. In order to solve the overall optimisation problem, with the integrated constraints, an Active-Set algorithm, suitable for experimental implementation, is integrated into the proposed control methodology.

From the presented formulation, two approaches are derived (scheme-A and -B) in this work. In scheme-A the model of the load/grid is not known and the prediction of the output currents is replaced by the sampled measurement. On the other hand, in scheme-B the models of the load/grid are known and are integrated in the optimisation problem computation. The simulation and experimental results are promising and validate the usefulness of the circulating current control scheme with its algorithm. The attractive features of the scheme are shown during transient operation, where the saturation scheme performance is adequate for a sampling and carrier period of 320μs in the experimental validation. Regarding the

performance between the two derived approaches, scheme-B has better regulation of the arm currents than scheme-A during transient operation.

As a general conclusion derived from the obtained results, the CCS-MPC using just the circulating currents has less computational burden than incorporating the nine arm currents. Nevertheless, even though the proposed control scheme may have less controllability, the advantages of the proposed strategy, demonstrated using several experimental and simulation tests, have been clearly identified, i.e. when the arm voltages and/or currents reach the specified bounds, they are modified in order to operate the arm-voltage/-current magnitudes within the limits, without affecting either the input or output port currents.

9.1. Contributions and Future Work

During the development of this project, various journal and conference papers have been published. A group of these publications are directly linked to the presented thesis work. In contrast, the other publications were developed in parallel and are not necessarily correlated with the same field from my PhD project.

9.1.1. Journal Publications

Derived from Thesis Project

(1) **M. Urrutia**, R. Cárdenas, J. C. Clare, and A. Watson, *Circulating current control for the modular multilevel matrix converter based on model predictive control*, IEEE Journal of Emerging and Selected Topics in Power Electronics, vol. 9, no. 5, pp. 6069–6085, 2021.

(2) **M. Urrutia**, R. Cardenas-Dobson, J. C. Clare, M. Diaz, and A. J. Watson, *Continuous set model predictive control for energy management of modular multilevel matrix converters*, IEEE Transactions on Power Electronics, pp. 1–1, 2021.

Participation as Co-author

(3) M. Díaz, R. Cárdenas, E. Ibaceta, A. Mora, **M. Urrutia**, M. Espinoza, F. Rojas, and P. Wheeler, *An Overview of Modelling Techniques and Control Strategies for Modular Multilevel Matrix Converters*, Energies, vol. 13, no. 18, p. 4678, Sep. 2020.

(4) M. Díaz, R. Cárdenas, E. Ibaceta, A. Mora, **M. Urrutia**, M. Espinoza, F. Rojas, and P. Wheeler, *An Overview of Applications of the Modular Multilevel Matrix Converter*, Energies, vol. 13, no. 21, p. 5546, Oct. 2020.

(5) A. Mora, **M. Urrutia**, R. Cárdenas, A. Angulo, M. Espinoza, M. Díaz, and P. Lezana, *Model-predictive-control-based capacitor voltage balancing strategies for modular multilevel converters*, IEEE Transactions on Industrial Electronics, vol. 66, no. 3, pp. 2432–2443, 2019.

(6) A. Mora, R. Cárdenas, **M. Urrutia**, M. Espinoza, and M. Díaz, *A vector control strategy to eliminate active power oscillations in four-leg grid-connected converters under unbalanced voltages*, IEEE Journal of Emerging and Selected Topics in Power Electronics, vol. 8, no. 2, pp. 1728–1738, 2020.

9.1.2. Conference Publications

Derived from Thesis Project

(7) **M. Urrutia**, F. Donoso, A. Mora, E. Espina, M. Diaz, and R. Cárdenas, *Enhanced circulating current control for the modular multilevel matrix converter based on model*

predictive control, in 2019 21st European Conference on Power Electronics and Applications (EPE '19 ECCE Europe), 2019, pp. 1–9.

Not related to Thesis Project

(8) **M. Urrutia**, A. Mora, A. Angulo, P. Lezana, R. Cárdenas, and M. Diaz, *A novel capacitor voltage balancing strategy for modular multilevel converters*, in 2017 IEEE Southern Power Electronics Conference (SPEC), 2017, pp. 1–6.

(9) A. Mora, F. Donoso, **M. Urrutia**, A. Angulo, and R. Cárdenas, *Predictive control strategy for an induction machine fed by a 3l-npc converter with fixed switching frequency and improved tracking error*, in 2018 IEEE 27th International Symposium on Industrial Electronics (ISIE), 2018, pp. 155–160.

(10) T. Roje, A. Navas, **M. Urrutia**, P. Mendoza-Araya, and G. Jiménez-Estévez, *Advanced lead-acid battery models for the state-of-charge estimation in an isolated microgrid*, in 2019 IEEE CHILEAN Conference on Electrical, Electronics Engineering, Information and Communication Technologies (CHILECON), 2019, pp. 1–6.

(11) F. Donoso, A. Mora, M. Espinoza, **M. Urrutia**, E. Espina, and R. Cardenas, *Predictive-based modulation schemes for the hybrid modular multilevel converter*, in 2019 21st European Conference on Power Electronics and Applications (EPE '19 ECCE Europe), 2019, P.1–P.9.

(12) E. Espina, R. Cárdenas, F. Donoso, **M. Urrutia**, and M. Espinoza, *A novel distributed secondary control strategy applied to hybrid ac/dc microgrids*, in 2019 21st European Conference on Power Electronics and Applications (EPE '19 ECCE Europe), 2019, P.1–P.9.

(13) M. Diaz, E. Ibaceta, A. Duran, C. Melendez, **M. Urrutia**, and F. Rojas, *Field oriented control of a modular multilevel matrix converter based variable speed drive*, in 2019 21st European Conference on Power Electronics and Applications (EPE '19 ECCE Europe), 2019, P.1–P.6.

(14) M. Espinoza-B., F. Donoso-M., M. Diaz-D., **M. Urrutia**, and R. Cardenas-D, *A novel control system for medium-voltage hexverter-based drives*, in 2020 Fifteenth International Conference on Ecological Vehicles and Renewable Energies (EVER), 2020, pp. 1–7.

(15) A. Fayyaz, Z. Wang, **M. Urrutia**, T. Yang, and P. Wheeler, *Design considerations for high-voltage high-current bi-directional dc solid-state circuit breaker (sscb) for aerospace applications*, in 2021 23rd European Conference on Power Electronics and Applications (EPE'21 ECCE Europe), 2021, P.1–P.10.

9.1.3. Future Work

In accordance with the development of the presented work, the following ideas emerged for further investigation.

- A singular CCV balacing and circulating current regulation CCS-MPC scheme can be introduced with a singular optimisation problem. The basic idea is to merge the proposed two-stage CCS-MPC scheme into a singular one with the same inputs and outputs.

- Since the T-SSCV dynamic relations are non-linear, the discrete modelling of the system can be further studied in order to verify the fidelity.

- Study the effects on the capacitor voltages and arm currents using different common-mode voltage waveforms and frequencies. Ideally, to propose a methodology or closed-loop control scheme for an optimal definition.

- Present an extended weight cost analysis for DFM and EFM. Include experimental results in the steady-state analysis at different weight costs.

- To improve the operation of the M3C during EFM by introducing a tolerance band. This goal aims to operate with a predefined band for the CCV oscillations, which should require less circulating current amplitudes and common-mode voltage.

- To evaluate the proposed scheme for different Modular Multilevel Converter topologies.

- To extend the applicability of the presented scheme during arm faults. This implies that the circulating currents have to be redefined in accordance of the faulty arm.

Bibliography

[1] B. Wu and M. Narimani, *High-Power Converters and AC Drives*, ser. IEEE Press Series on Power Engineering. Wiley, 2017.

[2] J. Rodriguez, Jih-Sheng Lai, and Fang Zheng Peng, "Multilevel inverters: a survey of topologies, controls, and applications," *IEEE Transactions on Industrial Electronics*, vol. 49, no. 4, pp. 724–738, 2002.

[3] E. I. E. Agency, "Energy efficiency roadmap for electric motors and motor systems," 2015.

[4] B. Wu, J. Pontt, J. Rodriguez, S. Bernet, and S. Kouro, "Current-source converter and cycloconverter topologies for industrial medium-voltage drives," *IEEE Transactions on Industrial Electronics*, vol. 55, no. 7, pp. 2786–2797, 2008.

[5] Z. Wang, B. Wu, D. Xu, and N. R. Zargari, "A current-source-converter-based high-power high-speed pmsm drive with 420-hz switching frequency," *IEEE Transactions on Industrial Electronics*, vol. 59, no. 7, pp. 2970–2981, 2012.

[6] H. Abu-Rub, J. Holtz, J. Rodriguez, and G. Baoming, "Medium-voltage multilevel converters—state of the art, challenges, and requirements in industrial applications," *IEEE Transactions on Industrial Electronics*, vol. 57, no. 8, pp. 2581–2596, 2010.

[7] L. G. Franquelo, J. Rodriguez, J. I. Leon, S. Kouro, R. Portillo, and M. A. Prats, "The age of multilevel converters arrives," *IEEE Industrial Electronics Magazine*, vol. 2, no. 2, pp. 28–39, 2008.

[8] J. Rodriguez, S. Bernet, B. Wu, J. O. Pontt, and S. Kouro, "Multilevel voltage-source-converter topologies for industrial medium-voltage drives," *IEEE Transactions on Industrial Electronics*, vol. 54, no. 6, pp. 2930–2945, 2007.

[9] S. Kouro, J. Rodriguez, B. Wu, S. Bernet, and M. Perez, "Powering the future of industry: High-power adjustable speed drive topologies," *IEEE Industry Applications Magazine*, vol. 18, no. 4, pp. 26–39, 2012.

[10] H. Akagi, "Classification, terminology, and application of the modular multilevel

cascade converter (mmcc)," in *The 2010 International Power Electronics Conference - ECCE ASIA* -, 2010, pp. 508–515.

[11] M. A. Perez, S. Bernet, J. Rodriguez, S. Kouro, and R. Lizana, "Circuit topologies, modeling, control schemes, and applications of modular multilevel converters," *IEEE Transactions on Power Electronics*, vol. 30, no. 1, pp. 4–17, 2015.

[12] M. Espinoza, R. Cardenas, M. Diaz, and J. C. Clare, "An Enhanced dq-Based Vector Control System for Modular Multilevel Converters Feeding Variable-Speed Drives," *IEEE Transactions on Industrial Electronics*, vol. 64, no. 4, pp. 2620–2630, apr 2017.

[13] M. Diaz, R. Cardenas, M. Espinoza, F. Rojas, A. Mora, J. C. Clare, and P. Wheeler, "Control of wind energy conversion systems based on the modular multilevel matrix converter," *IEEE Transactions on Industrial Electronics*, vol. 64, no. 11, pp. 8799–8810, 2017.

[14] "Sinamics perfect harmony gh180 air-cooled drives," Siemens Industry 2021.

[15] "Hvdc light (vsc)," *www.hitachiabb-powergrids.com/offering/product-andsystem /hvdc/hvdc-light*, ABB 2019.

[16] "Hvdc flexible," *www.narigroup.com/c-epri/products/flexible.html*, C-EPRI 2019.

[17] "Hvdc systems," *www.gegridsolutions.com/systems_ services/catalog /hvdc/*, GE Grid Solutions 2019.

[18] J. Kucka, D. Karwatzki, and A. Mertens, "AC/AC modular multilevel converters in wind energy applications: Design considerations," in *2016 18th European Conference on Power Electronics and Applications, EPE 2016 ECCE Europe*. IEEE, 9 2016, pp. 1–10. [Online]. Available: http://ieeexplore.ieee.org/document/7695542/

[19] K. Ilves, L. Bessegato, and S. Norrga, "Comparison of cascaded multilevel converter topologies for AC/AC conversion," in *2014 International Power Electronics Conference, IPEC-Hiroshima - ECCE Asia 2014*, 5 2014, pp. 1087–1094.

[20] H. Akagi, "Multilevel converters: Fundamental circuits and systems," *Proceedings of the IEEE*, vol. 105, no. 11, pp. 2048–2065, 2017.

[21] M. Diaz, R. Cardenas, M. Espinoza, C. M. Hackl, F. Rojas, J. C. Clare, and P. Wheeler, "Vector control of a modular multilevel matrix converter operating over the full output-frequency range," *IEEE Transactions on Industrial Electronics*, vol. 66, no. 7, pp. 5102–5114, 2019.

[22] F. Kammerer, M. Gommeringer, J. Kolb, and M. Braun, "Energy balancing of the modular multilevel matrix converter based on a new transformed arm power analysis," in *2014 16th European Conference on Power Electronics and Applications*, 2014, pp.

1–10.

[23] F. Kammerer, J. Kolb, and M. Braun, "Fully decoupled current control and energy balancing of the modular multilevel matrix converter," in *2012 15th International Power Electronics and Motion Control Conference (EPE/PEMC)*, 2012, pp. LS2a.3–1–LS2a.3–8.

[24] W. Kawamura, M. Hagiwara, and H. Akagi, "Control and experiment of a modular multilevel cascade converter based on triple-star bridge cells," *IEEE Transactions on Industry Applications*, vol. 50, no. 5, pp. 3536–3548, 2014.

[25] W. Kawamura, K. Chen, M. Hagiwara, and H. Akagi, "A low-speed, high-torque motor drive using a modular multilevel cascade converter based on triple-star bridge cells (mmcc-tsbc)," *IEEE Transactions on Industry Applications*, vol. 51, no. 5, pp. 3965–3974, 2015.

[26] W. Kawamura, Y. Chiba, M. Hagiwara, and H. Akagi, "Experimental verification of an electrical drive fed by a modular multilevel tsbc converter when the motor frequency gets closer or equal to the supply frequency," *IEEE Transactions on Industry Applications*, vol. 53, no. 3, pp. 2297–2306, 2017.

[27] A. Duran, E. Ibaceta, M. Diaz, F. Rojas, R. Cardenas, and H. Chavez, "Control of a Modular Multilevel Matrix Converter for Unified Power Flow Controller Applications," *Energies*, vol. 13, no. 4, p. 953, feb 2020.

[28] R. Cardenas, M. Diaz, F. Rojas, J. Clare, and P. Wheeler, "Resonant control system for low-voltage ride-through in wind energy conversion systems," *IET Power Electronics*, vol. 9, no. 6, pp. 1297–1305, 2016.

[29] A. Dekka, B. Wu, R. L. Fuentes, M. Perez, and N. R. Zargari, "Evolution of topologies, modeling, control schemes, and applications of modular multilevel converters," *IEEE Journal of Emerging and Selected Topics in Power Electronics*, vol. 5, no. 4, pp. 1631–1656, 2017.

[30] J. Rodriguez and P. Cortes, *Predictive Control of Power Converters and Electrical Drives*, ser. Wiley - IEEE. Wiley, 2012.

[31] T. Geyer, *Model Predictive Control of High Power Converters and Industrial Drives*. Wiley, 2016.

[32] S. Kouro, M. A. Perez, J. Rodriguez, A. M. Llor, and H. A. Young, "Model predictive control: Mpc's role in the evolution of power electronics," *IEEE Industrial Electronics Magazine*, vol. 9, no. 4, pp. 8–21, 2015.

[33] S. Vazquez, J. Rodriguez, M. Rivera, L. G. Franquelo, and M. Norambuena, "Model

predictive control for power converters and drives: Advances and trends," *IEEE Transactions on Industrial Electronics*, vol. 64, no. 2, pp. 935–947, 2017.

[34] A. Dekka, B. Wu, V. Yaramasu, R. L. Fuentes, and N. R. Zargari, "Model predictive control of high-power modular multilevel converters - an overview," *IEEE Journal of Emerging and Selected Topics in Power Electronics*, vol. 7, no. 1, pp. 168–183, 2019.

[35] A. Mora, M. Espinoza, M. Díaz, and R. Cárdenas, "Model predictive control of modular multilevel matrix converter," in *2015 IEEE 24th International Symposium on Industrial Electronics (ISIE)*, 2015, pp. 1074–1079.

[36] B. Fan, K. Wang, P. Wheeler, C. Gu, and Y. Li, "An optimal full frequency control strategy for the modular multilevel matrix converter based on predictive control," *IEEE Transactions on Power Electronics*, vol. 33, no. 8, pp. 6608–6621, 2018.

[37] H. Mahmoudi, M. Aleenejad, and R. Ahmadi, "Modulated model predictive control of modular multilevel converters in vsc-hvdc systems," *IEEE Transactions on Power Delivery*, vol. 33, no. 5, pp. 2115–2124, 2018.

[38] J. Yin, J. I. Leon, M. A. Perez, L. G. Franquelo, A. Marquez, and S. Vazquez, "Model predictive control of modular multilevel converters using quadratic programming," *IEEE Transactions on Power Electronics*, vol. 36, no. 6, pp. 7012–7025, 2021.

[39] M. Malinowski, K. Gopakumar, J. Rodriguez, and M. A. Pérez, "A survey on cascaded multilevel inverters," *IEEE Transactions on Industrial Electronics*, vol. 57, no. 7, pp. 2197–2206, 2010.

[40] J. Rodriguez, S. Bernet, B. Wu, J. O. Pontt, and S. Kouro, "Multilevel voltage-source-converter topologies for industrial medium-voltage drives," *IEEE Transactions on Industrial Electronics*, vol. 54, no. 6, pp. 2930–2945, 2007.

[41] S. Kouro, M. Malinowski, K. Gopakumar, J. Pou, L. G. Franquelo, B. Wu, J. Rodriguez, M. A. Pérez, and J. I. Leon, "Recent advances and industrial applications of multilevel converters," *IEEE Transactions on Industrial Electronics*, vol. 57, no. 8, pp. 2553–2580, 2010.

[42] B. P. McGrath, T. Meynard, G. Gateau, and D. G. Holmes, "Optimal modulation of flying capacitor and stacked multicell converters using a state machine decoder," *IEEE Transactions on Power Electronics*, vol. 22, no. 2, pp. 508–516, 2007.

[43] D.-W. Kang, B.-K. Lee, J.-H. Jeon, T.-J. Kim, and D.-S. Hyun, "A symmetric carrier technique of crpwm for voltage balance method of flying-capacitor multilevel inverter," *IEEE Transactions on Industrial Electronics*, vol. 52, no. 3, pp. 879–888, 2005.

[44] J. Pereda and J. Dixon, "Cascaded multilevel converters: Optimal asymmetries and

floating capacitor control," *IEEE Transactions on Industrial Electronics*, vol. 60, no. 11, pp. 4784–4793, 2013.

[45] M. Diaz, R. Cárdenas Dobson, E. Ibaceta, A. Mora, M. Urrutia, M. Espinoza, F. Rojas, and P. Wheeler, "An overview of applications of the modular multilevel matrix converter," *Energies*, vol. 13, no. 21, 2020.

[46] D. Karwatzki, L. Baruschka, and A. Mertens, "Survey on the Hexverter topology - A modular multilevel AC/AC converter," *9th International Conference on Power Electronics - ECCE Asia: "Green World with Power Electronics", ICPE 2015-ECCE Asia*, pp. 1075–1082, 2015.

[47] M. M. C. Merlin, T. C. Green, S. Member, P. D. Mitcheson, S. Member, D. R. Trainer, R. Critchley, W. Crookes, and F. Hassan, "The Alternate Arm Converter : A New Hybrid Multilevel Converter With DC-Fault Blocking Capability," vol. 29, no. 1, pp. 310–317, 2014.

[48] A. Nami, J. Liang, F. Dijkhuizen, and G. D. Demetriades, "Modular multilevel converters for hvdc applications: Review on converter cells and functionalities," *IEEE Transactions on Power Electronics*, vol. 30, no. 1, pp. 18–36, 2015.

[49] G. P. Adam, I. Abdelsalam, J. E. Fletcher, G. M. Burt, D. Holliday, and S. J. Finney, "New efficient submodule for a modular multilevel converter in multiterminal hvdc networks," *IEEE Transactions on Power Electronics*, vol. 32, no. 6, pp. 4258–4278, 2017.

[50] M. Farhadi Kangarlu and E. Babaei, "Cross-switched multilevel inverter: an innovative topology," *IET Power Electronics*, vol. 6, no. 4, pp. 642–651, 2013.

[51] X. Li, W. Liu, Q. Song, H. Rao, and S. Xu, "An enhanced mmc topology with dc fault ride-through capability," in *IECON 2013 - 39th Annual Conference of the IEEE Industrial Electronics Society*, 2013, pp. 6182–6188.

[52] F. Donoso, R. Cardenas, M. Espinoza, J. Clare, A. Mora, and A. Watson, "Experimental validation of a nested control system to balance the cell capacitor voltages in hybrid mmcs," *IEEE Access*, vol. 9, pp. 21 965–21 985, 2021.

[53] X. Yang, T. Q. Zheng, Z. Lin, T. Xiong, and X. You, "Power quality controller based on hybrid modular multilevel converter," in *2012 IEEE International Symposium on Industrial Electronics*, 2012, pp. 1997–2002.

[54] M. Kaya, A. Costabeber, A. J. Watson, F. Tardelli, and J. C. Clare, "A push–pull series connected modular multilevel converter for hvdc applications," *IEEE Transactions on Power Electronics*, vol. 37, no. 3, pp. 3111–3129, 2022.

[55] M. A. Perez, S. Ceballos, G. Konstantinou, J. Pou, and R. P. Aguilera, "Modular multilevel converters: Recent achievements and challenges," *IEEE Open Journal of the Industrial Electronics Society*, vol. 2, pp. 224–239, 2021.

[56] A. J. Korn, M. Winkelnkemper, P. Steimer, and J. W. Kolar, "Direct modular multi-level converter for gearless low-speed drives," in *Proceedings of the 2011 14th European Conference on Power Electronics and Applications*, 2011, pp. 1–7.

[57] J. Pereda and T. C. Green, "Direct modular multilevel converter with six branches for flexible distribution networks," *IEEE Transactions on Power Delivery*, vol. 31, no. 4, pp. 1728–1737, 2016.

[58] R. W. Erickson and O. A. Al-Naseem, "A new family of matrix converters," in *IECON'01. 27th Annual Conference of the IEEE Industrial Electronics Society (Cat. No.37243)*, vol. 2, 2001, pp. 1515–1520 vol.2.

[59] W. Kawamura, M. Hagiwara, H. Akagi, M. Tsukakoshi, R. Nakamura, and S. Kodama, "Ac-inductors design for a modular multilevel tsbc converter, and performance of a low-speed high-torque motor drive using the converter," *IEEE Transactions on Industry Applications*, vol. 53, no. 5, pp. 4718–4729, 2017.

[60] J. Kolb, F. Kammerer, and M. Braun, "Dimensioning and design of a modular multilevel converter for drive applications," in *2012 15th International Power Electronics and Motion Control Conference (EPE/PEMC)*, 2012, pp. LS1a–1.1–1–LS1a–1.1–8.

[61] R. Erickson, S. Angkititrakul, and K. Almazeedi, "A New Family of Multilevel Matrix Converters for Wind Power Applications: Final Report," *National Renewable Energy Laboratory (NREL)*, vol. NREL/SR-50, no. December, p. 2002, 2006. [Online]. Available: http://www.nrel.gov/wind/pdfs/40051.pdf

[62] N. Thitichaiworakorn, M. Hagiwara, and H. Akagi, "A medium-voltage large wind turbine generation system using an ac/ac modular multilevel cascade converter," *IEEE Journal of Emerging and Selected Topics in Power Electronics*, vol. 4, no. 2, pp. 534–546, 2016.

[63] T. Funaki and K. Matsuura, "Feasibility of the low frequency ac transmission," in *2000 IEEE Power Engineering Society Winter Meeting. Conference Proceedings (Cat. No.00CH37077)*, vol. 4, 2000, pp. 2693–2698 vol.4.

[64] W. Fischer, R. Braun, and I. Erlich, "Low frequency high voltage offshore grid for transmission of renewable power," in *2012 3rd IEEE PES Innovative Smart Grid Technologies Europe (ISGT Europe)*, 2012, pp. 1–6.

[65] Y. Miura, T. Mizutani, M. Ito, and T. Ise, "Modular multilevel matrix converter for low frequency ac transmission," in *2013 IEEE 10th International Conference on Power*

Electronics and Drive Systems (PEDS), 2013, pp. 1079–1084.

[66] C. Yuan, R. Zhou, and M. Tong, "Topologies and control of low-frequency alternating current for offshore wind farms based on modular multilevel matrix converter," *The Journal of Engineering*, vol. 2019, no. 16, pp. 2271–2277, 3 2019.

[67] J. Ma, M. Dahidah, V. Pickert, and J. Yu, "Modular multilevel matrix converter for offshore low frequency AC transmission system," in *IEEE International Symposium on Industrial Electronics*. IEEE, 4 2017, pp. 768–774. [Online]. Available: http://ieeexplore.ieee.org/lpdocs/epic03/wrapper.htm?arnumber=6527180

[68] L. Huang, X. Yang, B. Zhang, L. Qiao, H. Li, and M. Tian, "Hierarchical model predictive control of modular multilevel matrix converter for low frequency AC transmission," *9th International Conference on Power Electronics - ECCE Asia: "Green World with Power Electronics", ICPE 2015-ECCE Asia*, pp. 927–933, 7 2015.

[69] S. Liu, X. Wang, Y. Meng, P. Sun, H. Luo, and B. Wang, "A decoupled control strategy of modular multilevel matrix converter for fractional frequency transmission system," *IEEE Transactions on Power Delivery*, vol. 32, no. 4, pp. 2111–2121, 8 2017.

[70] M. Al-Tameemi, Y. Miura, J. Liu, H. Bevrani, and T. Ise, "A novel control scheme for multi-terminal low-frequency AC electrical energy transmission systems using modular multilevel matrix converters and virtual synchronous generator concept," *Energies*, vol. 13, no. 3, p. 747, 2 2020.

[71] A. Duran, E. Ibaceta, M. Diaz, F. Rojas, R. Cardenas, and H. Chavez, "Control of a modular multilevel matrix converter for unified power flow controller applications," *Energies*, vol. 13, no. 4, p. 953, 2 2020. [Online]. Available: https://www.mdpi.com/1996-1073/13/4/953

[72] W. Kawamura, Y. Chiba, M. Hagiwara, and H. Akagi, "Experimental Verification of an Electrical Drive Fed by a Modular Multilevel TSBC Converter When the Motor Frequency Gets Closer or Equal to the Supply Frequency," *IEEE Transactions on Industry Applications*, vol. 53, no. 3, pp. 2297–2306, 5 2017. [Online]. Available: http://ieeexplore.ieee.org/document/7845641/

[73] W. Zhou, J. Sheng, H. Luo, W. Li, and X. He, "Detection and localization of submodule open-circuit failures for modular multilevel converters with single ring theorem," *IEEE Transactions on Power Electronics*, vol. 34, no. 4, pp. 3729–3739, 2019.

[74] M. Chai, N. B. Y. Gorla, and S. K. Panda, "Fault detection and localization for cascaded h-bridge multilevel converter with model predictive control," *IEEE Transactions on Power Electronics*, vol. 35, no. 10, pp. 10 109–10 120, 2020.

[75] B. Fan, K. Wang, Z. Zheng, L. Xu, and Y. Li, "Optimized branch current control

of modular multilevel matrix converters under branch fault conditions," *IEEE Transactions on Power Electronics*, vol. 33, no. 6, pp. 4578–4583, 2018.

[76] C. Wang, Z. Zheng, K. Wang, and Y. Li, "Submodule fault-tolerant control of modular multilevel matrix converters with adaptive optimum common-mode voltage injection," *IEEE Transactions on Power Electronics*, vol. 37, no. 7, pp. 7548–7554, 2022.

[77] ——, "Fault detection and tolerant control of igbt open-circuit failures in modular multilevel matrix converters," *IEEE Journal of Emerging and Selected Topics in Power Electronics*, pp. 1–1, 2022.

[78] D. Karwatzki and A. Mertens, "Generalized control approach for a class of modular multilevel converter topologies," *IEEE Transactions on Power Electronics*, vol. 33, no. 4, pp. 2888–2900, 2018.

[79] M. Espinoza, R. Cardenas, M. Diaz, and J. C. Clare, "An enhanced dq-based vector control system for modular multilevel converters feeding variable-speed drives," *IEEE Transactions on Industrial Electronics*, vol. 64, no. 4, pp. 2620–2630, 2017.

[80] A. Mora, M. Urrutia, R. Cárdenas, A. Angulo, M. Espinoza, M. Díaz, and P. Lezana, "Model-predictive-control-based capacitor voltage balancing strategies for modular multilevel converters," *IEEE Transactions on Industrial Electronics*, vol. 66, no. 3, pp. 2432–2443, 2019.

[81] R. Teodorescu, M. Liserre, and P. Rodriguez, *Grid Converters for Photovoltaic and Wind Power Systems*, ser. Wiley - IEEE. Wiley, 2011.

[82] R. Cárdenas, R. Peña, M. Pérez, J. Clare, G. Asher, and F. Vargas, "Vector control of front-end converters for variable-speed wind-diesel systems," *IEEE Transactions on Industrial Electronics*, vol. 53, no. 4, pp. 1127–1136, 2006.

[83] W. Kawamura, Y. Chiba, M. Hagiwara, and H. Akagi, "Experimental verification of tsbc-based electrical drives when the motor frequency is passing through, or equal to, the supply frequency," in *2015 IEEE Energy Conversion Congress and Exposition (ECCE)*, 2015, pp. 5490–5497.

[84] M. Urrutia, A. Mora, A. Angulo, P. Lezana, R. Cárdenas, and M. Diaz, "A novel capacitor voltage balancing strategy for modular multilevel converters," in *2017 IEEE Southern Power Electronics Conference (SPEC)*, 2017, pp. 1–6.

[85] J. Huang, B. Yang, F. Guo, Z. Wang, X. Tong, A. Zhang, and J. Xiao, "Priority sorting approach for modular multilevel converter based on simplified model predictive control," *IEEE Transactions on Industrial Electronics*, vol. 65, no. 6, pp. 4819–4830, 2018.

[86] P. Liu, Y. Wang, W. Cong, and W. Lei, "Grouping-sorting-optimized model predictive

control for modular multilevel converter with reduced computational load," *IEEE Transactions on Power Electronics*, vol. 31, no. 3, pp. 1896–1907, 2016.

[87] J. I. Y. Ota, Y. Shibano, N. Niimura, and H. Akagi, "A phase-shifted-pwm d-statcom using a modular multilevel cascade converter (ssbc)—part i: Modeling, analysis, and design of current control," *IEEE Transactions on Industry Applications*, vol. 51, no. 1, pp. 279–288, 2015.

[88] F. Kammerer, J. Kolb, and M. Braun, "A novel cascaded vector control scheme for the modular multilevel matrix converter," in *IECON 2011 - 37th Annual Conference of the IEEE Industrial Electronics Society*, 2011, pp. 1097–1102.

[89] P. Hu and D. Jiang, "A level-increased nearest level modulation method for modular multilevel converters," *IEEE Transactions on Power Electronics*, vol. 30, no. 4, pp. 1836–1842, 2015.

[90] W. Huang, Y. Huang, M. Li, and W. Gong, "Stability analysis of modular multilevel converter using nearest level modulation," in *IECON 2016 - 42nd Annual Conference of the IEEE Industrial Electronics Society*, 2016, pp. 2582–2587.

[91] J. Rawlings, D. Mayne, and M. Diehl, *Model Predictive Control: Theory, Computation, and Design*. Nob Hill Publishing, 2017.

[92] S. Vazquez, J. Rodriguez, M. Rivera, L. G. Franquelo, and M. Norambuena, "Model predictive control for power converters and drives: Advances and trends," *IEEE Transactions on Industrial Electronics*, vol. 64, no. 2, pp. 935–947, 2017.

[93] P. Cortés, A. Wilson, S. Kouro, J. Rodriguez, and H. Abu-Rub, "Model predictive control of multilevel cascaded h-bridge inverters," *IEEE Transactions on Industrial Electronics*, vol. 57, no. 8, pp. 2691–2699, 2010.

[94] V. Yaramasu and B. Wu, "Predictive control of a three-level boost converter and an npc inverter for high-power pmsg-based medium voltage wind energy conversion systems," *IEEE Transactions on Power Electronics*, vol. 29, no. 10, pp. 5308–5322, 2014.

[95] B. Long, T. Cao, W. Fang, K. T. Chong, and J. M. Guerrero, "Model predictive control of a three-phase two-level four-leg grid-connected converter based on sphere decoding method," *IEEE Transactions on Power Electronics*, vol. 36, no. 2, pp. 2283–2297, 2021.

[96] P. Karamanakos, T. Geyer, and R. P. Aguilera, "Long-horizon direct model predictive control: Modified sphere decoding for transient operation," *IEEE Transactions on Industry Applications*, vol. 54, no. 6, pp. 6060–6070, 2018.

[97] R. Baidya, R. P. Aguilera, P. Acuña, S. Vazquez, and H. d. T. Mouton, "Multistep model predictive control for cascaded h-bridge inverters: Formulation and analysis,"

IEEE Transactions on Power Electronics, vol. 33, no. 1, pp. 876–886, 2018.

[98] T. Geyer and D. E. Quevedo, "Multistep finite control set model predictive control for power electronics," *IEEE Transactions on Power Electronics*, vol. 29, no. 12, pp. 6836–6846, 2014.

[99] L. Tarisciotti, P. Zanchetta, A. Watson, S. Bifaretti, and J. C. Clare, "Modulated model predictive control for a seven-level cascaded h-bridge back-to-back converter," *IEEE Transactions on Industrial Electronics*, vol. 61, no. 10, pp. 5375–5383, 2014.

[100] L. Tarisciotti, A. Formentini, A. Gaeta, M. Degano, P. Zanchetta, R. Rabbeni, and M. Pucci, "Model predictive control for shunt active filters with fixed switching frequency," *IEEE Transactions on Industry Applications*, vol. 53, no. 1, pp. 296–304, 2017.

[101] L. Tarisciotti, J. Lei, A. Formentini, A. Trentin, P. Zanchetta, P. Wheeler, and M. Rivera, "Modulated predictive control for indirect matrix converter," *IEEE Transactions on Industry Applications*, vol. 53, no. 5, pp. 4644–4654, 2017.

[102] F. Donoso, A. Mora, R. Cárdenas, A. Angulo, D. Sáez, and M. Rivera, "Finite-set model-predictive control strategies for a 3l-npc inverter operating with fixed switching frequency," *IEEE Transactions on Industrial Electronics*, vol. 65, no. 5, pp. 3954–3965, 2018.

[103] Z. Zhou, C. Xia, Y. Yan, Z. Wang, and T. Shi, "Torque ripple minimization of predictive torque control for pmsm with extended control set," *IEEE Transactions on Industrial Electronics*, vol. 64, no. 9, pp. 6930–6939, 2017.

[104] Z. Mynar, L. Vesely, and P. Vaclavek, "Pmsm model predictive control with field-weakening implementation," *IEEE Transactions on Industrial Electronics*, vol. 63, no. 8, pp. 5156–5166, 2016.

[105] S. Mariethoz and M. Morari, "Explicit model-predictive control of a pwm inverter with an lcl filter," *IEEE Transactions on Industrial Electronics*, vol. 56, no. 2, pp. 389–399, 2009.

[106] K. Belda and D. Vošmik, "Explicit generalized predictive control of speed and position of pmsm drives," *IEEE Transactions on Industrial Electronics*, vol. 63, no. 6, pp. 3889–3896, 2016.

[107] S. Boyd, S. Boyd, and Vandenberghe, *Convex Optimization*, ser. Berichte über verteilte messysteme. Cambridge University Press, 2004, no. parte 1.

[108] D. Bertsekas and M. I. of Technology, *Convex Optimization Algorithms*. Athena Scientific, 2015.

[109] J. Nocedal and S. Wright, *Numerical Optimization*, ser. Springer Series in Operations Research and Financial Engineering. Springer New York, 2006.

[110] M. S. K. Lau, S. P. Yue, K. V. Ling, and J. M. Maciejowski, "A comparison of interior point and active set methods for fpga implementation of model predictive control," in *2009 European Control Conference (ECC)*, 2009, pp. 156–161.

[111] R. A. Bartlett, A. Wachter, and L. T. Biegler, "Active set vs. interior point strategies for model predictive control," in *Proceedings of the 2000 American Control Conference. ACC (IEEE Cat. No.00CH36334)*, vol. 6, 2000, pp. 4229–4233 vol.6.

[112] J. Qin and M. Saeedifard, "Predictive control of a modular multilevel converter for a back-to-back hvdc system," *IEEE Transactions on Power Delivery*, vol. 27, no. 3, pp. 1538–1547, 2012.

[113] H. Akagi, "Multilevel Converters: Fundamental Circuits and Systems," *Proceedings of the IEEE*, vol. 105, no. 11, pp. 2048–2065, 2017.

[114] B. Kouvaritakis and M. Cannon, *Model Predictive Control: Classical, Robust and Stochastic*, ser. Advanced Textbooks in Control and Signal Processing. Springer International Publishing, 2015.

[115] T. Orłowska-Kowalska, F. Blaabjerg, and J. Rodríguez, *Advanced and Intelligent Control in Power Electronics and Drives*, ser. Studies in Computational Intelligence. Springer International Publishing, 2014.

[116] F. Kammerer, M. Gommeringer, J. Kolb, and M. Braun, "Overload Capability of the Modular Multilevel Matrix Converter for Feeding High Torque Low Speed Drives," *proceedings IET*, pp. 20–27, 2014.

[117] M. Diaz, R. Cardenas, E. Ibaceta, A. Mora, M. Urrutia, M. Espinoza, F. Rojas, and P. Wheeler, "An overview of modelling techniques and control strategies for modular multilevel matrix converters," *Energies*, vol. 13, no. 18, p. 4678, 9 2020.

[118] S. A. Davari, V. Nekoukar, C. Garcia, and J. Rodriguez, "Online weighting factor optimization by simplified simulated annealing for finite set predictive control," *IEEE Transactions on Industrial Informatics*, vol. 17, no. 1, pp. 31–40, 2021.

[119] G. Franklin, J. Da Powell, and A. Emami-Naeini, *Feedback Control of Dynamic Systems*. Pearson Education, 2014.

[120] M. Hagiwara, I. Hasegawa, and H. Akagi, "Startup and low-speed operation of an adjustable-speed motor driven by a modular multilevel cascade inverter (mmci)," in *2012 IEEE Energy Conversion Congress and Exposition (ECCE)*, 2012, pp. 718–725.

[121] D. Holmes and T. Lipo, *Pulse Width Modulation for Power Converters: Principles and*

Practice, ser. IEEE Press Series on Power Engineering. Wiley, 2003.

Annexed

Model Predictive Control Definition

In order to properly define the foundations of the implemented MPC strategies for regulating the M3C, it is necessary to emphasize the general formulation of the Model Predictive Control (MPC) scheme. In this regard, a commonly used structure of MPC, which is properly defined in [114, 91], is the following,

$$\begin{aligned} \underset{\substack{\boldsymbol{x}_1,\ldots,\boldsymbol{x}_{\mathrm{N}_f} \\ \boldsymbol{u}_0,\ldots,\boldsymbol{u}_{\mathrm{N}_f\text{-}1}}}{\text{Minimize}} \quad & J = \sum_{k=0}^{\mathrm{N}_f-1} \left(\boldsymbol{x}_k^T \boldsymbol{Q} \boldsymbol{x}_k + \boldsymbol{u}_k^T \boldsymbol{R} \boldsymbol{u}_k\right) + \boldsymbol{x}_{\mathrm{N}_f}^T \boldsymbol{P} \boldsymbol{x}_{\mathrm{N}_f} \\ \text{subject to} \quad & \boldsymbol{x}_{\ell+1} = \boldsymbol{A}_{\mathrm{d}} \boldsymbol{x}_\ell + \boldsymbol{B}_{\mathrm{d}} \boldsymbol{u}_\ell + \boldsymbol{D}_{\mathrm{d}} \mathbf{d}_\ell \\ & \boldsymbol{F} \boldsymbol{x}_{\ell+1} + \boldsymbol{G} \boldsymbol{u}_{\ell+1} \leq \mathbf{1} \\ & \forall \ell \in \{0, 1, ..., \mathrm{N}_f - 1\} \end{aligned} \tag{1}$$

where the prediction horizon is N_f; for the ℓ-th instant, the state and input variables of the system are $\boldsymbol{x}_\ell$ and $\boldsymbol{u}_\ell$, respectively; and $\mathbf{d}_\ell$ is a known disturbance. The $\boldsymbol{Q}$ matrix defines the weights on the states while $\boldsymbol{R}$ matrix defines the weights on the control input in the cost function; the weight matrix $\boldsymbol{P}$ is associated with the invariant set defined by the control law $\boldsymbol{u}_j = K_P \boldsymbol{x}_j$, for $j > \mathrm{N}_f$ [114]. To ensure a global minimum, it is strictly necessary that $\boldsymbol{Q} \succeq 0$ and $\boldsymbol{R} \succ 0$ [114, 91].

The respective boundaries of the state and input variables are stated in the inequality constraints with matrices $\boldsymbol{F}$ and $\boldsymbol{G}$. Besides, the equality constraints describe the dynamic of the system in every instant within the prediction horizon. Additionally, it is stated that the disturbances are known at every instant.

Without losing generality, this formulation can be written in an extended matrix form as follows [115, 31],

$$\begin{aligned} \underset{\boldsymbol{X}_{\mathrm{N}_f}, \boldsymbol{U}_{\mathrm{N}_f}}{\text{Minimize}} \quad & J = \boldsymbol{X}_{\mathrm{N}_f}^T \boldsymbol{T}_{\boldsymbol{Q}} \boldsymbol{X}_{\mathrm{N}_f} + \boldsymbol{U}_{\mathrm{N}_f}^T \boldsymbol{T}_{\boldsymbol{R}} \boldsymbol{U}_{\mathrm{N}_f} \\ \text{subject to} \quad & \boldsymbol{X}_{\mathrm{N}_f} = \boldsymbol{T}_{\boldsymbol{A}} \boldsymbol{x}_0 + \boldsymbol{T}_{\boldsymbol{B}} \boldsymbol{U}_{\mathrm{N}_f} + \boldsymbol{T}_{\boldsymbol{D}} \boldsymbol{D}_{\mathrm{N}_f} \\ & \boldsymbol{T}_{\boldsymbol{F}} \boldsymbol{X}_{\mathrm{N}_f} + \boldsymbol{T}_{\boldsymbol{G}} \boldsymbol{U}_{\mathrm{N}_f} \leq \mathbf{1} \end{aligned} \tag{2}$$

where $\boldsymbol{X}_{\mathrm{N}_f} \triangleq [\boldsymbol{x}_0^T \ \boldsymbol{x}_1^T \ ... \ \boldsymbol{x}_{\mathrm{N}_f}^T]^T$, $\boldsymbol{U}_{\mathrm{N}_f} \triangleq [\boldsymbol{u}_0^T \ \boldsymbol{u}_1^T \ ... \ \boldsymbol{u}_{\mathrm{N}_f-1}^T]^T$, $\boldsymbol{D}_{\mathrm{N}_f} \triangleq [\mathbf{d}_0^T \ \mathbf{d}_1^T \ ... \ \mathbf{d}_{\mathrm{N}_f-1}^T]^T$, $\boldsymbol{T}_{\boldsymbol{Q}} \triangleq \mathrm{diag}(\boldsymbol{Q}, ..., \boldsymbol{Q}, \boldsymbol{P})$, $\boldsymbol{T}_{\boldsymbol{R}} \triangleq \mathrm{diag}(\boldsymbol{R}, ..., \boldsymbol{R})$, $\boldsymbol{T}_{\boldsymbol{F}} \triangleq \mathrm{diag}(\boldsymbol{F}, ..., \boldsymbol{F})$ and $\boldsymbol{T}_{\boldsymbol{G}} \triangleq \mathrm{diag}(\boldsymbol{G}, ..., \boldsymbol{G})$.

In addition,

$$\boldsymbol{T_A} = \begin{bmatrix} \boldsymbol{I} \\ \boldsymbol{A}_{\mathrm{d}} \\ \vdots \\ \vdots \\ \boldsymbol{A}_{\mathrm{d}}^{\mathrm{N}_f} \end{bmatrix}, \quad \boldsymbol{T_B} = \begin{bmatrix} \boldsymbol{0} & \cdots & \cdots & \boldsymbol{0} \\ \boldsymbol{B}_{\mathrm{d}} & \boldsymbol{0} & \cdots & \boldsymbol{0} \\ \boldsymbol{A}_{\mathrm{d}}\boldsymbol{B}_{\mathrm{d}} & \boldsymbol{B}_{\mathrm{d}} & \cdots & \boldsymbol{0} \\ \vdots & \vdots & \ddots & \vdots \\ \boldsymbol{A}_{\mathrm{d}}^{\mathrm{N}_f-1}\boldsymbol{B}_{\mathrm{d}} & \boldsymbol{A}_{\mathrm{d}}^{\mathrm{N}_f-2}\boldsymbol{B}_{\mathrm{d}} & \cdots & \boldsymbol{B}_{\mathrm{d}} \end{bmatrix} \text{ and } \boldsymbol{T_D} = \begin{bmatrix} \boldsymbol{0} & \cdots & \cdots & \boldsymbol{0} \\ \boldsymbol{D}_{\mathrm{d}} & \boldsymbol{0} & \cdots & \boldsymbol{0} \\ \boldsymbol{A}_{\mathrm{d}}\boldsymbol{D}_{\mathrm{d}} & \boldsymbol{D}_{\mathrm{d}} & \cdots & \boldsymbol{0} \\ \vdots & \vdots & \ddots & \vdots \\ \boldsymbol{A}_{\mathrm{d}}^{\mathrm{N}_f-1}\boldsymbol{D}_{\mathrm{d}} & \boldsymbol{A}_{\mathrm{d}}^{\mathrm{N}_f-2}\boldsymbol{D}_{\mathrm{d}} & \cdots & \boldsymbol{D}_{\mathrm{d}} \end{bmatrix} \tag{3}$$

are the matrices related to the extended dynamic of the system (equality constraint).

Assuming that the disturbance $\boldsymbol{D}_{\mathrm{N}_f}$ is known, the equality constraint can be conveniently replaced in the cost function of (2), and the problem can be reformulated as,

$$\begin{aligned} \underset{\boldsymbol{U}_{N_k}}{\text{Minimize}} \quad & J = \left(\boldsymbol{U}_{N_k} - \boldsymbol{U}_{unc}\right)^T \boldsymbol{H} \left(\boldsymbol{U}_{N_k} - \boldsymbol{U}_{unc}\right) \\ \text{subject to} \quad & \boldsymbol{K}\boldsymbol{U}_{N_k} \leq \boldsymbol{L} \end{aligned} \tag{4}$$

where

$$\begin{aligned} \boldsymbol{U}_{unc} &= -\boldsymbol{H}^{-1}\boldsymbol{T}_{\boldsymbol{B}}^T\boldsymbol{T}_{\boldsymbol{Q}}(\boldsymbol{T}_{\boldsymbol{A}}\boldsymbol{x}_0 + \boldsymbol{T}_{\boldsymbol{D}}\boldsymbol{D}_{\mathrm{N}_f}) \\ \boldsymbol{H} &= \boldsymbol{T}_{\boldsymbol{B}}^T\boldsymbol{T}_{\boldsymbol{Q}}\boldsymbol{T}_{\boldsymbol{B}} + \boldsymbol{T}_{\boldsymbol{R}} \\ \boldsymbol{K} &= \boldsymbol{T}_{\boldsymbol{F}}\boldsymbol{T}_{\boldsymbol{B}} + \boldsymbol{T}_{\boldsymbol{G}} \\ \boldsymbol{L} &= \boldsymbol{1} - \boldsymbol{T}_{\boldsymbol{F}}(\boldsymbol{T}_{\boldsymbol{A}}\boldsymbol{x}_0 + \boldsymbol{T}_{\boldsymbol{D}}\boldsymbol{D}_{\mathrm{N}_f}) \end{aligned}$$

It is important to remark that $\boldsymbol{U}_{unc}$ is the unconstrained solution of (2), which depends on the initial state and the estimated perturbations during the predicted horizon.